245
3-19-80

DR 899

DOE/CS/95311-1
Unlimited Release
UC-63a Distribution

A Fresnel/Photovoltaic Concentrator Application Experiment for the Dallas-Fort Worth Airport

Phase I - System Design, Final Technical Report (June 1, 1978 to February 28, 1979)

MASTER

M. J. O'Neill
E-Systems, Inc.

Printed December 1979

United States
Department of Energy

Albuquerque Operations Office
Albuquerque, NM 87115

DISCLAIMER

Printed in the United States of America

Available from
National Technical Information Service
U. S. Department of Commerce
5285 Port Royal Road
Springfield, VA 22161

Price: Printed Copy ~~$6.50~~ 9.00 50; Microfiche ~~$3.00~~

DOE/CS/95311-1
UNLIMITED RELEASE
UC-63A DISTRIBUTION

A FRESNEL/PHOTOVOLTAIC CONCENTRATOR APPLICATION EXPERIMENT FOR THE DALLAS-FORT WORTH AIRPORT.

PHASE I: SYSTEM DESIGN.
FINAL TECHNICAL REPORT

1 JUNE 1978 - 28 FEBRUARY 1979

MARK J. O'NEILL, PROGRAM MANAGER

E-SYSTEMS, INC.
ENERGY TECHNOLOGY CENTER
P.O. BOX 226118
DALLAS, TEXAS 75266

PREPARED FOR THE

U.S. DEPARTMENT OF ENERGY
DIVISION OF ENERGY TECHNOLOGY
UNDER CONTRACT ET-78-C-04-5311

LIST OF CONTRIBUTORS

E-Systems, Energy Technology Center

Conceptual Design, Analysis, and Prototype Testing:	M. J. O'Neill A. J. McDanal W. T. Eriksen
Detail Design and Specification:	V. R. Goldberg D. L. Schools D. E. Lubin J. D. Hill

OCLI

Photovoltaic Design and Specification:	R. Brown K. Ling

Consultant

PCU Design:	J. Ross

TABLE OF CONTENTS

TABLE OF CONTENTS (CONT.)

LIST OF FIGURES

TITLE

LIST OF FIGURES

TITLE

LIST OF FIGURES

TITLE

LIST OF TABLES

TITLE

ABSTRACT

This Phase I Final Report sumamrizes the analytical, experimental, design and specification efforts for the first nine months of the Dallas/Fort Worth Airport Fresnel/Photovoltaic Concentrator Application Experiment. The overall objective of the complete three-phase program is to develop and demonstrate a unique photovoltaic concentrator total energy system which, when mass-produced, will provide electrical and thermal energy at costs competitive with conventional energy sources. Toward this objective, the Phase I - System Design contract has been completed, resulting in a final system design, analytical definition of system performance and economics, and a successfully tested prototype collector which fully verified performance predictions.

The proposed system will utilize 245 m^2 of E-Systems linear Fresnel photovoltaic collectors to provide 25 kw_e (AC) of power and 140 kw_t of heat to the Central Utility Facility of Dallas/Fort Worth Airport. The electric power will be used to meet a continuous lighting load, while the thermal energy will be used to preheat boiler feedwater. Peak system efficiencies will be 10.2% electric (insolation to net AC output) and 56% thermal (insolation to net heat delivered). Annual efficiencies will be 8.4% electric and 49% thermal. Production system economics are attractive in the near term: 7¢/Kwh electricity and $7/MMBtu heat (1975 $) could be achieved by 1981 with limited production. With higher production, these costs could be halved by 1990.

1.0 PROJECT SUMMARY

E-Systems, Inc., Energy Technology Center is pleased to submit this final technical report to the United States Department of Energy, in partial fulfillment of Contract No. ET-78-C-04-5311, Phase I, System Design of the Dallas/Ft. Worth Airport Fresnel Photovoltaic Concentrator Application Experiment. The overall objective of the complete three-phase program is to develop and demonstrate a unique photovoltaic concentrator total energy system which, when mass-produced, will provide electrical and thermal energy at costs competitive with conventional energy sources. Toward this objective, the Phase I - System Design contract has been completed, resulting in a final system design, analytical definition of system performance and economics, and a detailed plan for Phase II - System Fabrication and Phase III - System Operation/ Evaluation. Also, during Phase I, a prototype collector was built and successfully tested.

The site selected for the proposed experiment is at the Dallas-Fort Worth Airport, the largest (18,000 acres) airport in the United States. Figure 1.1 shows the airport and the proposed site, the Central Utility Plant, located at the geometric center of the airport. This facility provides heat, hot water and air-conditioning for the entire airport. Note that the Central Utility Facility is located between the two major throughfares of the airport. The collector arrays will be mounted on the roof of this building, which is clearly visible from both thoroughfares. Since more than 10 million persons utilize the airport each year, the site offers exceptional visibility. Other site factors which led to this selection include:

- Large growth potential: Since the proposed system will supply only 1/3% of the plant's total load, a possible future scale-up could be accomplished after technical/economic feasibility is established.

- Wide applicability: Since there are numerous such central energy plants worldwide, this demonstration could lead to system proliferatio in similar applications.

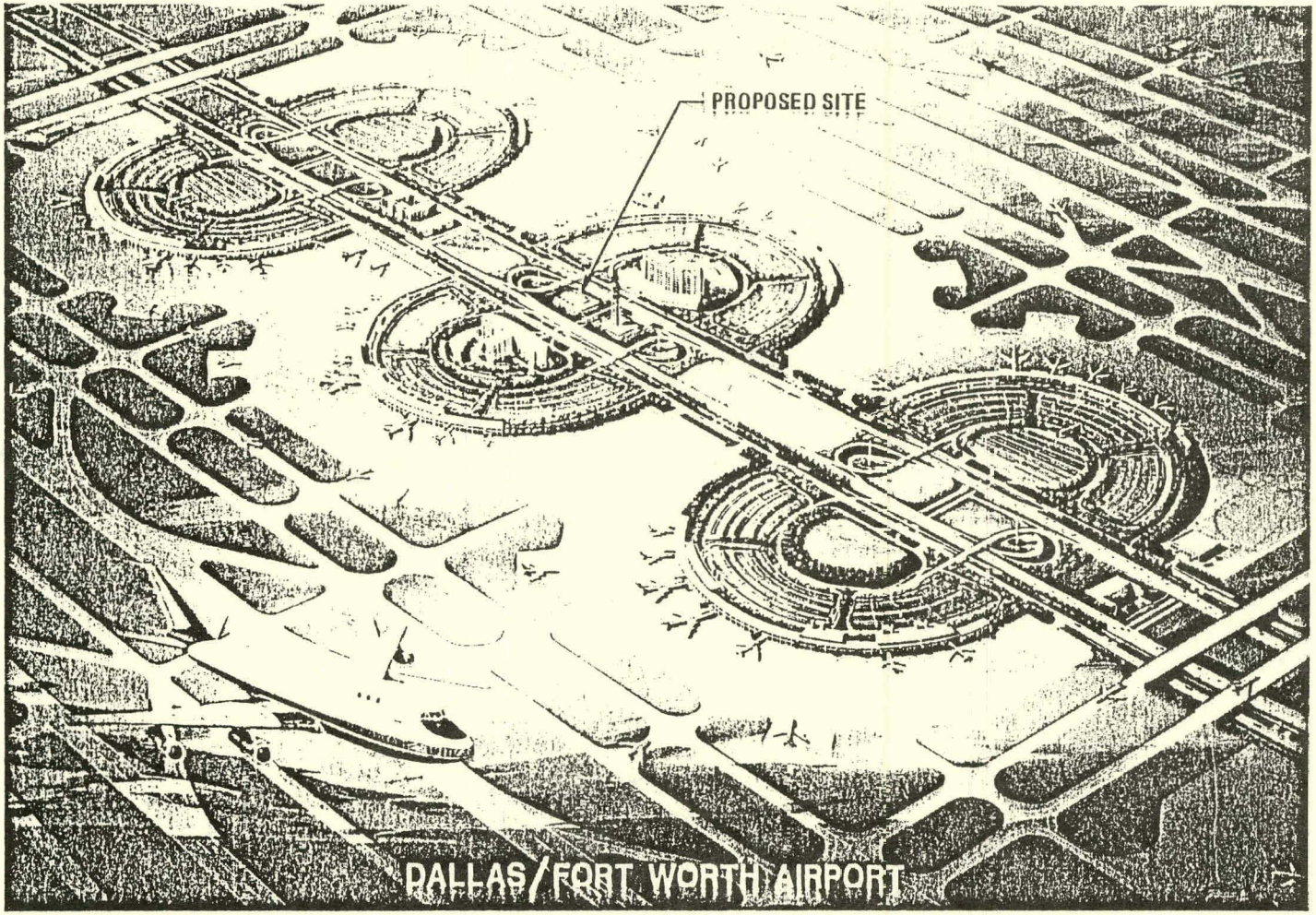

FIGURE 1.1 SITE OF THE EXPERIMENT

- Convenient access: Site visitors, including government contract monitors, team members, visiting dignitaries, et al, can easily visit the site from anywhere in the world.

- High insolation: Direct normal solar radiation is high and typical of the Southwest United States.

- Non-technical factors: No adverse effects to the environment, and no code or rate structure impacts will be caused by the system.

The system design is extremely simple, consisting of the following major elements:

- Concentrator array: 11 array assemblies of 10 collector modules each will provide a total aperture of 245m^2. Each module consists of E-Systems new high-efficiency, short focal length, linear Fresnel lens concentrator which focusses incident sunlight upon actively cooled OCLI silicon photovoltaic cells. Both the electrical and thermal outputs of the collectors will be fully utilized. Peak outputs will be 27 kw_e DC and 140 kw_t.

- Electric interface: A unique, fully transistorized inverter will convert the DC photovoltaic power to useable AC power to provide for parasitics and for a constant 25 kw lighting load within the plant. Supplemental line power from Texas Power and Light Company will be rectified to DC and mixed with the photovoltaic array output to meet the inverter input requirements. No electric storage or waste will be required.

- Thermal interface: The glycol/water solution circulating through the collector field will exchange collected heat with a continuous stream of low temperature (about 30°C) boiler feedwater in the plant. A simple one-pass heat exchanger is used for this nominal 140 kw_t thermal energy transfer. No thermal energy storage or waste will be required.

System performance will be excellent. Peak overall system efficiencies will be 10.2% electric (insolation to net AC output) and 56% thermal (insolation to net heat delivered). Annual efficiencies are also high: 8.4% electric and 49% thermal. Thus, on an annual basis, over 57% of the available insolation will be converted to useful energy output.

System economic viability is also excellent. With limited production, the system could deliver electric energy at a 20-year levelized 7¢/kwh and heat at a 20-year levelized $7/MMBtu (1975$) by 1981, using economic factors appropriate to DFW Airport. In the longer term, with higher production, these levelized costs should

drop to about 3¢/kwh and $3/MMBtu (1975$) by 1990. On a life cycle basis, even the near term energy costs above are competitive with conventional energy costs when modest fuel escalation rates are considered.

To verify the excellent performance estimates made for the new system, a prototype collector module was built and tested during Phase I. Since the proposed collector system will consist of 110 collector modules, each of which is the functional equivalent of the prototype collector, these test results are an excellent indicator of full system performance. Key test results are:

- At system design point conditions, i.e., cell temperature about 55°C, the overall collector electrical efficiency was measured to be 11.3%. This value agrees with predications made in the original proposal a year ago within 1% (predicted value: 11.4%).
- At design point conditions, the overall collector thermal efficiency was measured to be 56.4%. This value agrees with predictions made in the Mid-Program Review within 4% (predicted value: 58.6%), despite gaps in the lens, a 25 mph wind, and 8°C cooler ambient during the test.
- At design point conditions, the overall (thermal & electrical) collector efficiency was measured to be 67.7% , only 3% lower than the predicted 70%.
- The lens net transmittance was measured, using a short circuit current ratio with and without the lens in place, to be 88.7%, 4% higher than the predicted 85%.
- The image width produced by the lens was substantially less than the cell width, indicating that concentration ratios well above 25 are achievable in the long term.

Detailed plans for Phases II and III are presented in the Phase II/III proposal and will not be repeated in this report. Similarly, the detailed design drawing package will not be included in this report, but is available from DOE upon request.

Program participants include E-Systems, DFW Airport, Optical Coating Lab, and Texas Power and Light Company.

2.0 CONCEPTUAL SYSTEM DESIGN AND ANALYSIS

2.1 System Description

The proposed Fresnel/Photovoltaic/Photothermal power system (depicted in Figure 2.1.1) will supply a nominal 25 kw_e (AC) of electrical power and 140 kw_t of process heat to the Central Utility Facility of the Dallas-Fort Worth Airport. The electrical output of the photovoltaic system will be used to power the continuous-duty emergency lighting system within the plant, which consists of high efficiency fluorescent and mercury vapor lamps. The thermal output will be used to preheat boiler feedwater which is condensed at 85-95°F (29-35°C) within a continuous-duty Rankine cycle power system in the plant. Since both electrical and thermal outputs of the photovoltaic system are always less than or equal to the loads with which they interface, neither electrical storage nor thermal storage will be required, and no appreciable solar-generated energy will be wasted for lack of load. The low-temperature heat load available (boiler feedwater) enhances both the electrical and thermal performance of the system, since the silicon cells operate more efficiently for lower cell temperatures, and thermal losses from collectors and piping are lower for lower fluid temperatures.

The solar concentrator array consists of 11 arrays of 10 collector modules each. Each module utilizes a unique, high-efficiency, short F-number, linear Fresnel lens of 3 feet (91.4 cm) aperture width by 8 feet (244 cm) aperture length, to focus incident sunlight upon a series-connected string of 53 silicon solar cells. Each cell is 1.44 inches (3.66 cm) wide by 1.78 inches (4.52 cm) long, thus forming an 8 foot (244 cm) long cell string one twenty-fifth as wide as the lens. Thus, the geometric concentration ratio of the collector is 25. The peak power voltage of each cell under

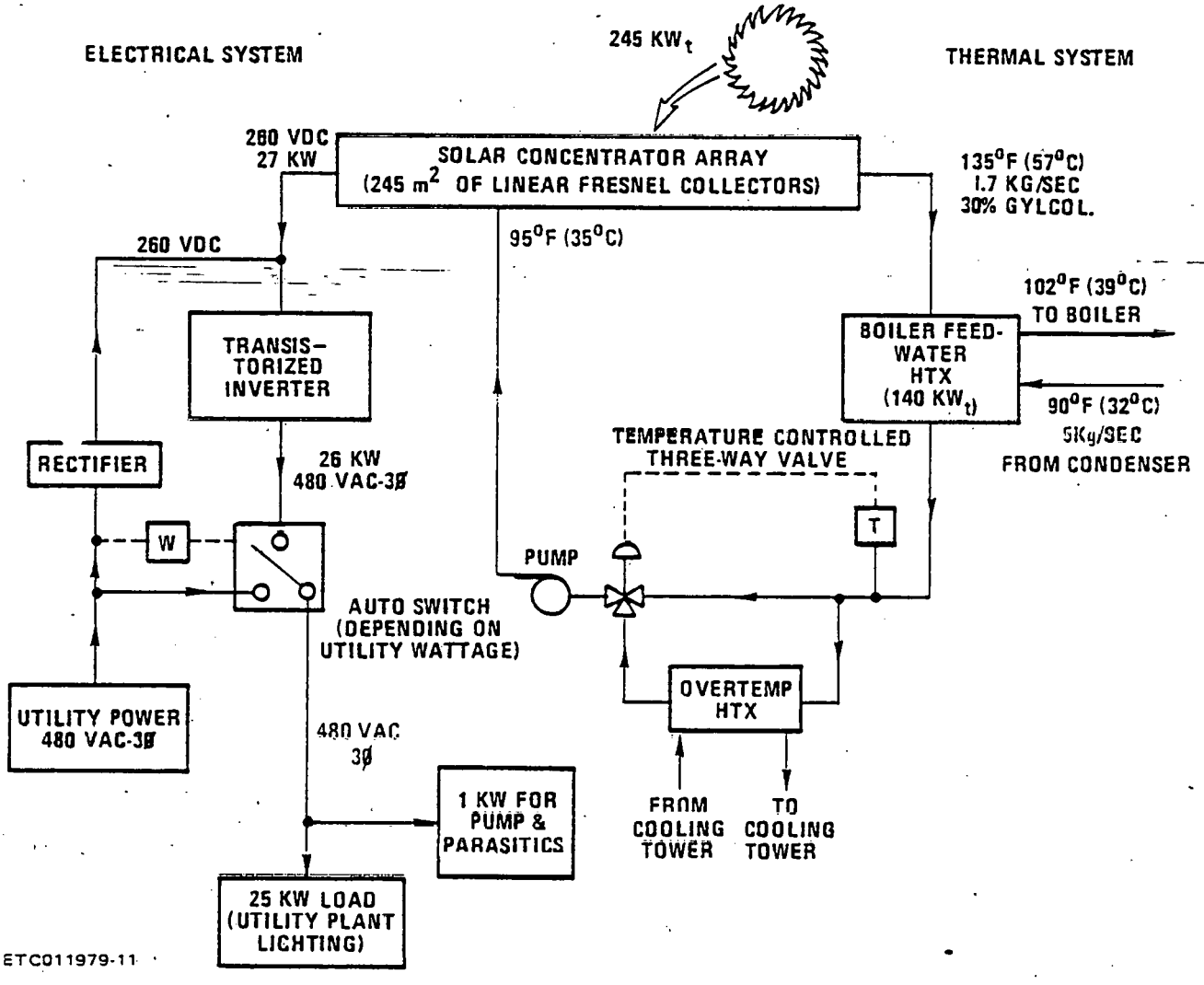

FIGURE 2.1.1. BLOCK DIAGRAM OF THE FRESNEL/PHOTOVOLTAIC/PHOTOTHERMAL POWER SYSTEM FOR DFW AIRPORT

operating conditions is approximately 0.49 volts such that 53 series cells provide 26 volts at peak power. Ten modules are connected in series to form a nominal 260 volt array. Eleven such arrays wired in parallel will produce about 27 kw_e of direct current power at 260 volts when the direct normal insolation is 1000 w/m^2 and the cell temperature is about 55°C. The cell string within each module is mounted to a copper fin/tube heat sink through which a 30% solution of ethylene glycol/water is circulated. This fluid absorbs the thermal energy produced in the cell assembly by the incident concentrated solar flux. Each array is plumbed with ten modules in series with a nominal array temperature rise of 40°F (22.2°C). The eleven arrays are plumbed in parallel to one another. Full details of the array design and performance are presented in Section 3.1.

The electrical interface utilizes a unique fully transistorized inverter developed for the rapid transit industry (Reference 1). This inverter has an overall DC-to-AC efficiency of 97%, based upon prototype test data. Thus, at peak conditions, 26 kw of 480 VAC power will be output from the inverter to meet load and parasitic requirements. The previously described load is an invariant 25 kw lighting load. The parasitic power requirements, consisting mainly of the pump motor, but also including tracking motors and control power, amount to less than 1 kw. Supplemental power is provided by the local utility, Texas Power & Light Company (TP&L). However, a TP&L regulation prohibits mixing of on-site generated AC electricity with utility AC power (cogeneration). Therefore, the supplemental power is mixed with the photovoltaic power at the DC level of Figure 2.1.1, i.e., after rectifying line power to DC. While this interface arrangement causes losses

in supplemental power due to the inefficiencies of the rectifier and inverter, it meets the previously mentioned regulation and it provides one distinct advantage. Since the combined photovoltaic array output and the supplemental utility power are mixed to provide a constant 27 kw (DC) input/26 kw (AC) output at the inverter, this device always operates at a fixed load. Thus, the inverter is designed for optimal efficiency at this 27 kw - in/26 kw-out load, and it never operates at off-design load. Of course, the rectifier must operate at a variety of loads depending upon photovoltaic output. Fortunately, the rectifier inefficiencies are quite small, varying from less than 200 watts at zero rectifier output to less than 600 watts at full (27 kw) output, which correspond to only 0.8% and 2.4%, respectively, of the 25 kw lighting load. Thus the supplemental utility power losses are small for the proposed design. Whenever the utility wattage drawn by the system exceeds the 25 kw load being met by the system (e.g., when clouds obscure the sun), the automatic switch will disconnect the load from the photovoltaic system and substitute utility power directly to meet the load. This will prevent operation of the system at a net energy loss condition. Although not shown in Figure 2.1.1, the power conditioning unit (PCU) utilizes a closed-loop peak power point tracking system to maintain the DC voltage setting at the point of maximum photovoltaic array output. Full details of the PCU, control and switchgear are presented in Section 3.2.

The thermal interface design is even simpler than the electrical interface design. A single-pass, counterflow, shell-and-tube heat exchanger is used to cool the glycol solution from the collector array by heating boiler feedwater as it flows between the condenser and boiler of the steam

Rankine cycle power system within the plant. This feedwater flow rate varies with weather conditions, since the primary output of the Rankine cycle system is used to drive centrifugal chillers for meeting the air-conditioning needs of the terminals, hotels, and other facilities at DFW Airport. However, there is always enough feedwater flow to absorb the full solar system heat output without the feedwater exceeding 200°F (93°C) at the outlet of the heat exchanger. Typically, the feedwater flowrate is around 40,000 lbm/hr (18,000 kg/hr) and can absorb the full array heat output with a mere 12° F (7°C) temperature rise, as shown in Figure 2.1.1. The peak solar thermal output will be about 140 kw_t when the insolation level is 1 kw/m^2. In the event of a feedwater stoppage due to some plant failure, a thermostatically controlled three-way valve will divert the glycol solution flow through an overtemperature heat exchanger which is cooled by water from the plant cooling towers. This will prevent array overheating during such failure-mode periods.

In summary, the proposed system is a simple total energy system, wherein the electrical output will be inverted and used to power a constant-load lighting system, with rectified line power supplying supplemental energy, while the thermal output will be absorbed in total by a low temperature feedwater heat sink. In comparison to other applications, this system offers the following important advantages:

- This system will fully utilize both the electrical and the thermal outputs of the solar collectors. Since six times more thermal energy than electrical energy is produced, the economic value of the heat is greater than the electricity, and this heat should not be wasted.
- This system is modular, with the basic building block being a single array of 10 collector modules (240 ft^2 or 22.3 m^2 of aperture per 10 module array). The ten modules in each

array are both wired and plumbed in series to provide the full voltage and temperature rises of the system. Thus, any number of arrays can be wired and plumbed together in parallel to provide any desired electrical/thermal output. While eleven such arrays have been selected for the present application to match the 25 kw load, the successful implementation of the current system will also prove the feasibility of this system concept for any other reasonable size load, since only the number of arrays will vary in other size systems.

- Both the thermal and electrical loads are continuous, twenty-four hours per day, seven days per week, and both loads are always greater than or equal to the solar system outputs. Therefore, neither thermal nor electrical storage will be required, and no solar-derived energy will be wasted. This represents an optimal load, since it maximizes system efficiency while minimizing system cost.

- The output thermal energy is useful at a very low temperature since the feedwater heat sink temperature is only 85-95°F (29-35°C). This maximizes photovoltaic cell performance and collector thermal performance, since heat losses to the environment at this low temperature are minimal.

- The site is excellent in terms of maximal public exposure (10 million annual passengers), high insolation, a trained staff of plant operation/maintenance personnel, large expansion potential (18,000 acres), similarity to numerous central energy plants worldwide, and ease of access for visitors from any part of the world.

- The system will be the first to use the new high-efficiency, short F/Number, linear Fresnel concentrator in a photovoltaic application.

- The system will be the first to use the fully transistorized, high-efficiency PCU in a photovoltaic application.

2.2 System Analysis

2.2.1 E-Systems Novel Fresnel Lens Concentrator

2.2.1.1 Background

For the past two years, a major company-funded development effort has been underway at E-Systems with the objective of commercializing a unique Fresnel lens solar concentrator. This new concentrator, fully described in U.S. Patent No. 4,069,812, utilizes a configuration which provides the highest possible transmittance achievable with a refractive prismatic lens concentrator. Additionally, the new lens has a remarkable tolerance for aberrations and errors which are present in all refractive concentrators. Because of this tolerance for errors, the new lens is most amenable to low cost manufacturing methods such as extrusion/embossing, a process being perfected by E-Systems under Sandia Contract No. 13-2359. The following paragraphs describe the new concentrator and compare its performance to more conventional Fresnel lens devices.

2.2.1.2 Fresnel Lens Comparisons

Figure 2.2.1.1 shows schematically a Fresnel lens solar collector with several possible lens concentrators. Note that since all of these potential lenses have the same rim angle (θ_{max}), the remainder of the collector (receiver, housing, plumbing, etc.) is essentially the same regardless of which lens is selected. Then how does one select which lens to use? The answer is, or course, to select the lens which performs the best, and this performance is measured by two key parameters: transmittance and concentration ratio (aperture width/receiver width). The new lens under development by E-Systems is fully optimized for maximal transmittance, as rigorously proven in Reference 2. This maximal transmittance is achieved through the use of

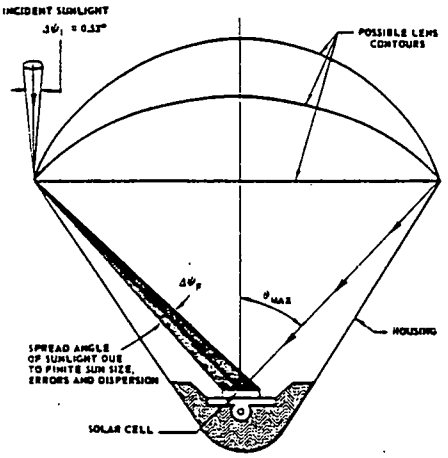

ETC011979-40

FIGURE 2.2.1.1
INFINITE FAMILY OF LENS CONTOURS FOR SAME RIM ANGLE CONCENTRATOR

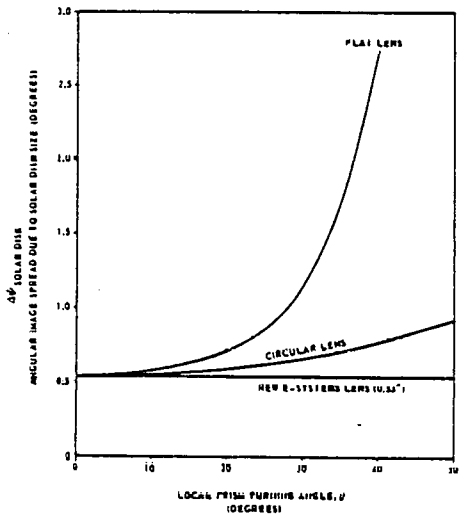

FIGURE 2.2.1.2 ANGULAR IMAGE SPREAD DUE TO FINITE SOLAR DISK

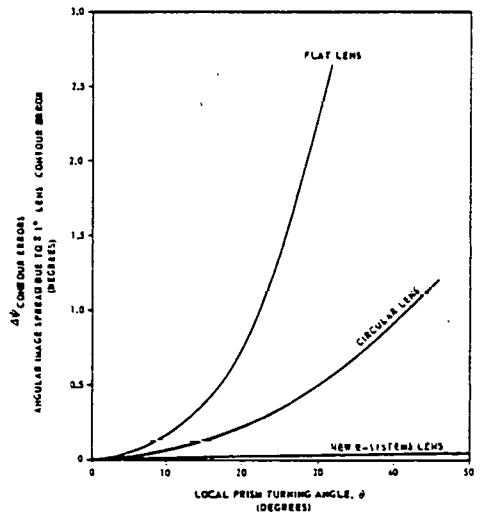

FIGURE 2.2.1.3 ANGULAR IMAGE SPREAD DUE TO LENS CONTOUR ERROR

ETC011979-42

prisms each of which makes equal incidence angles with the solar ray at both the front and back prism faces. This equal incidence angle condition, combined with additional requirements for zero shading and/or blocking within or between prisms, fully defines the lens configuration for maximal transmittance. The resultant lens has a smooth convex outer surface forming a curve of decreasing radial distance with increasing rim angle; the equi-incidence angle prisms are formed on the inside concave surface.

The superior transmittance properties of this new lens are fully described in Reference 2 and will not be repeated here. However, the other key performance index, concentration ratio, requires further discussion. Note in Figure 2.2.1.1 that the incident sunlight is all contained within a small cone of 0.53° spread angle, corresponding to the solar disk. However, after refraction by a prism, the leaving sunlight is contained within a larger spread angle, corresponding to not only the sun's angular size, but also errors and dispersion. This final spread angle ($\Delta\Psi_F$) is important since the receiver size must be larger for larger spread angles, i.e., the larger $\Delta\Psi_F$, the smaller the concentration ratio. The spread angle may be broken into its components as:

$$\Delta\Psi_F = \Delta\Psi_{\substack{\text{solar}\\\text{disk}}} + \Delta\Psi_{\substack{\text{contour}\\\text{errors}}} + \Delta\Psi_{\substack{\text{prism}\\\text{angle}\\\text{errors}}} + \Delta\Psi_{\text{dispersion}} .$$

Fortunately, the transmittance-maximized lens discussed above also provides smaller spread angles due to solar disk size, contour errors, prism angle errors and dispersion than for more conventional lens designs. For comparison, each of these spread angles has been calculated for three different lens designs: the new lens, a flat lens, and a circular arc lens with its center

at the focal line. For all three lenses, the prisms are on the inner surface of the lens and the material is acrylic plastic.

Figure 2.2.1.2 presents the spread angle component due to the solar disk angular diameter of 0.53 degrees. The flat lens greatly enlarges the spread angle over the incident solar disk angle, expecially for large prism turning angles. This gross enlargement of the sun's image at large turning angles precludes the use of flat lenses for large rim angle concentrators; thus, flat lenses can only be used for low rim angle (long focal length) concentrators. The circular lens spread angle is better, but is still large at large turning angles. In contrast, the new lens spread angle is identical to the incident spread angle of 0.53 degrees, regardless of prism turning angle. Additionally, note that the new lens spread angle is much smaller than for either of the other lenses, markedly so for large turning angles.

Figure 2.2.1.3 presents curves of spread angle due to a lens contour error of 1 degree. This error corresponds to a slope error over the lens surface and is analogous to the slope errors of reflective concentrators. Since Fresnel lenses must be free-standing over most of their surface areas, as opposed to reflective concentrators which can be rigidly supported over their full surface area, slope errors due to wind and gravity deflections will be relatively large. Such errors badly spread the sunlight for both the flat and circular lenses, but have a barely noticeable effect on the new lens. This insensitivity to contour errors is a direct result of the equi-incidence angle prisms comprising the new lens. A contour error causes a slight increase in one incidence angle which causes a corresponding decrease in the other incidence angle, thereby netting a very small effect. (Although not shown in Figure 2.2.1.3, a reflective concentrator would have a total image spread of 4 degrees for a $\pm$ 1 degree slope error, regardless of turning angle).

Figure 2.2.1.4 presents spread angle due to prism angle errors. This error corresponds to the actual prism facet angles, and represents a lens manufacturing error. Note that once again the new lens is superior to the other two lenses, especially for large turning angles.

Figure 2.2.1.5 presents angular spread due to dispersion, i.e., variation in index of refraction over the wavelengths in the solar spectrum. A nominal variation in index of refraction from 1.48 to 1.50 was used to prepare these curves, and corresponds approximately to acrylic plastic's dispersion curve. Note that once again the new lens shows superiority to the others.

Table 2.2.1.1 summarizes the comparison for two cases of practical importance: rim angle values of 27° and 45°. The former corresponds to an F/1.0 lens in flat form, and the latter to an F/0.5 lens in flat form. (F/# is ambiguous for curved lenses since focal length varies across the lens; rim angle is a more definitive parameter). Note that for the 27° rim angle case, the new lens total spread angle ($\Delta\Psi_F$) is about 30% smaller than for the circular lens, and about 60% smaller than for the flat lens. Similarly, for the 45° rim angle case, the new lens spread angle is about 40% smaller than for the circular lens, and the flat lens will not work at all at this rim angle. Thus, in terms of concentration ratio, which is inversely proportional to spread angle, the new lens is substantially superior to the other lens designs.

One additional error tolerance employed in the new lens design is pictorially described in Figure 2.2.1.6. Low-cost manufacture of Fresnel lenses by methods such as the extrusion/embossing technique generally results in some rounding of the prism peaks due to imperfect filling of the roll/die and surface tension/memory effects within the plastic material.

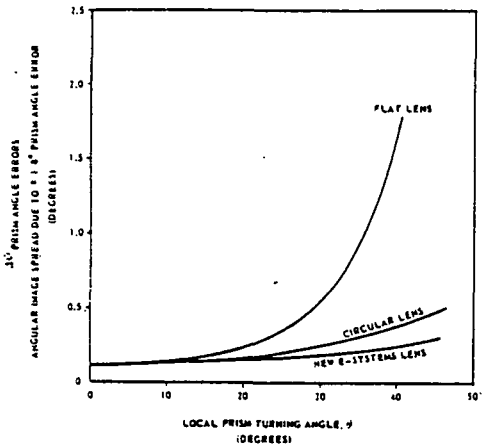

FIGURE 2.2.1.4 ANGULAR IMAGE SPREAD DUE TO PRISM ANGLE ERRORS

ETC011979-43

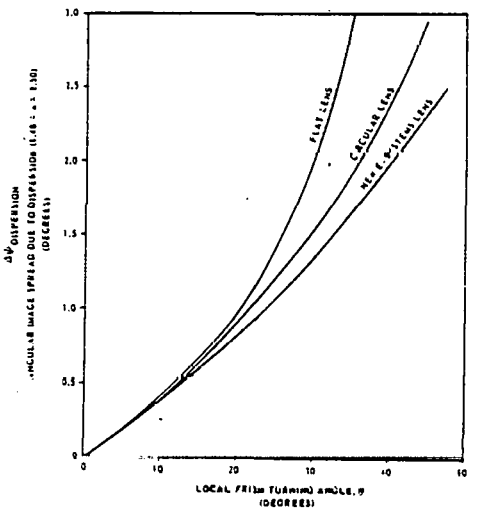

FIGURE 2.2.1.5 ANGULAR IMAGE SPREAD DUE TO DISPERSION

ETC011979-44

	LENS TYPE	θ MAX	Δψ SOLAR DISK @ 0.53°	Δψ CONTOUR ERRORS @ ± 1°	Δψ PRISM ANGLE ERRORS @ ± 1/8°	Δψ DISPERSION @ Δ n = .02	$\Delta\psi_F$ (TOTAL)
F/1.0	FLAT	27°	0.95°	1.75°	0.42°	1.62°	4.74°
	CIRCULAR	27°	0.64°	0.40°	0.22°	1.34°	2.60°
	NEW	27°	0.53°	0.01°	0.18°	1.16°	1.88°
F/0.5	FLAT	45°	WILL NOT WORK				
	CIRCULAR	45°	0.84°	1.16°	0.48°	2.95°	5.43°
	NEW	45°	0.53°	0.03°	0.30°	2.33°	3.19°

TABLE 2.2.1.1 COMPARISON OF FRESNEL LENS CONCENTRATORS

ETC011979-45

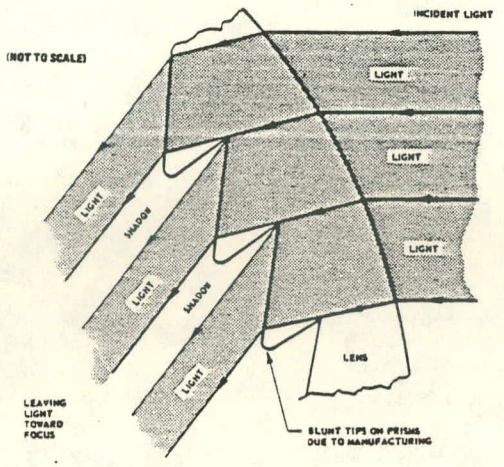

FIGURE 2.2.1.6 PRISM FACE OVEREXTENSION TO MINIMIZE OPTICAL LOSSES

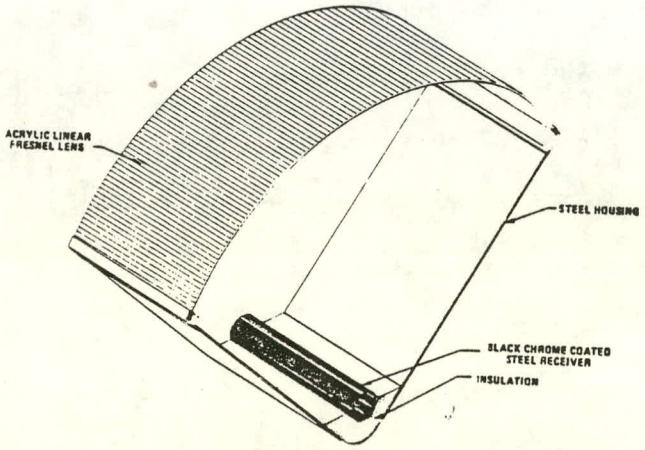

FIGURE 2.2.1.7 E-SYSTEMS FRESNEL LENS SOLAR HEAT COLLECTOR

ETC-011979-47

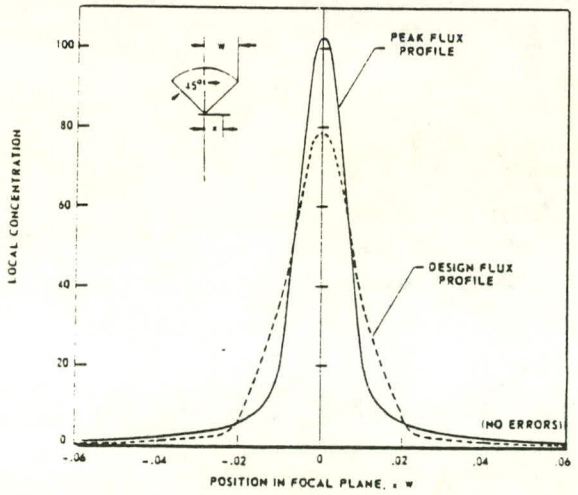

FIGURE 2.2.1.8
FLUX PROFILE OF 45° RIM ANGLE FRESNEL LENS SOLAR CONCENTRATOR

ETC011979-48

Such peak rounding causes direct losses in transmittance for conventional Fresnel lenses, but not for the new lens since these rounded peaks are overextended beyond the light path through the prism. Thus, with the prism peak tucked out of the way of the light passing through the prisms, the new lens has a high tolerance for both peak rounding and bottom prism face angular mislocation. In magnitude, this blunt tip allowance is greatest for the deepest prisms near the extremity of the lens; for the outermost prism of the 45 degree rim angle concentrator, the blunt tip may be 24% as wide as the prism itself with no optical loss.

To summarize the above discussion and comparisons, the new E-Systems Fresnel lens solar concentrator is far superior to conventional Fresnel lens devices in transmittance, concentration ratio, and tolerance for errors and aberrations. The following section summarizes the expected performance of the new concentrator.

2.2.1.3 E-Systems Concentrator Performance Summary

The Fresnel concentrator development program currently underway at E-Systems under company funding has primarily been directed toward a solar heat collector. Figure 2.2.1.7 shows a schematic of this photothermal device. Cost minimization studies have led to the selection of a short focal length (high rim angle) concentrator of relatively large dimensions. A three foot (0.91 m) aperture width, 45° rim angle, and eight foot (2.44 m) aperture length have been selected to provide a compact, light-weight, low-cost collector module.

While the fundamental generalized design of the new Fresnel lens is described in the patent specification, an additional important

independent variable is the design index of refraction (n_D) for each prism in the lens. Since the solar spectrum extends over a broad range of wavelengths (0.4 - 2 microns) and since acrylic plastic's index of refraction varies substantially over these wavelengths (1.51 - 1.48), the choice of n_D greatly affects the resultant flux profile in the focal plane. While in the past a constant value of n_D has been utilized for all prisms in a Fresnel lens, better results can be achieved by varying n_D from prism to prism. This allows the individual prism images to be superimposed in any desired manner to produce a desired result in the focal plane, in an analogous manner to adding terms in a Fourier series to produce a desired function. To evaluate this effect and to accurately determine flux profiles for the new lens, a detailed optical model has been developed at E-Systems for the concentrator. This model uses the method of cone optics, i.e., analytical tracing of finite conical bundles of rays originating across the solar disc incident upon each point on the lens surface. This model treats each of the following:

- Finite sun.
- Solar image displacement (dispersion) for each wavelength band in the solar spectrum.
- Transmittance variation with prism location.
- Actual prism angular errors of any type and distribution across lens.
- Any desired variation in n_D, including prism to prism variations.
- Any rim angle (F-Number).

Basically the model determines the local flux ($\dot{q}_x$) at any location (x) in the focal plane by performing the following triple integration:

$$\dot{q}_x = \int_{\theta} \int_{1} \int_{\lambda} \frac{\tau \dot{q}_\lambda}{A_{image}} \left(\frac{dA_{aperture}}{d\theta dl} \right) d\lambda dl d\theta,$$

wherein θ is local rim angle lens coordinate,
l is local longitudinal lens coordinate,
λ is wavelength,
τ is transmittance (a function of θ and λ)
A_{image} is solar image area in the focal plane (a function of θ),
$\dot{q}_\lambda$ is the incident radiant flux at wavelength λ per unit wavelength,
$A_{aperture}$ is aperture area.

The integral is carried out for all wavelengths (λ) in the solar spectrum, and over all contributing portions (θ, 1) of the lens which have refracted cones which overlap the point x in the focal plane. Results of this analysis are discussed in the following paragraph.

Figure 2.2.1.8 shows two possible flux profiles achievable with the new lens. The solid curve can be obtained by superimposing images from the individual prisms such that the individual image peaks are all coincident in the focal plane, thereby providing a maximal center-point concentration. The dashed curve can be obtained by superimposing images from the individual prisms such that the greatest amount of energy is concentrated within a region defined by $(-0.02 \leq \frac{x}{w} \leq +0.02)$; this design provides a maximum amount of energy interception at a concentration ratio of 50 for a rim angle of 45 degrees. (Higher concentration ratios are achievable with lower rim angles, but the resultant deeper collector modules would be heavier and more costly.) This nominal concentration ratio of 50 was selected for the design configuration.

While the lens currently being developed at E-Systems is optimized for concentration ratio of 50, errors due to manufacture, assembly,

alignment, tracking, drive, deflection, etc., will lower this value in practice. A detailed error analysis has been conducted to define maximum expected values of all errors and the resultant effect on achievable concentration ratio. Table 2.2.1.2 summarizes this error budget and presents a conservative estimate of achievable concentration. The effects of prism angular errors, lens contouring slope errors, and lens-receiver alignment were calculated from optical analysis. The module tracking, drive, structure and alignment errors were calculated from electro-mechanical and structural analyses. The longitudinal incidence error occurs because of the simple roll-tilt tracking strategy employed (discussed below) which maintains a zero incidence angle across the prismatic lens (laterally) but not along the linear lens (longitudinally). This tracking scheme allows the longitudinal incidence angle to vary from zero to ten degrees on the worst day (solstice) of the year, with a resultant image displacement due to focal length foreshortening. Note that the RSS total of all errors is only ± 0.180" (0.46 cm) a reasonable value for a 36" (91 cm) aperture width lens. Due to the Gaussian shape of the lens flux profile (Figure 2.2.1.8), the solar image width may be artitrarily defined as that width containing a certain percentage of transmitted sunlight. For 95% of the transmitted energy, this width is 1.08" (2.74 cm). Thus, the required receiver width must equal this image width plus the displacement error in both directions, or 1.44" (3.66 cm). Therefore, a net concentration ratio of 25 should be readily achieved in practice.

In addition to concentration ratio, the other key parameter of lens performance is transmittance. As mentioned previously, the new lens provides a maximal transmittance. Even for the short focal length lens under consideration (with a 45° rim angle), the average single-surface

TABLE 2.2.1.2 - ERROR BUDGET/CONCENTRATION RATIO

ERROR TYPE	MAX. EXPECTED VALUE	IMAGE DISPLACEMENT
Prism Angles	± 0.125°	± 0.095" (± 0.241 cm)
Lens Contour	± 1.00°	± 0.012" (± 0.030 cm)
Lens/Receiver Alignment	± 0.010°	± 0.010" (± 0.025 cm)
Tracking Controller	± 0.05°	± 0.031" (± 0.079 cm)
Drive/Linkage	± 0.05°	± 0.031" (± 0.079 cm)
Structural Deflection	± 0.05°	± 0.031" (± 0.079 cm)
Module Alignment	± 0.05°	± 0.031" (± 0.079 cm)
Longitudinal Incidence	± 10.0°	± 0.139" (± 0.353 cm)

- TOTAL PROBABLE IMAGE DISPLACEMENT (RSS TOTAL) ± 0.180" (± 0.457 cm)
- SOLAR IMAGE WIDTH CONTAINING 95% OF TRANSMITTED SUNLIGHT = 1.08" (2.743 cm)
- REQUIRED RECEIVER WIDTH = 1.08" + 2 (0.180")= 1.44" (3.66 cm)
- NET CONCENTRATION RATIO = 36"/1.44" = 25

TABLE 2.2.1.3 - LENS TRANSMITTANCE

LOSS TYPE	FRACTION OF INCIDENT SUNLIGHT LOST
FRONT SURFACE REFLECTION	4.3%
ABSORPTION/SCATTERING	2.0%
BACK SURFACE REFLECTION	4.0%
FLUX PROFILE TRUNCATION*	4.5%
TOTAL LOSSES	14.8%

- Net Transmittance = 85.2%

* Undersizing the receiver width such that the low flux tail of the flux profile curve is not intercepted.

reflectance loss for all prisms in the lens is only 4.3%, compared to 3.9% for a flat sheet of acrylic. However, other transmittance losses include absorption/scattering within the acrylic, and cutting off the low flux "tail" of the focal plane flux profile. All losses are summarized in Table 2.2.1.3. Note that a net transmittance of more than 85% will be achieved.

In summary, the concentrator will provide a concentration ratio of 25 and a net transmittance of 85%. Empirical verification of these performance parameters is fully described in Section 3.1.

2.2.2 Photovoltaic Receiver Module

The photovoltaic receiver module is shown schematically in Figure 2.2.2.1. It consists of a series string of 53 photovoltaic cells mounted on an eight foot (244 cm) long actively cooled copper heat sink. The following paragraphs describe the photovoltaic cells and the fin/tube heat sink and the analysis which determined the final design selection.

2.2.2.1 Photovoltaic Cell

The photovoltaic cells designed by OCLI for the DFW application are single crystal silicon cells designed specifically for concentrated sunlight input. For the proposed application, each cell is 1.44 inches (3.66 cm) active width by 1.78 inches (4.52 cm) long by 0.014 inches (0.036 cm) thick. Details of the methods used in designing, optimizing and manufacturing these cells are fully described in Reference 3.

Sandia Laboratories (Reference 3) has experimentally determined the performance of similar OCLI photovoltaic cells under actual concentrated sunlight. Figures 2.2.2.2 and 2.2.2.3 present the results of these measurements in terms of conversion efficiency as a function of concentration and cell temperature. Of special importance in the proposed application is the point shown on Figure 2.2.2.2 at 55°C (131°F) and 21.25 suns (0.85 x 25 suns), since this corresponds to the nominal operating conditions expected for the DFW installation. The conversion efficiency at this operating point is 13.4%. Additionally, OCLI has estimated the absorptance of the cells to be approximately 85% of the incident concentrated sunlight. These data were further substantiated by E-Systems' prototype test program described in detail in Section 3.1. The efficiency versus temperature profile obtained in

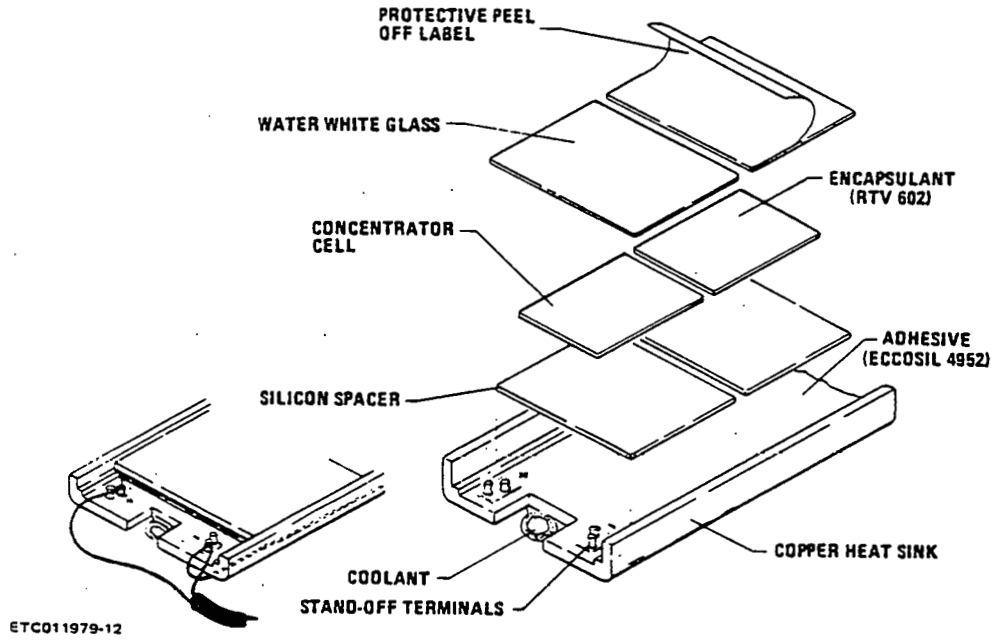

FIGURE 2.2.2.1 PHOTOVOLTAIC RECEIVER MODULE

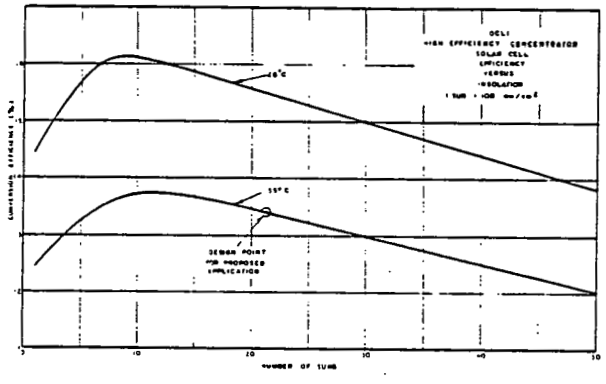

FIGURE 2.2.2.2 CELL EFFICIENCY VS. CONCENTRATION

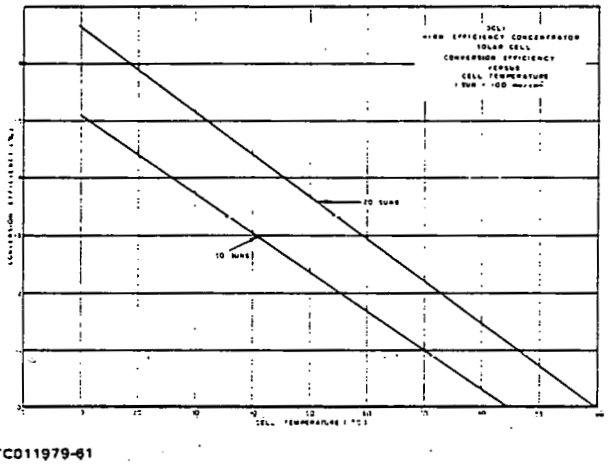

FIGURE 2.2.2.3 CELL EFFICIENCY VS. TEMPERATURE

the prototype tests performed under a variety of operating conditions show excellent correlation with the curve shown in Figure 2.2.2.3.

For the system simulation analysis described in Section 2.2.6, the cell performance was modeled as follows:

- The incident radiant flux on the cells was determined.
- The average cell temperature for the cell string on the receiver was determined.
- The cell string efficiency was calculated from the data of Figures 2.2.2.2 and 2.2.2.3, based upon the average temperature and flux level defined above.

An electric circuit analysis of series - connected cells was performed and proved that the overall efficiency corresponds to the average temperature of the cells in the string.

2.2.2.2 Photovoltaic Receiver Thermal/Fluid Analysis

The fin/tube heat sink, shown schematically in Figure 2.2.2.1 serves to actively cool the photovoltaic cells by transferring the thermal energy produced in the cell assembly by the incident concentrated solar flux to a coolant fluid which circulates through the receiver module. Optimal design of the heat sink not only increases thermal performance but also increases electrical performance since the cell conversion efficiency increases with decreasing cell temperature. In the following paragraphs the rationale for selecting copper as the heat sink material is given, the analysis conducted to select the design fin thickness and the diameter of the coolant tube is discussed and the overall temperature distribution through the photovoltaic receiver module is presented.

Copper was selected as the base material for the fin/tube heat sink instead of aluminum based on the following considerations:

- Copper has a thermal conductivity a factor of two larger than aluminum. An aluminum heat sink with the same thermal perfor-

mance as a copper heat sink would be twice as thick. Since the cost of copper is approximately twice the cost of aluminum and twice as much aluminum is required, the total material cost would be approximately equal.

- An all-copper fluid circulation loop will be used to minimize corrosion. In contrast, solar energy systems with water-solution-cooled receivers and absorbers made of aluminum have historically performed poorly under actual field operating conditions due to leaks and corrosion problems.

- Copper offers superiority in fabricability, since it can be soldered and brazed, it requires standard fittings, and all plumbing contractors are familiar with its use.

Enhanced performance of the photovoltaic receiver module requires minimization of the temperature differential between the photovoltaic cells and the coolant fluid. In the following paragraphs three distinct temperature gradients are discussed, leading to the selection of the fin thickness and tube diameter. They are:

- The gradient between the average cell temperature and average fin temperature,

- The gradient between the average fin temperature and fin base temperature (directly above the tube),

- The gradient between the fin base temperature and the coolant fluid temperature.

In the analysis and design of the photovoltaic cell stack OCLI selected materials with good thermal properties (i.e., thermal conductivities, etc.) over materials with lesser thermal properties to maintain as small a temperature differential through the cell stack as possible. For a system operating at a net concentration ratio of 21.25 suns and a cell temperature of 55°C (131°F) OCLI has determined that the temperature gradient between the cell and fin is less than 2°C (3.6°F).

Thermal analysis and fluid mechanical analysis of the copper fin/tube heat sink were performed independently of the cell stack to determine the fin thickness and tube diameter which reduces the temperature gradient along the fin and the gradient between the fin base and the fluid to an acceptable value. To uncouple the cell stack thermal analysis from the

fin/tube analysis the actual flux profile (Figure 2.2.1.8, Section 2.2.1) incident on the cell stack was reduced appropriately to account for: lens transmittance losses (τ = 0.85), cell absorptance (α = 0.85), and energy converted to DC electricity (η = 0.134). Nominal values for these quantities are listed in parenthesis. Once the fin/tube heat transfer rates and temperatures were obtained from the analysis, the temperatures and heat transfer rates were calculated for the cell stack by assuming one-dimensional conduction.

The thermal model treats two-dimensional conduction within the copper fin/tube heat sink, thermal losses from the fin surface, and convection between the tube wall and coolant fluid. The fluid mechanical model treats pressure drops in the receiver tube, interconnect piping and minor losses to define pumping power requirements. A computer code containing both thermal and fluid models was developed and tradeoff studies were conducted for various fin thicknesses, tube diameters and coolant fluids. Water, ethylene glycol and several heat transfer fluids (Caloria HT-43, Therminol, Dowtherm) were considered as coolant fluids. A 30% ethylene glycol/water solution was selected due to its good heat transfer characteristics, low pumping power requirements and freeze protection.

The results of the analysis used to determine the design fin thickness are presented in Figure 2.2.2.4. As shown, the difference between the integrated average fin temperature ($T_{fin_{avg}}$) and the fin base temperature ($T_{fin_{base}}$) decreases with increasing fin thickness. A 0.125 in. (0.318 cm) fin thickness with the corresponding 2°F (1.1°C) temperature gradient was selected because at this point on the curve further increases in fin thickness yield only small decreases in temperature gradient.

Figures 2.2.2.5 and 2.2.2.6 show the effects of tube diameter and mass flow rate on cell output power and pumping power respectively. Cell output power is defined as the product of the lens transmittance, the cell conversion efficiency and the direct normal insolation. For low

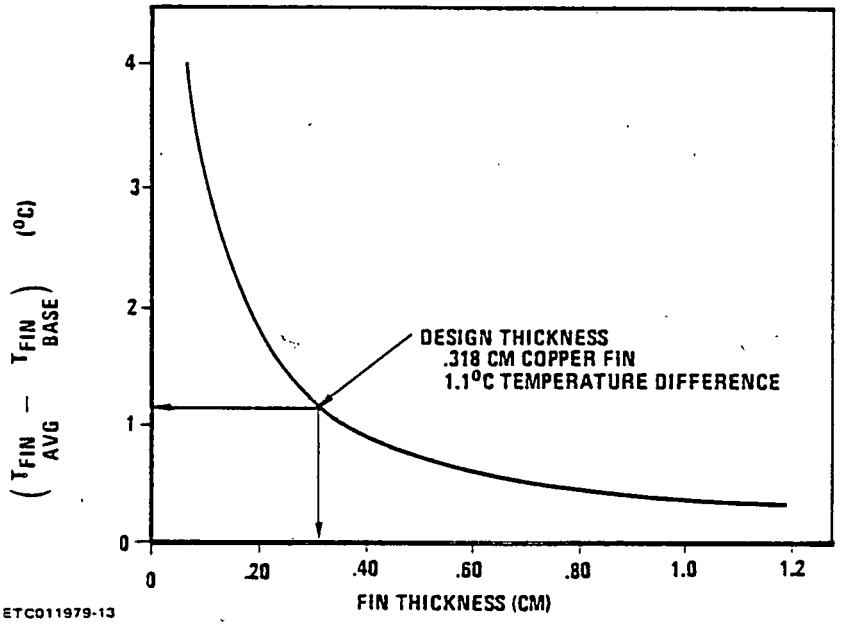

FIGURE 2.2.2.4 FIN THICKNESS DETERMINATION

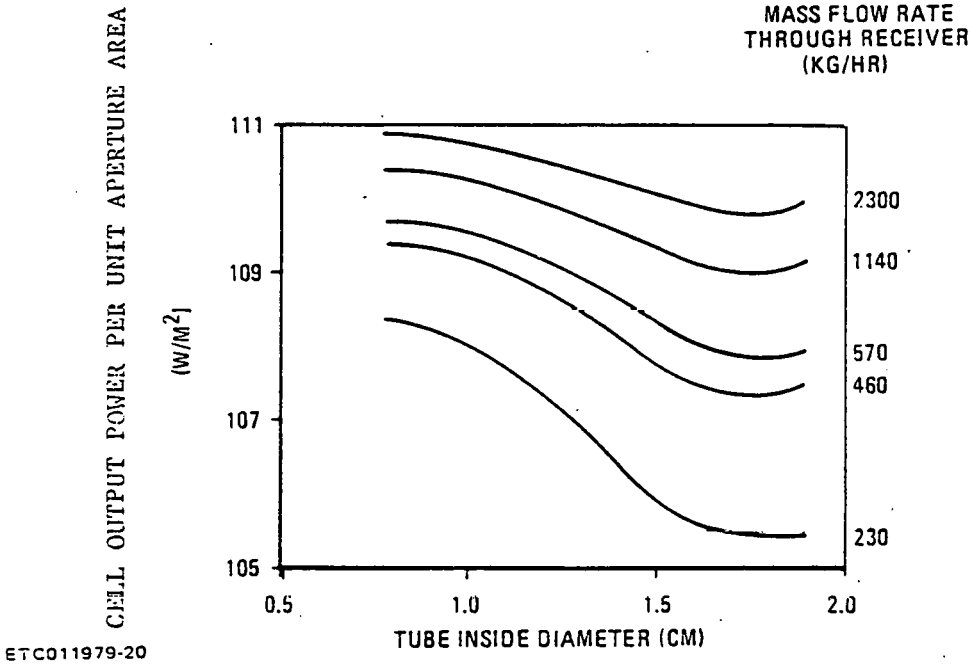

FIGURE 2.2.2.5
EFFECT OF RECEIVER TUBE DIAMETER AND MASS FLOW RATE ON CELL OUTPUT POWER

mass flow rates the cell operates at a higher temperature because of poor convection within the tube, which results in a reduction in cell output power. Pumping power increases with increasing mass flow rate and increases with decreasing tube diameter. As shown in Figure 2.2.2.6 small tube diameters and large flow rates result in a costly pumping power penalty. By defining a net output power as the difference between the cell output power and pumping power and plotting these results as functions of tube diameter and flow rate (as shown in Figure 2.2.2.7), determination of the final design tube diameter is possible. A 0.65 in. (1.65 cm) diameter copper tube was selected to provide a maximal net output power over a wide range of allowable flow rates. The final receiver design selected is shown schematically in Figure 2.2.2.8.

The temperature distribution through the photovoltaic receiver module, the heat transfer rates and the electrical power output rate are shown in Figure 2.2.2.9 for a 0.65 in. (1.65 cm) tube diameter and a 0.125 in. (0.318 cm) fin thickness. For the conditions listed, the cell which is at 131°F (55°C) is approximately 17°F (9.4°C) above the fluid temperature. The cell to fluid temperature differential as a function of flow rate for various levels of direct normal insolation is presented in Figure 2.2.2.10.

In summary, the final design of the photovoltaic receiver module includes a 0.65 in. (1.65 cm) diameter copper tube mounted to a 0.125 in. (0.318 cm) thick copper fin. A 30% ethylene glycol/water solution is the coolant fluid. The thermal and fluid mechanical model of the photovoltaic receiver module as described herein is incorporated into the total system simulation analysis discussed in Section 2.2.6.

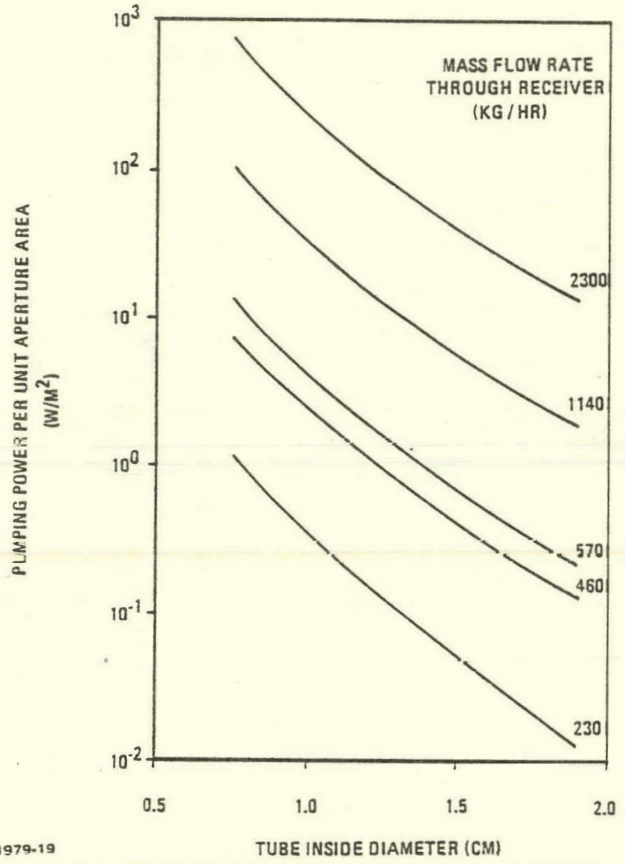

FIGURE 2.2.2.6 EFFECT OF RECEIVER TUBE DIAMETER AND MASS FLOW RATE ON PUMPING POWER

NET OUTPUT POWER = CELL OUTPUT POWER – PUMPING POWER

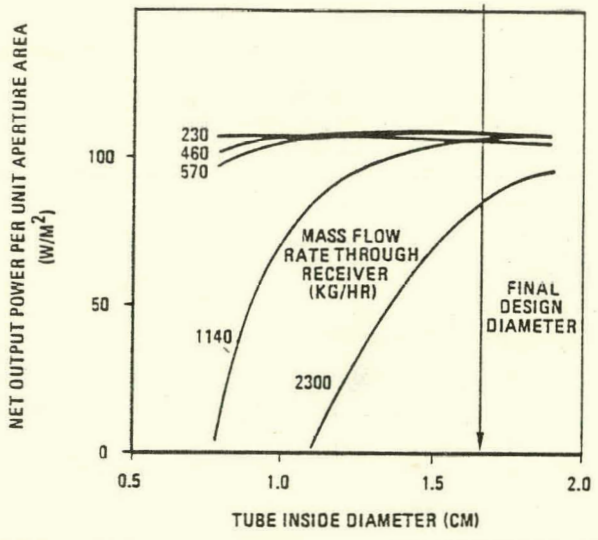

FIGURE 2.2.2.7 EFFECT OF RECEIVER TUBE DIAMETER AND MASS FLOW RATE ON NET CELL OUTPUT

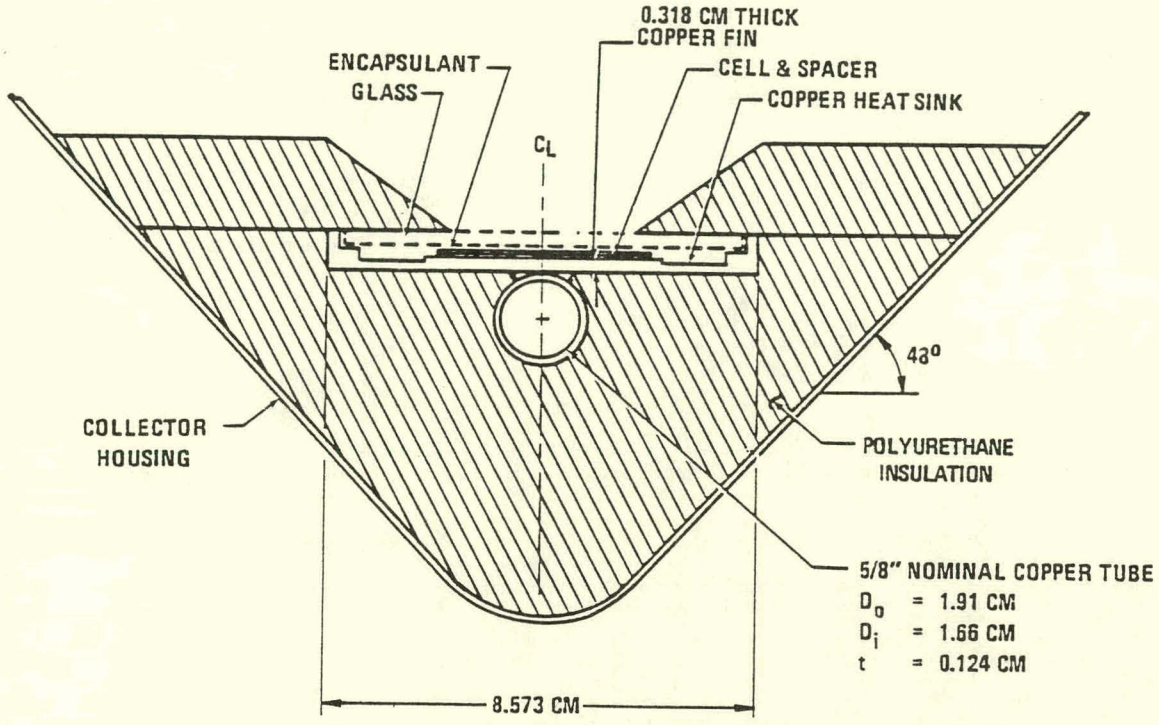

FIGURE 2.2.2.8 RECEIVER SCHEMATIC

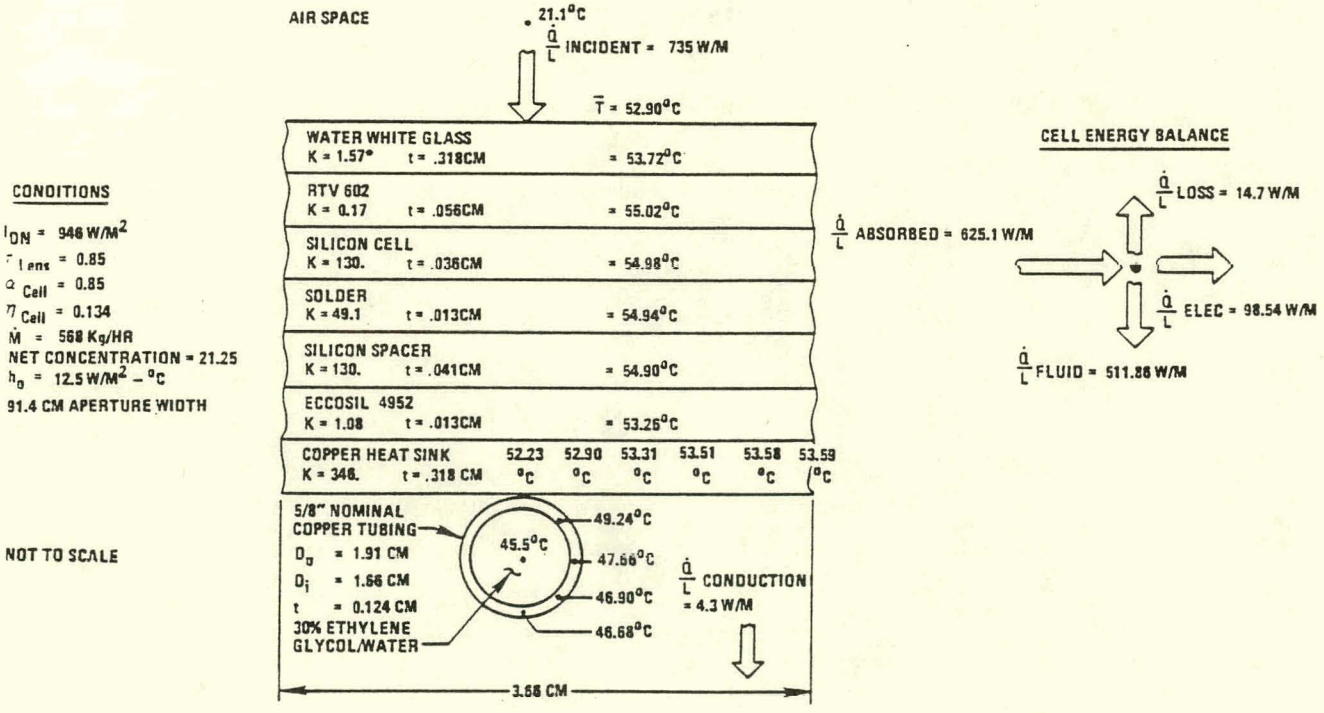

FIGURE 2.2.2.9 TEMPERATURE DISTRIBUTION THROUGH CELL STACK AND RECEIVER ASSEMBLY

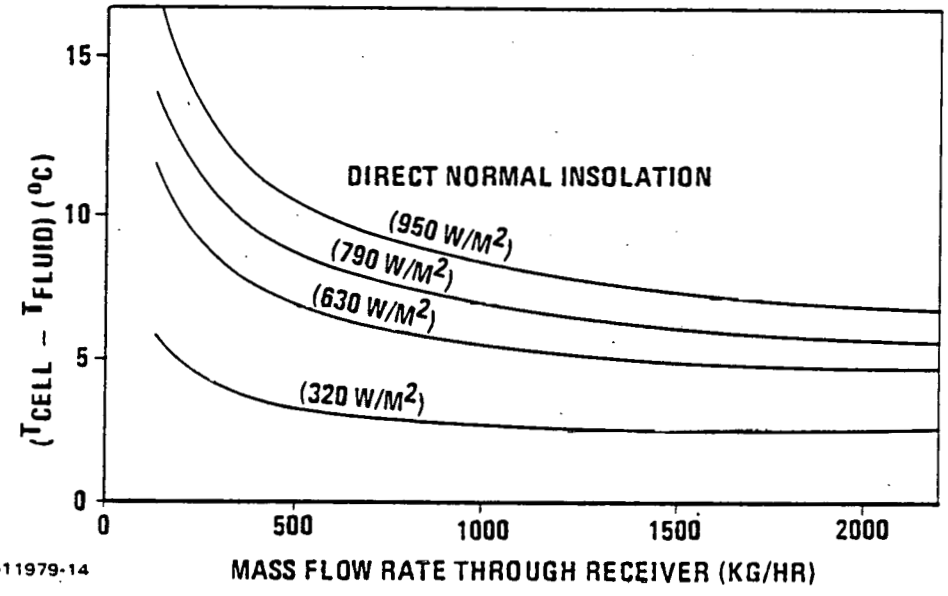

FIGURE 2.2.2.10 CELL TO FLUID TEMPERATURE DIFFERENTIAL FOR FINAL RECEIVER DESIGN

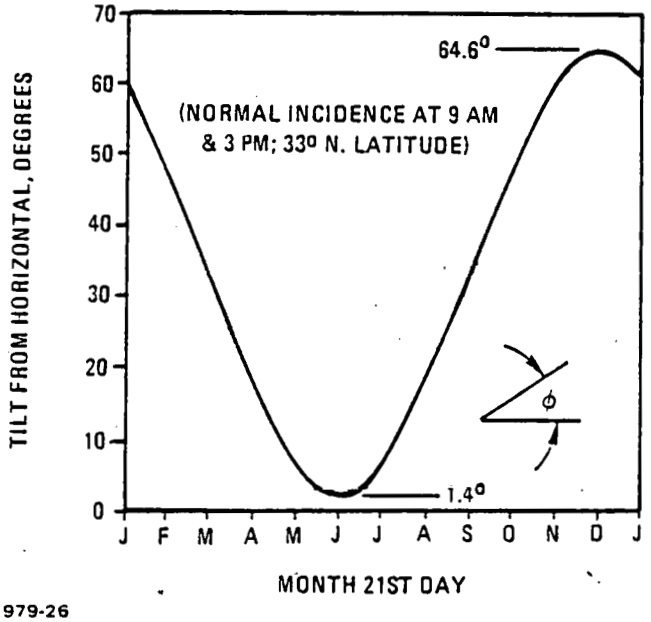

FIGURE 2.2.3.1
FRESNEL COLLECTOR ARRAY
ANNUAL TILT ANGLE VARIATION

2.2.3 Fresnel/Photovoltaic Collector

2.2.3.1 Tracking System Analysis

As previously discussed, ten collector modules are mounted in a common support frame and are linked together via the roll-axis drive system to actively follow the sun's diurnal motion. Additionally, the frame tilt angle toward the south is adjusted every few days via the tilt-axis drive system to minimize the effect of the sun's declination angle variation through the year. This approach to tracking has been selected for the new Fresnel collector for the following reasons:

- Single axis tracking, i.e., polar-axis tracking, results in a large deterioration in lens image quality due to a foreshortening of the lens focal length with longitudinal incidence angles of $\pm 23.5^{\circ}$.
- Full two-axis tracking is expensive in terms of travel limits, ground or deck interfaces, drive system complexity, etc.
- The roll/tilt system maintains incidence angles at essentially zero in the roll direction and less than 10 degrees in the longitudinal direction, thereby maintaining an excellent image quality, with no continuous tilt angle tracking.
- The roll/tilt system achieves an annual tracking efficiency of about 90%, a value which would be difficult to exceed with full two-axis tracking.

Thus, the roll-tilt strategy provides the optical and tracking benefits of full two-axis tracking, with less complexity and lower cost.

The proposed system will require tilt angle adjustment every few days to follow the curve of Figure 2.2.3.1. This tilt angle variation will provide the tracking performance summarized in Figure 2.2.3.2. The longitudinal angle of incidence will remain at $0^{\circ} \pm 10^{\circ}$ for the full operational day (9-10 hours) year-round. On the equinoxes, the longitudinal incidence angle is zero all day. On the solstices, it varies from less than 8° (absolute value) at noon to 10° (absolute value) at 4 hours 40 minutes either side of

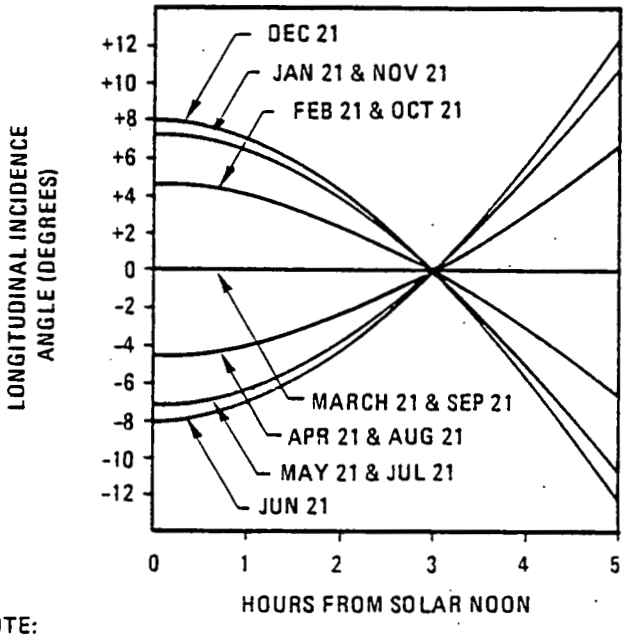

NOTE:
MINUS SIGN INDICATES SUN VECTOR IS SOUTH OF COLLECTOR APERTURE NORMAL,
PLUS SIGN INDICATES SUN VECTOR IS NORTH OF COLLECTOR APERTURE NORMAL.

ETC011979-29

FIGURE 2.2.3.2 LONGITUDINAL INCIDENCE ANGLE FOR THE ROLL/TILT TRACKING SYSTEM WITH PERIODIC TILT ADJUSTMENT

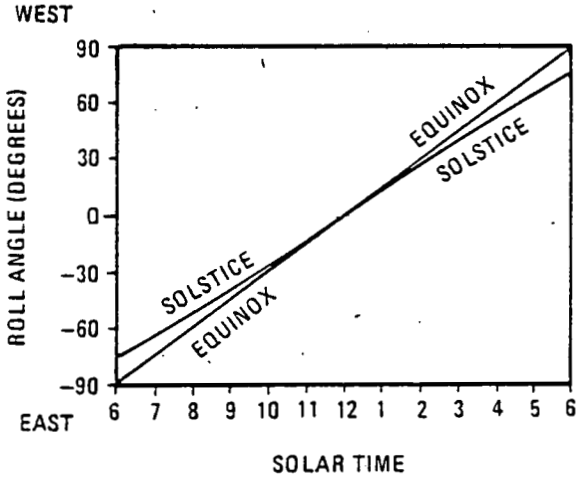

FIGURE 2.2.3.3
ROLL ANGLE MOTION ENVELOPE

ETC011979-30

noon. On an annual basis, the average incidence angle is less than 4° (absolute value). Thus, on an annual basis, the cosine loss is negligible and the receiver shaded length due to the end plate of the trough is only about 1% of the full receiver length. Note in Figure 2.2.3.2 that the selected tilt angle variation through the year (Figure 2.2.3.1) provides for a zero incidence angle at 9 am and 3 pm year-round. This time was selected to balance the plus and minus incidence angles at noon and early/late in the day, to maintain the absolute value of the incidence angle as small as possible on average through the day.

The rate of roll angle motion is not constant during the day, except at equinox, as shown in Figure 2.2.3.3. Thus, a clock drive will not work for the roll motion; an active, sun-seeking system is required, as described in Section 3.3.

Tradeoff studies have been conducted to determine the optimal module-to-module spacing and roll axis travel limits. Figure 2.2.3.4 presents the results of these tradeoffs in terms of an annual average tracking efficiency. As one would expect, the closer the module spacing, the greater the annual shading loss and the lower the tracking efficiency. Similarly, the roll angle travel limit (λ_{max}) reduces sky coverage and thereby lowers tracking efficiency. To achieve 100% tracking efficiency, an infinite spacing and full (90°) roll axis motion would be required. The selected design, based upon cost/performance considerations, is shown on Figure 2.2.3.4. This design uses closely spaced modules (5 feet (1.52 meters) center-to-center spacing for 3 feet (0.91 meter) aperture width) to minimize support frame size and cost. Also, it utilizes roll angle travel limits of ± 75° to minimize interference problems and drive system travel, thereby minimizing cost.

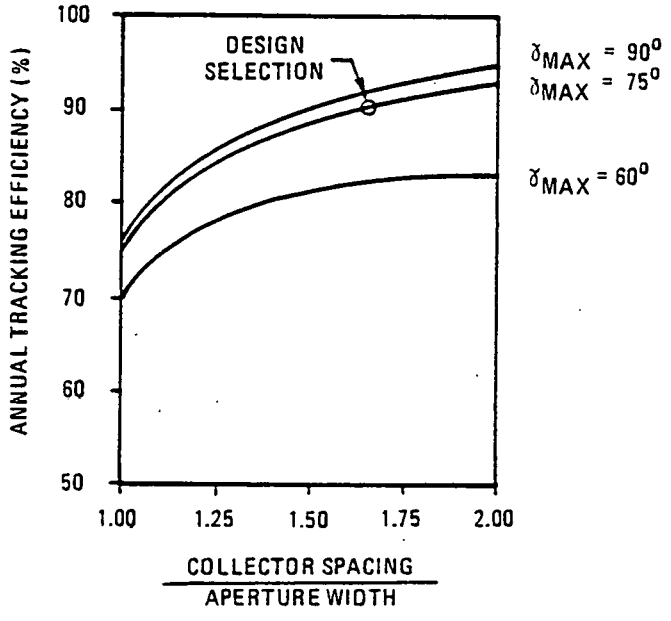

ETC011979-27

FIGURE 2.2.3.4
EFFECT OF COLLECTOR SPACING AND MAXIMUM ROLL ANGLE ON TRACKING EFFICIENCY

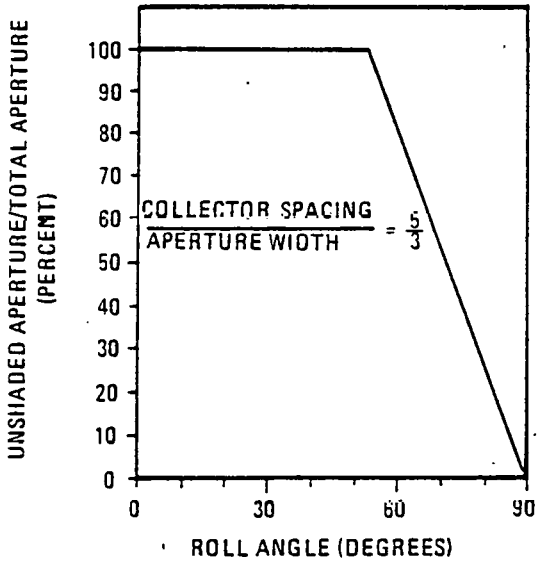

ETC011979-28

FIGURE 2.2.3.5
MODULE-TO-MODULE SHADING LOSS

Even with this close spacing and restricted roll travel, the annual tracking efficiency is a respectable 90%. For this selected spacing, Figure 2.2.3.5 summarizes the module-to-module shading loss as a function of roll angle. Note that at the cut-off roll angle (75°), the modules are about 60% shaded or 40% unshaded.

For the selected module spacing and roll travel limits, the instantaneous tracking efficiency calculation was included in the system simulation program described in Section 2.2.6.

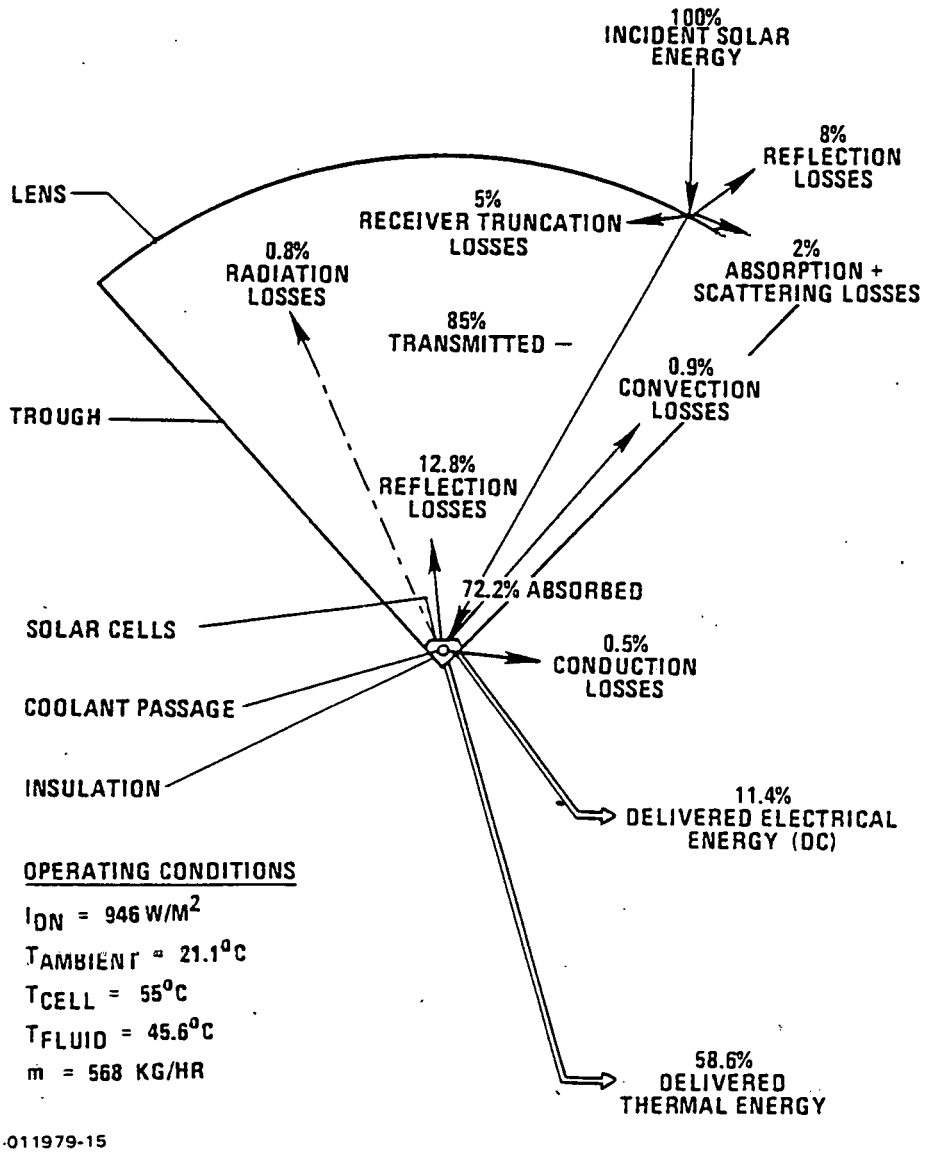

FIGURE 2.2.3.6 FRESNEL PHOTOVOLTAIC SOLAR COLLECTOR ENERGY BALANCE

2.2.3.2 Collector Performance Analysis

Figure 2.2.3.6 presents the instantaneous collector performance near solar noon from incident sunlight to output thermal and electrical energy. The equation for the electrical power output per unit aperture area is:

$$\dot{e}_o = \frac{\dot{E}_o}{A_{aper}} = \tau I_{dn} \eta_{cell}$$

where $\dot{e}_o$ = electrical power output per unit aperture area; $\dot{E}_o$ = electrical power output; A_{aper} = aperture area; τ = lens transmittance; I_{dn} = direct normal insolation flux; η_{cell} = photovoltaic cell conversion efficiency.

The overall collector solar to electrical efficiency is thus:

$$\eta_e = \frac{\dot{e}_o}{I_{dn}} = \tau \eta_{cell}.$$

As discussed in Sections 2.2.1 and 2.2.2, the lens transmittance is 85%, and the cell efficiency for 55°C and 21.25 suns (.85 x 25 suns) is 13.4%. Therefore, η_e = 11.4%, as shown in Figure 2.2.3.6.

The thermal power output per unit aperture area is:

$$\dot{q}_o = \frac{\dot{Q}_o}{A_{aper}} = \tau\alpha I_{dn} - \dot{q}_{loss} - \dot{e}_o$$

where $\dot{q}_o$ = thermal power output per unit aperture area; $\dot{Q}_o$ = thermal power output; A_{aper} = aperture area; τ = lens transmittance; α = cell/receiver absorptance; I_{dn} = direct normal insolation flux; $\dot{q}_{loss}$ = thermal loss rate per unit aperture area due to convection, conduction, and radiation from receiver to environment; $\dot{e}_o$ = electrical power output per unit aperture area.

The overall collector solar to thermal efficiency is thus:

$$\eta_t = \frac{\dot{q}_o}{I_{dn}} = \tau\alpha - \frac{\dot{q}_{loss}}{I_{dn}} - \eta_e.$$

As previously mentioned, τ = 85% and η_e = 11.4%. Conductive, convective and radiative thermal losses as discussed in Section 2.2.2.2 are 2.2% of the incident direct normal insolation. The absorptance of the cell/receiver module is estimated

by OCLI to be 85%. Therefore, η_t = 58.6%.

In summary, the collector will convert 58.6% of the incident sunlight to useful heat output and 11.4% to useful electrical output; thus, 70% of the available insolation will be effectively captured.

2.2.4 Electrical System

The electrical system interface is shown schematically in Figure 2.1.1. The 25 KW constant-load emergency lighting system was selected as the system load because of its invariance and ease of interface. The nominal 260 VDC voltage level for the photovoltaic array was selected for the following reasons:

- This voltage closely matches the 277 VAC line-to-neutral voltage required by the 480 VAC 3Ø load, thereby maximizing PCU performance.
- This voltage is high enough to minimize I^2R line losses, while low enough to avoid exceeding standard equipment (wiring, contactors, breakers, etc.) voltage ratings.
- This voltage is conveniently achieved in the collector arrays with 10-module series wiring of reasonably sized cells.

For the system simulation study described in Section 2.2.6 the electrical system interface is modeled conceptually as shown in Figure 2.1.1. Each component in the electrical system is discussed in detail in Section 3.2 and only the information needed in the system simulation is summarized here.

The rectifier efficiency is a function of the supplemental utility power required to augment the photovoltaic output to meet the 25 KW load. The efficiency versus receifier output power shown in Figure 3.2.4 was curve-fit for the system simulation model. The inverter, designed for optimal efficiency for the constant 27 KW DC input, has an overall DC to AC efficiency of 97%.

System parasitic losses other than rectifier and inverter losses are modeled as: a 3% loss due to collector end plate shading of cells (Section 3.1.4); a 2% loss due to cell mismatch and series resistance (Section 3.2); a variable loss due to fluid pumping (Section 2.2.5); and negligible loss due to module tracking (Section 3.2).

The hour-by-hour array/line/load interaction is modeled as follows:

- The DC electrical output of the photovoltaic array is determined. If the photovoltaic DC output after inversion to AC electricity is sufficient to meet the 25 KW load plus parasitics, then the load is supplied by the photovoltaic output.
- If the photovoltaic output is insufficient to supply the load, supplemental utility power is rectified, mixed with the photovoltaic output at the DC level, inverted to AC electricity and supplied to the load.
- Whenever the utility line power drawn by the system exceeds the load the automatic switch disconnects the load from the photovoltaic system and substitutes utility power directly.

2.2.5 Thermal Transport System

The thermal transport system interface is shown schematically in Figure 2.1.1. The interface is a simple recirculation loop through the solar concentrator array and through a boiler feedwater heat exchanger. The thermal system is modeled conceptually as shown in the figure.

The DFW thermal load is a combined flow of condensate arriving from a chilled water pump steam turbine condenser and from a chiller turbine condenser, both streams being part of a continuous duty Rankine cycle power system in the plant. The condensate flow rate varies with local weather conditions since the output of the Rankine cycle system is used to drive centrifugal chillers for meeting the airconditioning requirements of the terminals, hotels, and other facilities at the DFW airport. Based on recent operating records at the DFW Central Utility Facility (Reference 4) the following table was compiled to characterize the total condensate flow rate as a function of wet-bulb temperature.

Wet Bulb Temperature (^{o}C)	Total Condensate Flow Rate (kg/hr)
< 8	2000
8-10	4500
10-21	4500-16000
21-25	16000-19000
>25	19000

For the system simulation study the boiler feedwater heat exchanger and over-temperature heat exchanger were modeled in general as counterflow shell-and-tube type with variable flow rates. Preliminary calculations were performed to determine the general thermal capacity range (UA product) sufficient to absorb the full solar concentrator array thermal output at a reasonable temperature differential. Once the range was established an actual heat exchanger was selected and the actual performance based on the manufacturer's thermal capacity specification was incorporated into the system simulation model.

Parasitic thermal and electrical losses associated with the thermal system interface include pumping power requirements to overcome pressure drop throughout the system and piping thermal losses. Pipe sizing was selected to keep pumping power requirements to a minimum. The overall pressure drop through the thermal system was modeled and incorporated into the system simulation as a function of the square of the mass flow rate. Insulation thickness on all plumbing and piping was selected to minimize thermal piping losses which were included in the system simulation study as a function of temperature differences between the fluid and ambient. These parasitics were incorporated into the system simulation study described in Section 2.2.6.

2.2.6 System Simulation

The results of individual component analysis and subsystem analysis (Section 2.2.1 through 2.2.5) have been incorporated into a total system computer model to accurately simulate the performance of the proposed Fresnel/Photovoltaic/Photothermal power system. Tradeoff studies were conducted on collector array size, control strategy and thermal and electrical interface component selection to assess their effects on annual electrical and thermal energy outputs. A summary of the system simulation model is shown in Figure 2.2.6.1. The system simulation was conducted on an hour by hour basis throughout the year using insolation and weather data models for the Dallas/Fort Worth area compiled by Aerospace Corporation (Reference 5) and a Typical Meteorological Year (TMY) model compiled by Sandia Laboratories (Reference 6). The results which follow are based on the Aerospace Corporation weather model. A comparison of this model to the TMY model is presented and the effect on performance is discussed.

Tradeoff studies were conducted to determine the number of collector arrays required to meet the DFW electrical and thermal loads. Eleven arrays were selected because peak output from the solar power system was sufficient to meet the DFW electrical load without any electrical waste. Twelve arrays result in waste electrical output and ten arrays require additional supplemental line power to meet the electrical load. The thermal output of eleven arrays also matches well the feedwater heat sink's minimum heat requirements.

Similarly, a study was conducted to determine the design flow rate for optimal annual performance. The results of this study are presented in Figure 2.2.6.2. As shown, peak annual thermal efficiency (49.4%) occurs for flow rates above 600 kg/hr; peak annual electrical efficiency (8.5%) occurs at 460 kg/hr. As a tradeoff, a single array design flow rate of 568 kg/hr (6250 kg/hr for the eleven arrays) was selected yielding a net electrical efficiency of 8.4% and a net thermal efficiency of 49.3% annually. The flow rate

- HOURLY VALUES OF I_{DN}, T_{WB}, T_{DB} USING 1962 DALLAS/FT. WORTH DATA COMPILED BY AEROSPACE CORPORATION, TMY DATA COMPILED BY SANDIA LABORATORIES
- CONCENTRATOR – τ = 85%, CR = 25, HOURLY TRACKING & SHADING LOSS
- RECEIVER – ENERGY BALANCE RE-COMPUTED HOURLY FOR EACH MODULE (10 MODULES IN SERIES) TO DETERMINE η_{CELL}, T_{CELL}, T_{FLUID}, $\dot{Q}_{COLL}$, $\dot{E}_{COLL}$, $\dot{Q}_{LOSS}$, U_{LOSS} COEFFICIENT DETERMINED EXPERIMENTALLY. α_{CELL} = 85% (OCLI)
- INVERTER – η = 97%
- ARRAY ELECTRICAL LOSS – CELL MISMATCH AND RESISTANCE LOSSES (2%)
- PARASITICS – INCLUDE PUMPING AND TRACKING POWER LOSSES
- SUPPLY LOSSES – LINE AC TO DC (VARIABLE RECTIFIER EFFICIENCY), DC TO AC (97% INVERTER), TOTAL LOSS APPROXIMATELY 7% OF LINE POWER
- HEAT EXCHANGER – ENERGY BALANCE RE-COMPUTED HOURLY BASED ON $UA_{OVERALL}$ AND $\dot{M}_{CONDENSATE}$ AND $\dot{M}_{ARRAY}$
- DFW THERMAL LOAD – $\dot{M}_{CONDENSATE}$ AS A FUNCTION OF AMBIENT CONDITIONS (A/C LOAD)
- DFW ELECTRICAL LOAD – CONSTANT 25 KW ELECTRICAL LOAD

ETC011979-56

FIGURE 2.2.6.1 TOTAL SYSTEM ANALYSIS

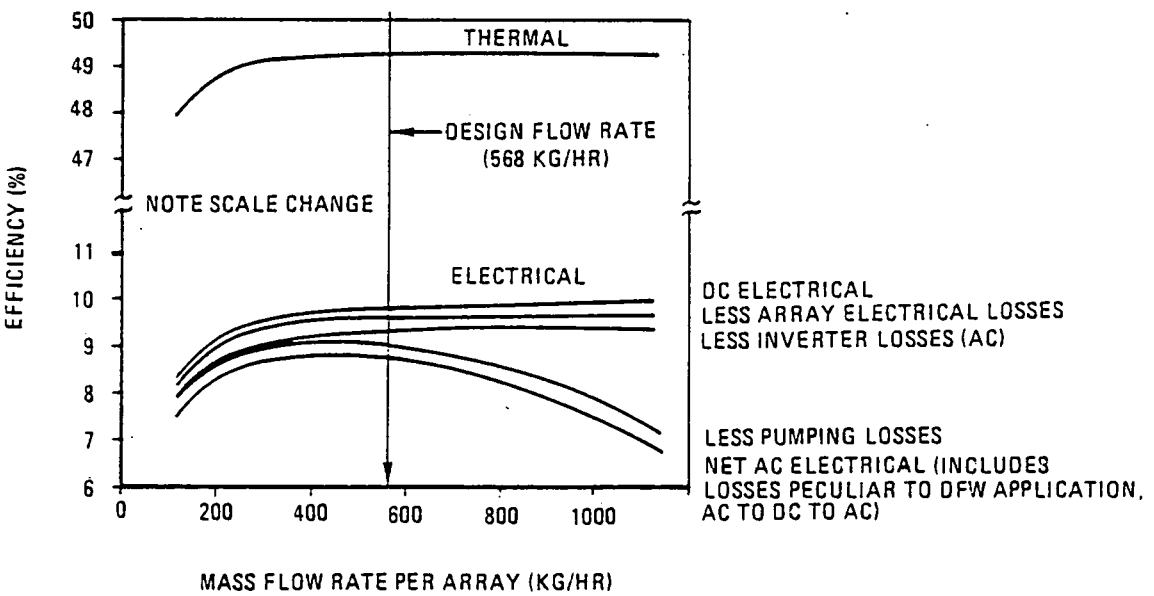

ETC011979-21

FIGURE 2.2.6.2
ANNUAL SYSTEM EFFICIENCY VS. FLOW RATE

corresponding to peak electrical was not selected because fluid temperatures exceeding 220°F (104°C) were experienced several times throughout the year at this flow rate, presenting possible fluid boiling problems.

Figure 2.2.6.3 presents whole-day electrical and thermal performance for a typical operating day. Due to roll-tilt tracking the output curves closely match the direct normal insolation curve. For this typical whole-day operation, 47.9% of the available insolation is converted to useful thermal output and 9.8% is converted to DC electricity.

The annual system performance results are presented in Figure 2.2.6.4. On a yearly basis, array tracking losses and module to module shading reduce the available insolation by 11.8%. Additionally, in the electrical conversion process a 3% loss is incurred due to shading effects of the lower and upper three photovoltaic cells in each module. This loss factor is fully described in Section 3.1.4. This reduces the available direct normal insolation to 85.6%. Transmittance losses ($\tau = 0.85$) further reduce this value to 72.8% (.85 x .856). The cell annual average conversion efficiency (13.1%) reduces the total to 9.51%. Of the 9.51% converted to DC electrical energy, cell mismatch and wiring series resistance losses lower the total to 9.3%. The inverter efficiency (97%) further reduces the total to 9.0%. Parasitic losses associated with fluid pumping, module tracking and electronic component operation amount to 3% of output power. At this point, 8.7% of the annual available energy is available as AC electricity. The final loss factor relates to the utility supplemental power losses in the rectifier and inverter. Supplemental utility power required to augment the photovoltaic output power to match the load is not used directly because parallel AC generation is prohibited by local utility regulation (Section 2.1). This requires the supplemental utility power to be rectified to DC, mixed with the DC output of the photovoltaic array and then inverted to AC electricity. The rectifier efficiency varies

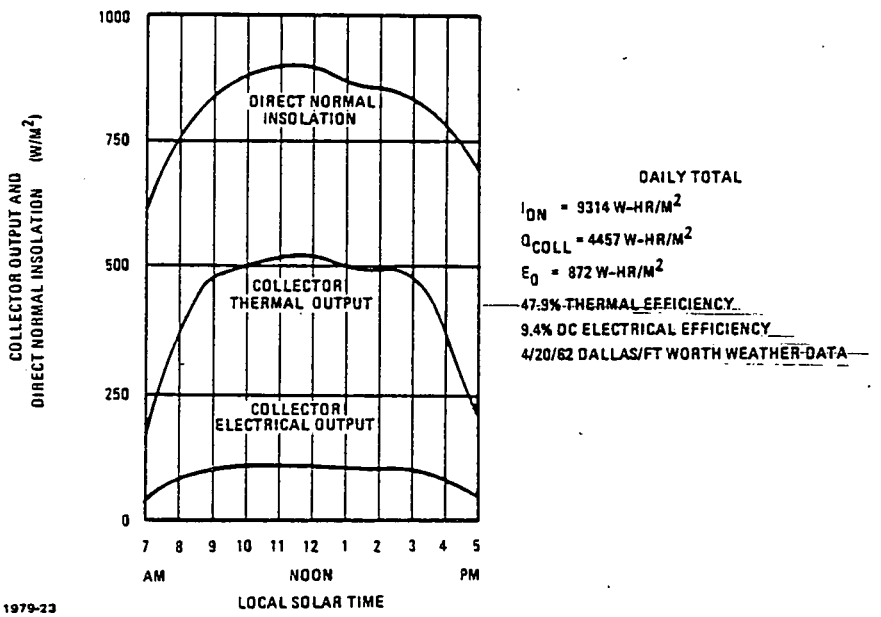

FIGURE 2.2.6.3 DAILY THERMAL/ELECTRICAL PERFORMANCE

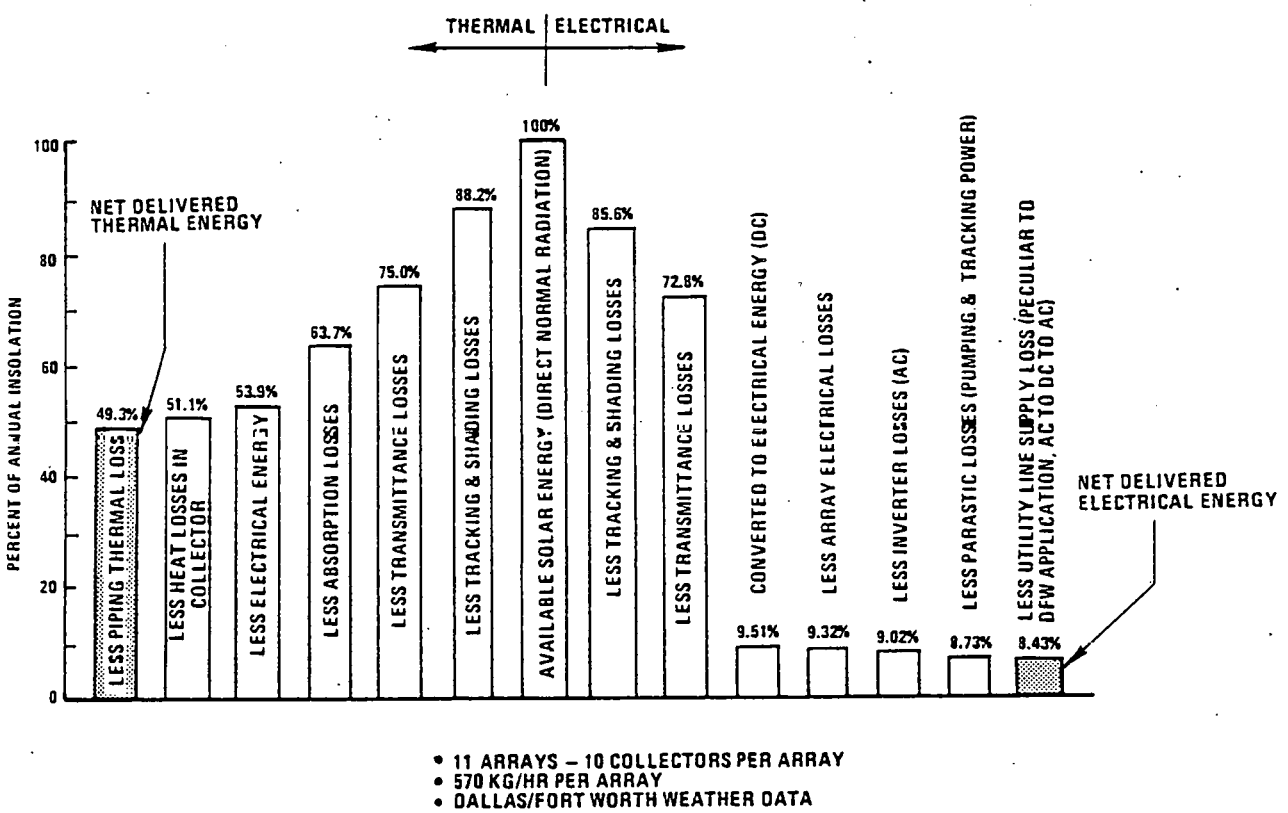

FIGURE 2.2.6.4 ANNUAL SYSTEM PERFORMANCE

with the amount of auxillary utility power required and is fully described in Section 3.2. On an annual basis this AC to DC to AC power processing results in a supplemental line power loss equal to 3.5% of the net solar electric power delivered. Incorporating this parasitic loss, the net annual conversion of direct normal insolation to AC electricity is 8.4%.

On the thermal side of Figure 2.2.6.4, the 3% loss due to cell shading effects is not included in the tracking and shading losses as it is due to inherent electrical characteristics of the cells and their diode protection and was treated on the electrical side of the figure. The 11.8% tracking and shading loss reduces the total to 88.2%. Of this total, 85% is transmitted through the lens and is incident on the photovoltaic receiver module. Absorption of the incident concentrated flux by the photovoltaic receiver ($\alpha = .85$) further reduces the total to 63.7%. The annual DC electrical output of the cells (9.51%) is subtracted leaving 53.9%. Next, annual radiant, convective and conductive receiver thermal losses lower the total to 51.1%. Finally, piping thermal loss reduces the net thermal energy delivered to the DFW thermal load to 49.3% on an annual basis.

In summary, the proposed Fresnel/photovoltaic/photothermal power system converts 8.4% of the annual direct normal insolation to AC electricity and 49.3% to thermal output. Thus, approximatly 58% of the available insolation is delivered as useful thermal and electrical energy.

While the results presented in Figure 2.2.6.4 are based on the Aerospace weather model, a similar performance analysis was conducted using the TMY model. The annual available direct normal insolation predicted by the Aerospace model (2340 kw-hr/m^2) is 33% greater than that predicted by TMY (1770 kw-hr/m^2). The net effect of the TMY data on performance is to increase slightly the annual electrical and thermal system efficiencies (to 8.78% and 51.6%, respectively) and to decrease the annual amount of delivered AC electrical and thermal energy in direct proportion to the annual insolation.

While both models predict essentially the same annual system efficiency, a question arises as to the total amount of direct normal insolation in the Dallas/Fort Worth area.

Neither model is based upon site-measured direct normal insolation, and thus both are subject to question. One apparent anomaly in both models is the high number of daylight hours with positive readings of direct normal insolation. The Aerospace model indicates 82% of the daylight hours have some direct normal insolation, while the TMY model indicates 95%. Since direct normal insolation is zero during cloudy periods, both of these values appear high. Only long-term actual measurements will resolve this discrepancy and refine annual output prediction accuracy.

2.3 System Performance Summary

Table 2.3.1 summarizes the performance of the DFW Airport Photovoltaic Concentrator Experiment. The peak system output is 25 kw of net alternating current power derived from solar energy. The peak thermal output is 140 kw_t of net boiler heat savings. On an annual basis, the net system outputs are shown to be 48 megawatt-hours and 280 megawatt-hours of electricity and heat respectively. The concentrator module used in the application is E-Systems short focal length linear Fresnel lens, coupled with OCLI silicon cells. A roll-tilt tracking scheme is utilized. Both electric and thermal loads are continuous and located within the Central Utility Plant. The collector array consists of 11 ten-module array assemblies, providing 245 m^2 of aperture. Peak system efficiencies are 10.2% and 56%, electric and thermal respectively. Annual efficiencies are 8.4% and 49%. Thus, about 58% of the annual direct normal insolation available to the system will be converted to useful energy output.

PEAK ELECTRICAL OUTPUT	25KW$_e$ AC (NET UTILITY SAVINGS)
PEAK THERMAL OUTPUT	140 KW$_t$ (NET FUEL SAVINGS)
ANNUAL ELECTRICAL OUTPUT	48,000 KW-HR$_e$ (NET UTILITY SAVINGS)
ANNUAL THERMAL OUTPUT	280,000 KW-HR$_t$ (NET FUEL SAVINGS)
CONCENTRATOR	E-SYSTEMS 91 CM WIDE X 244 CM LONG LINEAR 45° RIM ANGLE FRESNEL LENS (85% NET TRANSMITTANCE)
CELLS	OCLI SILICON CELLS (13.4% AT 55°C)
CONCENTRATION RATIO	25 (91.4 CM APERTURE TO 3.66 CM CELL WIDTH)
TRACKING	ACTIVE DIURNAL TRACKING, PERIODIC TILT ADJ.
ELECTRIC LOAD	CONSTANT 25 KW LIGHTING WITHIN UTILITY PLANT
THERMAL LOAD	CONTINUOUS 29° – 35° C CONDENSATE WATER FLOW (BOILER FEEDWATER)
COLLECTOR ARRAY SIZE	11 ARRAYS, 110 COLLECTOR MODULES, 245 M^2 TOTAL APERTURE
PEAK EFFICIENCY	10.2% ELECTRIC (INSOLATION TO NET AC OUTPUT), 56% THERMAL
ANNUAL EFFICIENCY	8.4 % ELECTRIC (INSOLATION TO NET AC OUTPUT), 49% THERMAL

ETC011979-53

TABLE 2.3.1 SYSTEM PERFORMANCE SUMMARY

	REQ'D PER SITE	COST PER SITE	$/FT^2	$/M^2
COLLECTOR MODULE ASSY (W/O RECEIVER)	100	9933.20	4.14	44.56
PHOTOVOLTAIC RECEIVER ASSY	100	26500.00	11.04	118.83
TILT DRIVE ASSEMBLY	10	5065.70	2.11	22.71
ROLL DRIVE ASSEMBLY	10	1354.70	.56	6.03
FRAME & INTERFACE COMPONENTS	10	6212.60	2.59	27.88
TRACKING & CONTROL				
ROLL AXIS	10	384.60	.16	1.72
TILT AXIS	1	65.32	.03	0.32
PLUMBING		1200.00	.50	5.38
ELECTRICAL		1200.00	.50	5.38
HARDWARE		200.00	.08	0.86
SHOP LABOR		935.00	.39	4.20
PREPARATION FOR SHIPPING		555.00	.23	2.48
SHIPPING (TYPICAL 100 MILE RADIUS)		1000.00	.42	4.52
SITE PREPARATION		200.00	.08	0.86
FOUNDATION		2400.00	1.00	10.76
INSTALLATION & ALIGNMENT		4800.00	2.00	21.53
TOTAL DIRECT COST		62006.12	25.84	278.02
INDIRECT COSTS				
• LABOR OVERHEAD @ 100% OF DIRECT LABOR COST		990.00	0.41	4.41
• MATERIAL BURDEN @ 3% OF DIRECT MATERIAL COST		1830.00	0.76	8.18
• GENERAL & ADMINISTRATIVE @ 25% OF COST ADDITIONS		952.00	0.40	4.31
• FEE @ 10% OF COST		6577.86	2.74	29.49
TOTAL INSTALLED PRICE		72356.48	30.15	324.41

- BASED ON ANNUAL PRODUCTION OF 2,000 ARRAYS (500,000 FT^2) (46,000 M^2)
- BASED ON A TYPICAL SITE DEFINED AS:
  - 10 ARRAYS, SERIES HOOK-UP
  - 1 CONTROL CENTER
  - FIELD INSTALLED (AS OPPOSED TO ROOF INSTALLATION)
  - 3000 PSF SOIL
  - MINIMUM SITE PREPARATION

ETC011979-55

TABLE 2.4.1 COLLECTOR PRODUCTION COST ESTIMATE (1978 $)

2.4 System Economics Summary

To define the near-term economic viability of a production-version system similar to the DFW Airport Experiment, a detailed estimate of the installed price of such a system was completed during Phase I. Table 2.4.1 summarizes this price estimate, based upon an assumed system configuration of ten arrays of ten modules each for a total system aperture of $223m^2$, installed on a ground-level site as noted. An annual production rate of $46,000m^2$ was used for quantity estimates. The cost element with the highest uncertainty is the photovoltaic receiver. It was estimated based upon a laid-down cell cost of $5 apiece, or $30¢/cm^2$ of cell area. The total installed price of $\$30/ft^2$ ($\$324/m^2$) is closely in line with E-Systems' target price of $\$20/ft^2$ ($\$215/m^2$) for a purely thermal version of the Fresnel collector, since the difference in price between the photovoltaic receiver and the thermal receiver is about $\$10/ft^2$ ($\$108/m^2$). Using the annual efficiencies defined in Section 2.3, the cost estimate of Table 2.4.1, and the economic factors listed in Table 2.4.2, a levelized energy cost analysis was conducted. The first set of economic factors in Table 2.4.2 was prescribed by DOE for all PRDA-35 contractors, while the second set corresponds to actual conditions at DFW Airport.

Levelized energy costs were determined in two different ways:

- The thermal and electrical energy costs were calculated separately, based upon a system cost allocation of 1/3 to the electrical energy and 2/3 to the thermal energy. These costs are shown on the right-hand axis of Figure 2.4.1.
- The thermal energy was converted to equivalent electrical energy by assuming a 30% conversion efficiency. This equates to valuing heat at 30% of the value of electricity. The combined equivalent electrical energy was then costed out as shown on the left-hand axis of Figure 2.4.1.

Since annual energy production is proportional to annual insolation, the levelized energy costs are shown as functions of "Percent Clear Days". This parameter is based upon ASHRAE clear day direct normal insolation data. 100% clear days corresponds to 3250 kw-hr/m^2 annual direct normal insolation.

	SUGGESTED	D/FW CASE
SYSTEM OPERATING LIFE	20 YEARS	20 YEARS
ANNUAL OTHER TAXES AS FRACTION OF CAPITAL INVESTMENT	.02	.02
ANNUAL INSURANCE PREMIUMS FRACTION CI	.0025	.0025
EFFECTIVE INCOME TAX	.50	–
RATIO DEBT	.50	1.0
RATIO COMMON STOCK	.40	–
RATIO PREFERRED STOCK	.10	–
RATE OF RETURN DEBT	.10	.065
RATE OF RETURN COMMON	.12	–
RATE OF RETURN PREFERRED	.10	–
GENERAL INFLATION	.07	.07
FIRST YEAR COMMERCIAL OPERATIONS	1980	1980
ESCALATION CAPITAL AND OPERATING & MAINTENANCE	.07	.07
BASE YEAR FOR CONSTANT DOLLARS	1975	1975

ETC011979-59

TABLE 2.4.2 ECONOMIC FACTORS

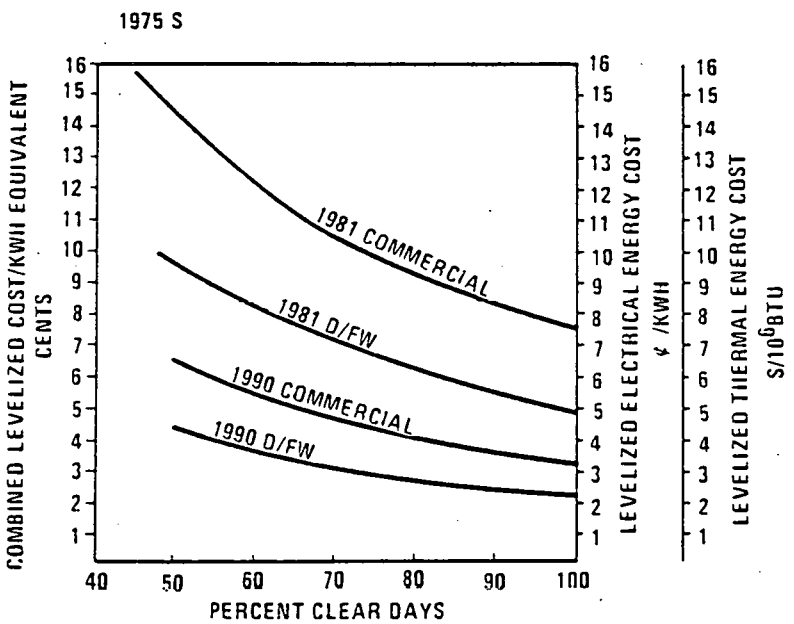

ETC011979-38

ASSUMPTIONS:
- ECONOMIC FACTORS OF TABLE 2.4.2
- COLLECTOR COST IN 1981 FROM TABLE 2.4.1
- O&M COST AT 1% OF CAPITAL INVESTMENT PER YR.
- PCU COST IN 1981 AT $250/KW
- 1990 COSTS ASSUME 90% LEARNING CURVE ON COLLECTORS AND CELLS WITH 5MW INSTALLED IN 1981, AND 10 Mw/YEAR THEREAFTER
- 1990 COSTS ASSUME CONCENTRATION RATIO OF 50
- COMBINED HEAT & ELECTRIC ENERGY COST VALUES HEAT AT 30% OF ELECTRICITY
- SEPARATE HEAT & ELECTRICITY COST BASED UPON SYSTEM COST ATTRIBUTED 1/3 TO ELECTRICAL ENERGY AND 2/3 TO HEAT

FIGURE 2.4.1 COST OF ENERGY

There is a lack of measured data for direct normal insolation in the Dallas/Fort Worth area, as discussed in Section 2.2. However, the value estimated by Aerospace Corporation (Referenee 5) corresponds to 72% clear days in Figure 2.4.1. The appropriate energy costs for the commercial system in 1981 (corresponding to the DOE-generated economic factors) are about 10¢/kwh (equivalent) or 10¢/kwh (electric) and $10/MMBtu (thermal). The DFW Airport 1981 curve (corresponding to actual economic factors) yields 7¢/kwh (equivalent) or 7¢/kwh (electric) and $7/MMBtu (thermal). Over the 20-year life cycle of the system, these values are competitive with conventional energy costs if conventional costs rise at moderate rates.

While near-term economic viability for the system appears excellent, if long-term mass production were carried on over a period of years, the usual learning curve decrease in system costs should be realized. To estimate these reduced costs, 90% learning curves were applied to collector costs and cell costs, based upon the volume assumptions given on Figure 2.4.1. Additionally, a concentration ratio increase to 50 from the current 25 was assumed, based upon the lens analyses and tests conducted during Phase I. The resultant levelized energy costs are presented as the lower two curves of Figure 2.4.1, for the two sets of economic factors previously discussed. Note that the levelized energy costs for 72% clear days (Dallas/Fort Worth area) fall to the 3-5¢/kwh (equivalent) or 3-5¢/kwh (electric) and $3-5/MMBtu (heat), depending on which set of economic factors are applicable. These values are competitive with today's conventional energy costs and would thus be far less than conventional energy costs over the 20 year system life cycle.

In summary, the proposed system design represents an economically viable total energy source in the near-term, with increasing viability in the long term.

3.0 COMPONENT SPECIFICATION

3.1 Photovoltaic Array

3.1.1 Photovoltaic Array Specification

The system is comprised of eleven photovoltaic array assemblies (FIG. 3.1.1) each of which consists of ten collector modules mounted in a structural frame, with appropriate tracking and drive facilities (FIG. 3.1.2). In each array the modules are interconnected in series hookup, both electrically and thermally, to produce nominally 2.5 KW_e of DC power and 13 KW_t thermal per array. The eleven arrays are interconnected in parallel to provide approximately 27 KW_e of DC power at 260 volts, nominal, to the power conditioning equipment for conversion to useable AC. The cooling fluid system of the arrays is similarly connected in parallel to produce about 140 KW_t of thermal power to the heat transfer system, where it is coupled into the airport boiler feedwater system.

The photovoltaic system has been designed to be compatible with a realistic environment as defined in the specification listed below:

- Design Environment

	Operational	Survival (Stow Position)
Wind	30 MPH (13.4 mps) gusting to 45 mph (20 mps)	90 MPH (40.2 mps)
Temperature	-20°F to 120°F (-27°C to +49°C)	-40°F to +140°F (-40°C to +60°C)
Humidity	0 to 100%	0 to 100%
Rain	-	2 In./Hour(5cm/hr)
Snow	-	12 In. Accumulation (30 cm
Ice	-	1 In. Radial (2.5 cm)
Hail	-	1 In. Dia.-Terminal Velocity (2.5 cm)
Seismic	-	0.25G Lateral Acceleration

- Design Life

  20 year operational life span requiring only normal maintenance.

In Table 3.1.1 the key elements of each of the major components and/or sub-assemblies of the photovoltaic array are described. Since the drawing package defines in detail all specification criteria, it is the primary procurement and manufacturing specification and as such is referenced for detailed design and specification data.

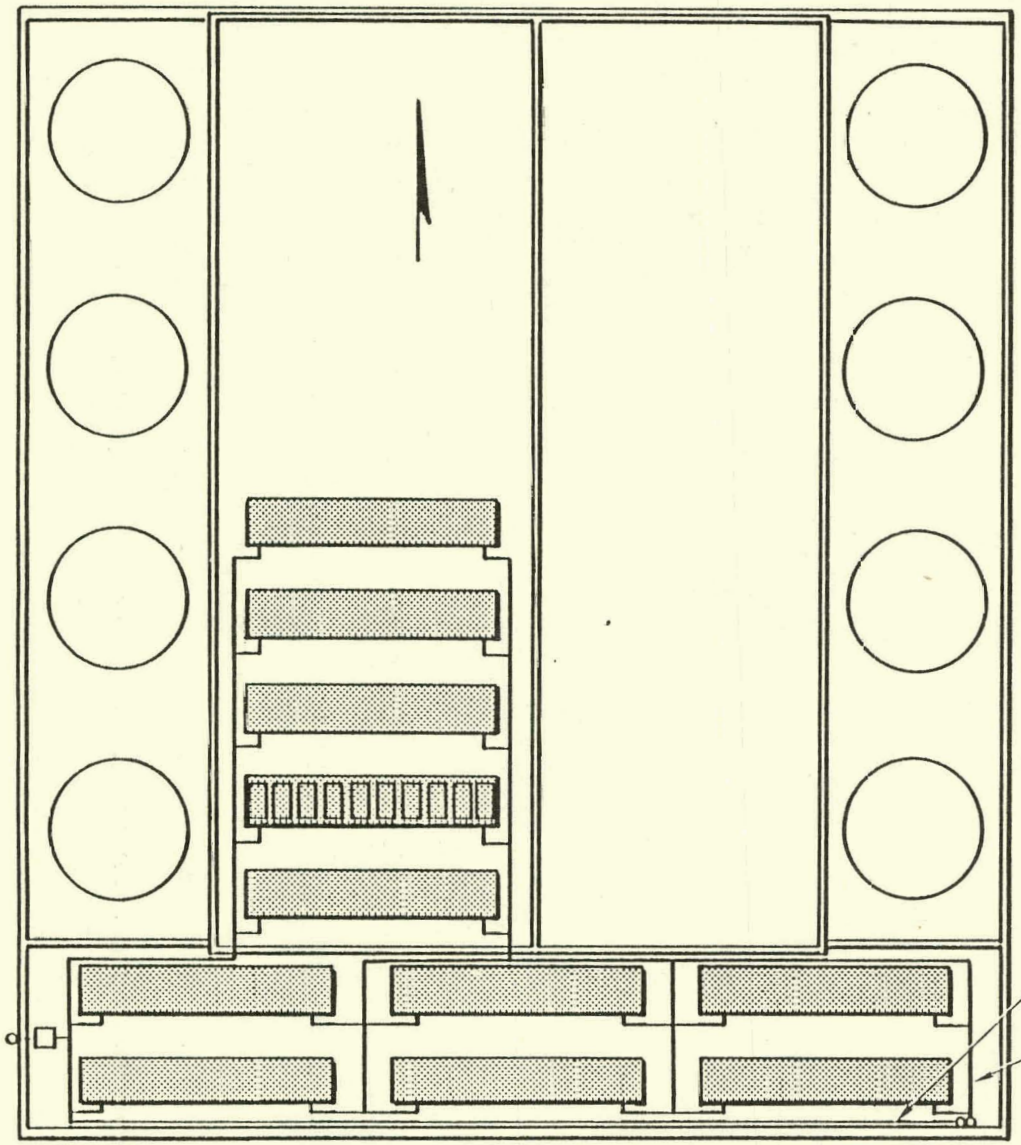

ETC011979-37

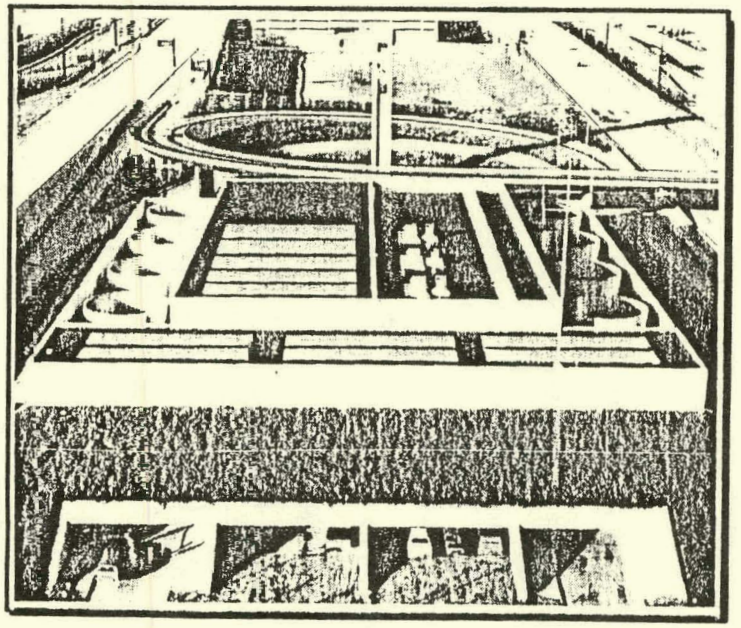

FIGURE 3.1.1 SYSTEM INSTALLATION

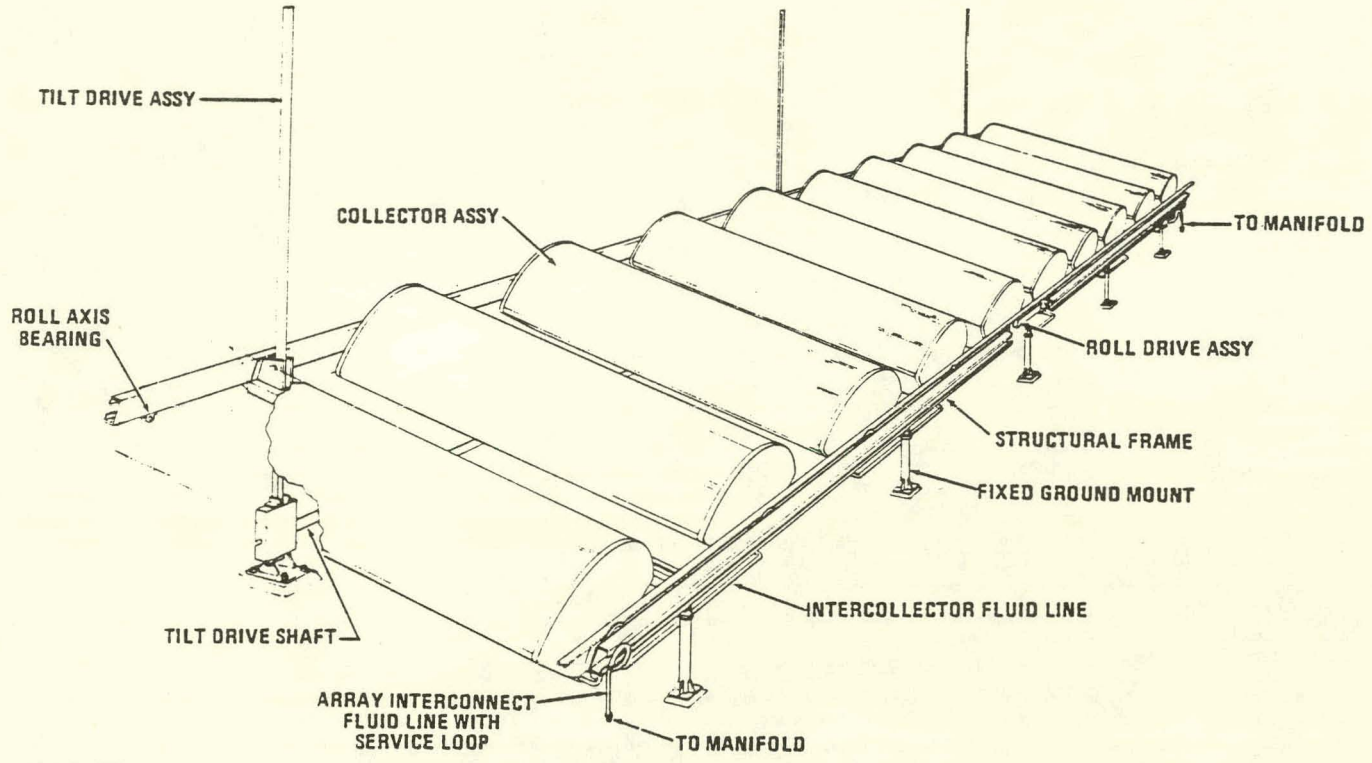

FIGURE 3.1.2 ARRAY ASSEMBLY

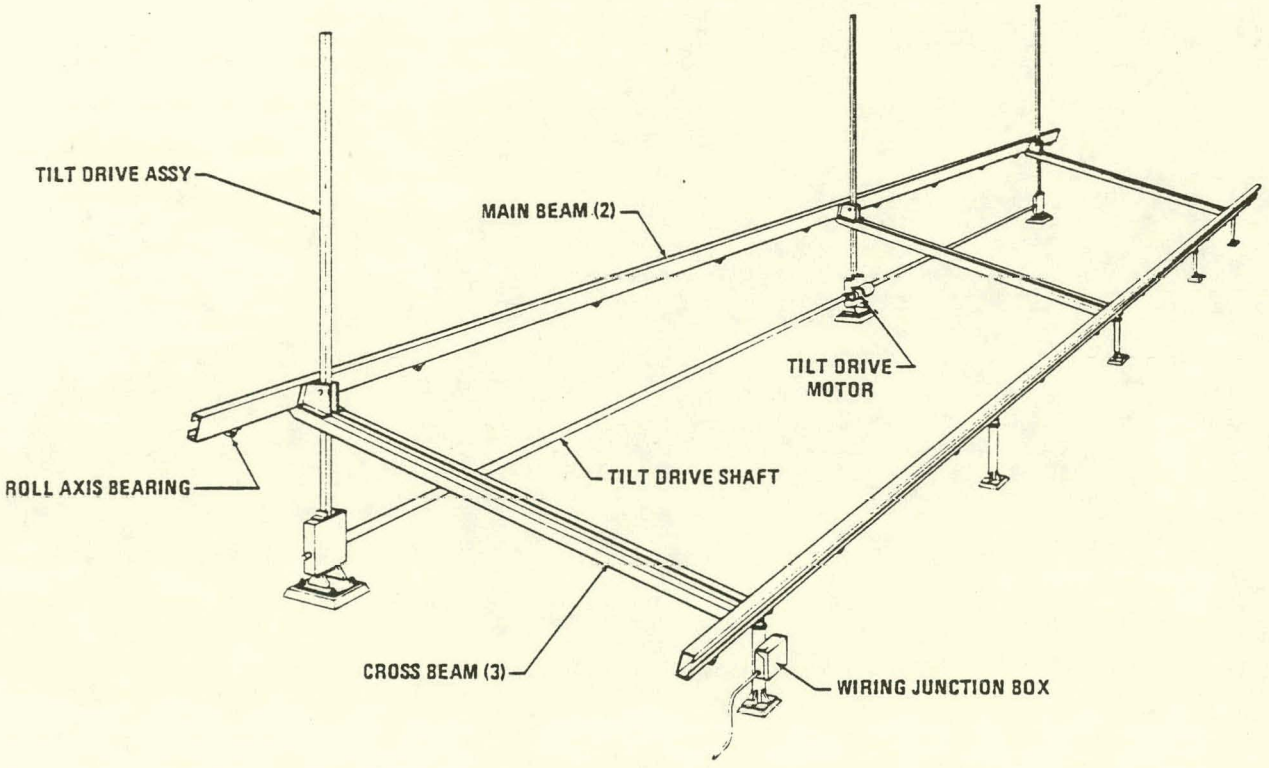

FIGURE 3.1.3 STRUCTURAL FRAME TILT DRIVE ASSY

COMPONENT	DESCRIPTION	WT. (LBS) PER ARRAY ASSY
COLLECTOR MODULE		1278
HOUSING STRUCTURE	• 10 MODULES PER ARRAY.	
	• GALVANIZED SHEET STEEL CONST.	
	• INTEGRAL ROLL AXIS SHAFT OR AXIAL CG	
	• ROLL AXIS DRIVE SHEAVE INTEGRAL WITH END PLATE	
	• ENVIRONMENTAL LENS & JOINT SEALS	
LENS	• 3 MM THK CURVED ACRYLIC FOR WHOLE APERTURE	
RECEIVER ASSY	• 53 SILICON SOLAR CELLS MOUNTED IN SERIES ON COPPER HEATSINK	
	• COPPER HEATSINK BRAISED TO A 15MM DIA COPPER TUBE	
	• POLYURETHANE INSULATION BETWEEN RECEIVER AND HOUSING	
	• SUPPORTED ALONG FULL LENGTH OF HOUSING	
DRIVES		358
ROLL AXIS DRIVE	• 5 WATT, AC-PULSE DRIVE	
	• SINGLE LINEAR ACTUATOR PER ARRAY	
	• CLOSED LOOP ACTIVE TRACKING IN SINGLE DIRECTION	
	• 150° SKY COVERAGE	
	• SLEW SPEED – 5°/MIN.	
TILT AXIS DRIVE	• 50 WATT, AC DRIVE	
	• THREE (3) LINEAR ACTUATORS DRIVEN BY COMMON SHAFT	
	• MANUAL JOG CONTROL FOR PERIODIC ADJUSTMENT	
	• REMOTE TILT POSITION INDICATION	
	• SLEW SPEED – 1¾°/MIN.	
ARRAY STRUCTURE	• HIGH STIFFNESS/WEIGHT RATIO SHEET STEEL FRAME	883
	• APPROX. 14.6M X 3.0M	
	• TILT AXIS AT SOUTH FACE	
INTERFACES	• SELF ALIGN BEARINGS FOR MODULE/ FRAME MOUNT	25
	• TEN MODULES WIRED IN SERIES TO PROVIDE 260 VDC OUTPUT	
	• TEN MODULES PLUMBED IN SERIES FOR COOLANT FLUID FLOW	
		TOTAL ARRAY WEIGHT 2544 LBS.
ETC011979-58		WEIGHT/APERTURE 10.6 LBS/FT^2

TABLE 3.1.1 PHOTOVOLTAIC ARRAY COMPONENT SPECIFICATION

The two most critical items of the system are the lens and the photovoltaic receiver. Vendors have been tentatively designated for these items:

- Lens: Swedlow, Inc., is currently providing prototype quantities of cast lenses to E-Systems under company funding. From schedular considerations, they are the leading candidate lens supplier for Phase II. However, E-Systems is developing an extrusion/embossing mass production technique under Sandia Contract No. 13-2359. If acceptable lenses are available from this program in time to meet Phase II requirements, they will be used instead of cast lenses. Furthermore, additional lens vendors, including 3M Company, are working on other production processes under E-Systems funding and will be considered as Phase II suppliers.
- Photovoltaic Cell Assembly: OCLI designed and fabricated the prototype photovoltaic cell assembly which was successfully tested during Phase I. Thus, they are the leading candidate cell supplier for Phase II.

Figures 3.1.3 and 3.1.4 are provided for ease in identification of the major elements comprising the structural frame and the collector module, respectively. The category identified as "Housing Structure" in Table 3.1.1 includes the asterisked items in Figure 3.1.4.

As part of the in-house E-Systems-funded program, a single test array was constructed as shown in Figure 3.1.5. All structural aspects of the frame and collector modules are identical to the photovoltaic array configuration with the exception of the ground mount. In this case it was necessary to elevate the array to achieve a clear solar line of sight. It should also be noted that no lenses are included in the installation. Masonite covers have been substituted on each of the modules for simulation of weight and overturning moments.

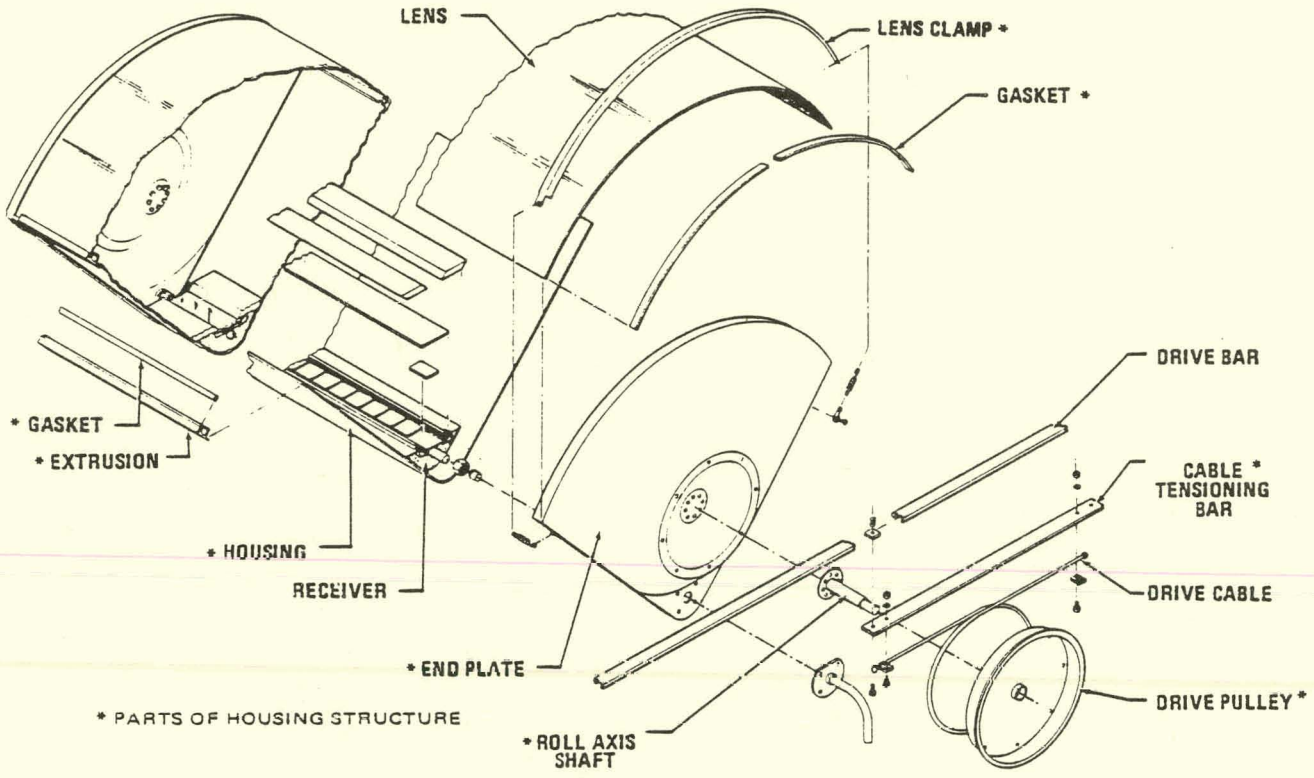

FIGURE 3.1.4 COLLECTOR ASSEMBLY

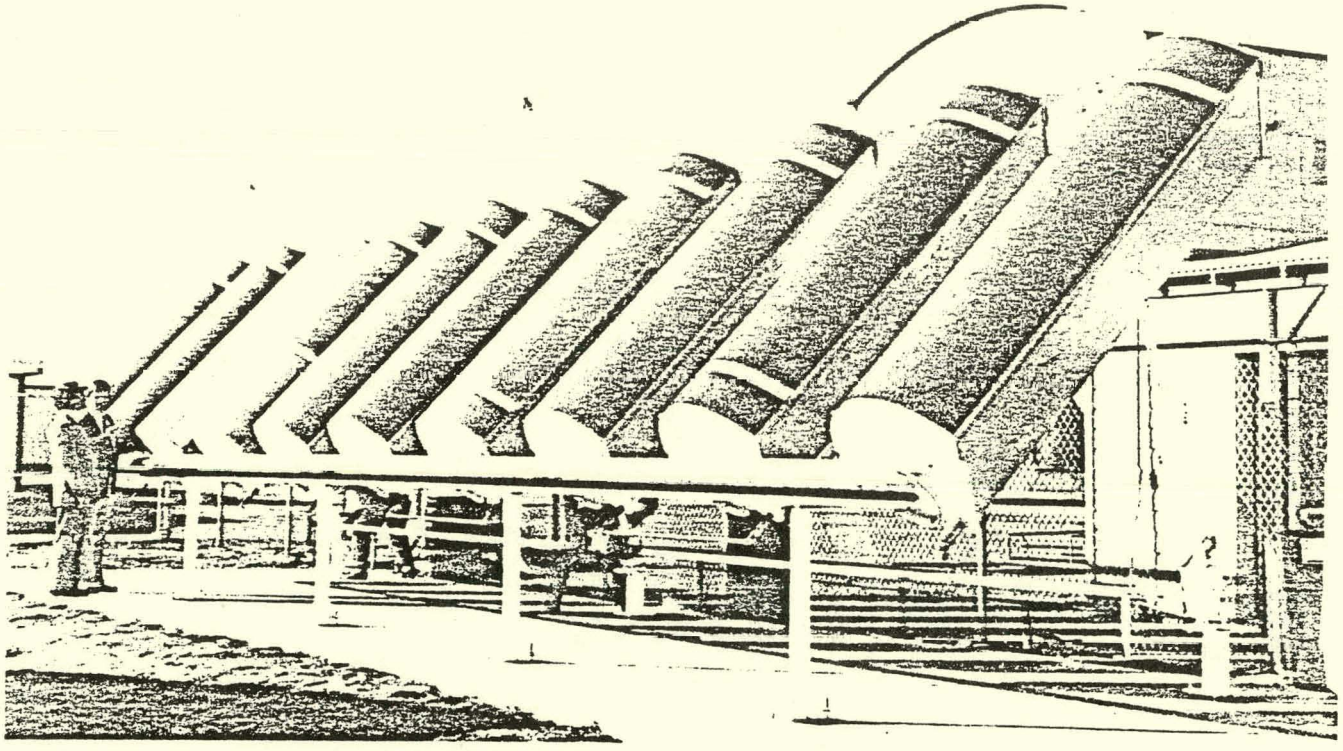

FIGURE 3.1.5 E-SYSTEMS FUNDED TEST ARRAY

The test array has been used to verify the structural and mechanical design. Clearances, tolerances, deflections, drives, installation and alignment techniques, and environmental survival characteristics have been checked and measured as applicable and modifications made where required. The drawing package reflects the latest design criteria resulting from the array testing.

3.1.2 Prototype Fresnel/Photovoltaic Concentrator Development and Testing

To verify the predicted performance of E-Systems Fresnel/Photovoltaic collector, a prototype collector was designed, fabricated and successfully tested during Phase I. Photographs of the prototype collector and receiver are presented in Figures 3.1.6 and 3.1.7. The prototype design is representative of the proposed production collectors with two major exceptions:

- The prototype lens is a parquet of 36 small compression-molded acrylic lens elements rather than the full-size, single-piece cast acrylic lens planned for use in Phase III. However, the parquet lens is a full three feet (91.4 cm) in aperture width by eight feet (244 cm) in length. Furthermore, the same master tooling used to press the parquet lens elements is also being used to make electroform tooling for the full-size Phase II cast lenses. Thus, the prototype optical performance should be the same as the production lens optical performance.

- Because shadows are formed by the lateral ribs supporting the parquet lens, gaps were provided between cells at shadow points along the prototype photovoltaic receiver. Also, because of test stand length limitations, a shorter receiver was used for the prototype than planned for Phase II production units. The combined effect of these constraints was to limit the number of cells to 46 rather than 53. Since each cell is 1.78 inches (4.52 cm) long and requires a 0.030 inch (0.076 cm) space between it and the next cell, the integrated length of the prototype cell string including spaces is 46 x 1.81 inches = 83.3 inches (212 cm), compared to 53 x 1.81 inches = 95.9 inches (244 cm), for the production receiver. Thus the output power for the prototype is only $\frac{46}{53}$ or 86.6% of that for the production collector. For efficiency calculations, the effective aperture area is defined to be the cell string integrated length (83.3 inches) times the full aperture width (36 inches), or 20.83 ft^2 (1.935 m^2). No reduction in aperture was treated for longitudinal joints between lens parquet elements or for bolts used to hold these elements together. The prototype cells are identical to those which will be used for the Phase II production collectors.

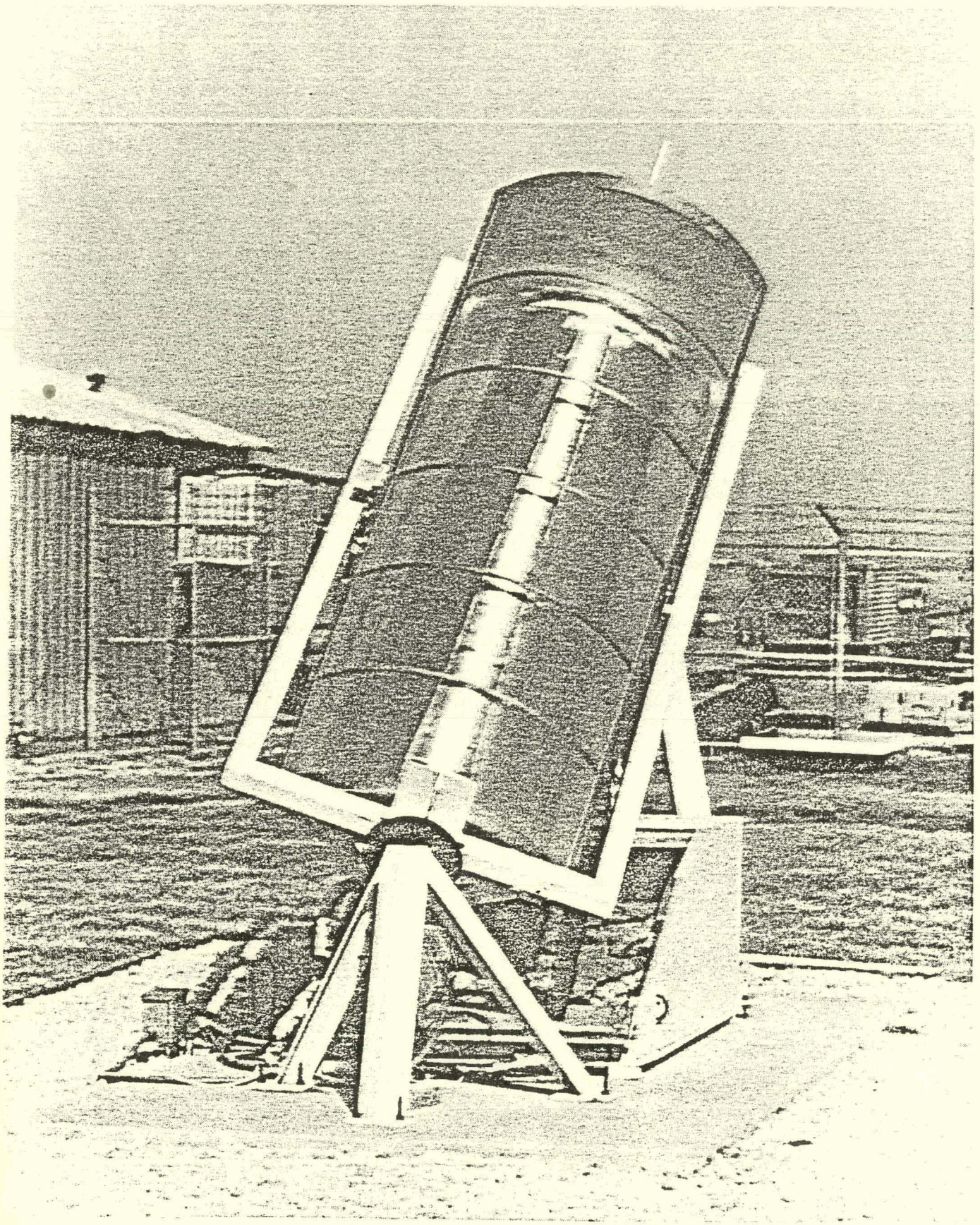

Figure 3.1.6 - Prototype Collector

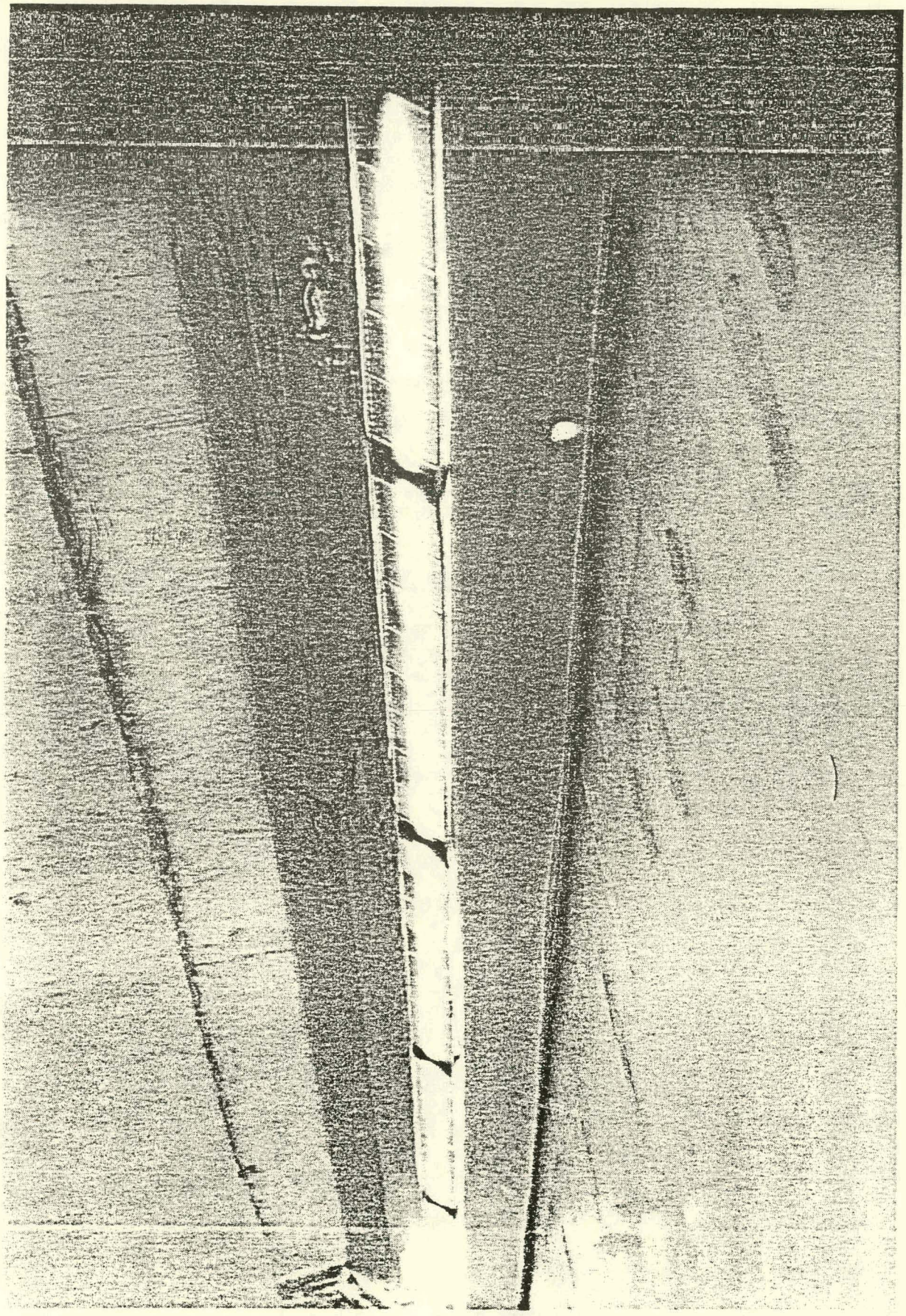

Figure 3.1.7 - Prototype Receiver

The prototype collector was installed in E-Systems Fresnel Collector Test Facility which was previously built under company funding. This facility includes highly accurate instrumentation for collector performance evaluation, including:

- A complete weather station including wind speed and direction, an Eppley normal incidence pryheliometer calibrated by NOAA, ambient temperature, etc.
- A turbine flowmeter and digital display calibrated and checked at 0.5% accuracy.
- Platinum resistance sensors and bridges for collector water inlet, outlet, and differential measurement. These devices have been calibrated and checked at 0.03°F accuracy.
- A recently calibrated shunt resistor for measuring the photovoltaic cell string current to 0.1% accuracy.
- Digital voltmeters accurate to the 1μ volt level for monitoring insolation, temperatures, voltages and currents in the test collector.
- A wattmeter for monitoring power output from the photovoltaic string within 1% accuracy.
- A solid-state variable resistance circuit simulator with high stability for performing voltage/current curve measurements.

This test system was used to perform a variety of tests, including lens optical performance measurements, collector thermal efficiency tests, collector electrical efficiency tests, total collector efficiency tests, and current/voltage characteristic curve tests for the photovoltaic collector. These tests and their results are described below.

The optical performance of the Fresnel lens concentrator can be specified in terms of two parameters: concentration ratio and transmittance. The geometric concentration ratio selected for the collector is 25, including the effects of all errors (tracking, manufacturing, deflection, etc.). Thus the cell active width was set at 1.44 in. (3.66 cm) for the 36 in. (91.44 cm) wide lens. The prototype lens easily met this focussing requirement, as the image photograph of Figure 3.1.7 shows. Visual inspection indicates that

nearly all of the image is contained within 1/2 of the cell width (about 0.72 in. (1.83 cm)); thus the lens is achieving about a 50:1 concentration ratio as theoretically predicted (Section 2.2). The dark bands on either side of the bright image thus allow for sizable errors in tracking, alignment, deflection, etc., without allowing the image to move off of the cell. Also note from Figure 3.1.7 that the shadows caused by the lateral ribs in the parquet lens fall properly on the polished copper blanks where cells were omitted from the cell string. Regarding transmittance, the following test was performed to measure this important parameter.

It is well known that the short-circuit current of photovoltaic cells is directly proportional to the radiant flux incident upon such cells (Reference 7). Thus if this current is measured for the prototype receiver cells under one sun conditions (without the lens) and then under concentrated flux conditions (with the lens), the ratio of the latter to the former will be the net flux concentration (geometric concentration ratio times lens transmittance). The one sun test was performed as shown in Figure 3.1.8 with a black box mounted around the cells to allow all the direct normal insolation to impinge upon the cells, but blocking reflected radiation from the trough walls and blocking about 90% of the diffuse sky radiation. The short circuit current was measured for several insolation levels to define the flux/current proportionality constant. This constant was found to be 2033 w/m^2-ampere, as shown in Figure 3.1.9. Using this measured constant, all of the one sun data yielded a net concentration of 1.00 within 0.4% maximum error. Three such calibration points are shown on the lower curve of Figure 3.1.9. Next, several short circuit current tests were run with the lens in place. Using the previously defined proportionality constant, these

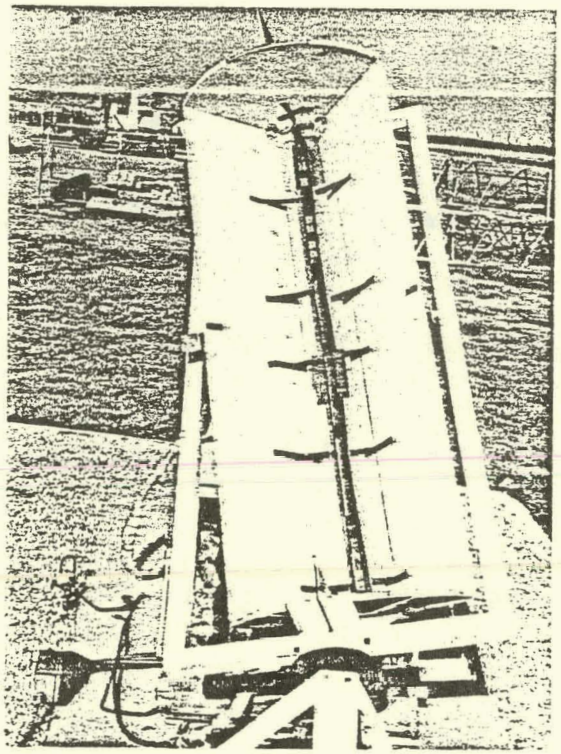

FIGURE 3.1.8 ONE SUN RECEIVER TEST

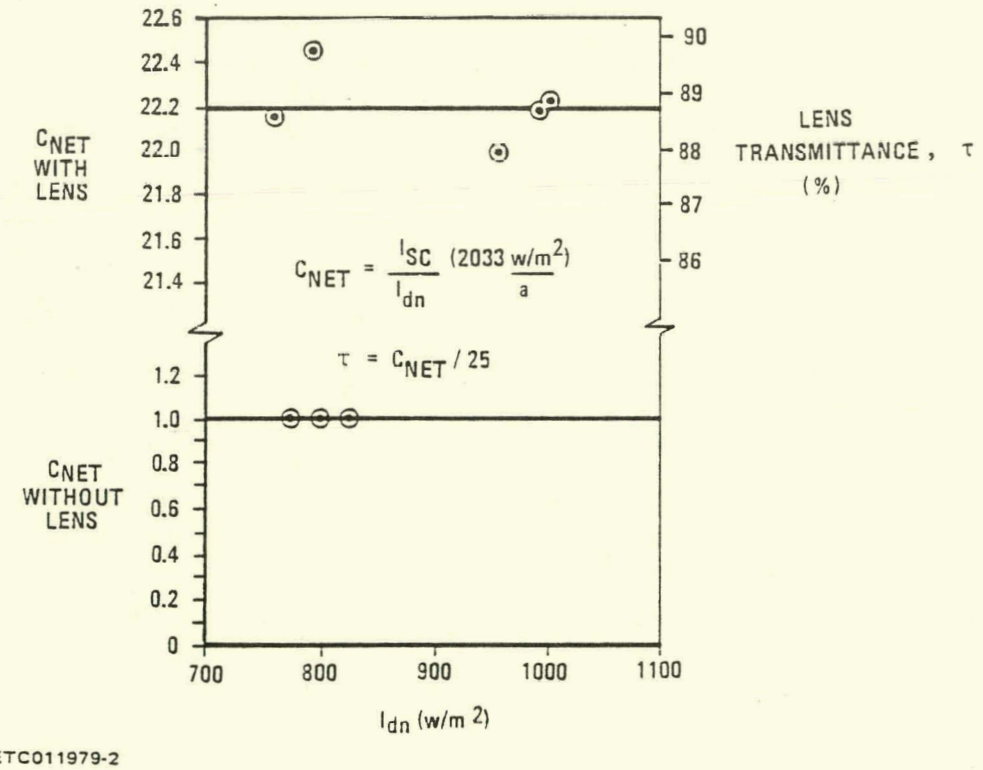

FIGURE 3.1.9
LENS OPTICAL PERFORMANCE TEST RESULTS

results all defined a net concentration of 22.2 ± 0.2 suns, despite insolation variations of 30%, as shown on the upper curve of Figure 3.1.9. Dividing net concentration by geometric concentration provides the net transmittance of the lens which was 89 ± 1%, as also shown on Figure 3.1.9. Thus, the lens exceeded the transmittance goal of 85%, as least over the silicon solar cell response spectrum. This higher value is not totally unexpected, since the absorption bands for acrylic are in the near infrared spectral region which is outside of the response spectrum of the silicon cells. The full solar spectrum transmittance is probably about 2% lower than the silicon cell spectrum transmittance due to this infrared absorption. Thus, the lens transmittance is slightly higher for photovoltaic applications (89%) than for photothermal applications (87%), and in both cases, the actual transmittance is higher than the original goal of 85%. In summary, the new lens performed excellently in the prototype tests, thereby confirming the theoretical performance predictions for this novel, optimized, short-focal-length concentrator.

Overall collector electrical efficiency and total efficiency (electrical + thermal) tests were also performed for a variety of conditions to verify the predicted collector performance. Figures 3.1.10 and 3.1.11 present the results of these tests. Since electrical efficiency is primarily a function of cell temperature, which is approximately 10°C higher than fluid temperature based on thermal analysis, Figure 3.1.10 presents measured overall collector electrical efficiency as a function of fluid temperature. Note that this electrical efficiency varies from about 13% at 15°C fluid temperature to about 9% at about 95°C fluid temperature.

To empirically verify the weatherability of the photovoltaic receiver, it was left in the prototype collector outside all winter. Data from tests conducted both before and after this 60-90 day exposure are presented in Figure 3.1.10 and indicate no degradation in electrical performance.

Collector total efficiency (electrical + thermal) is primarily a function of the usual thermal collector parameter ($\Delta T/I_{dn}$), wherein ΔT is the fluid-to-ambient temperature differential and I_{dn} is the direct normal insolation flux. Thus this total efficiency data is presented in Figure 3.1.11 as a function of ($\Delta T/I_{dn}$).

Data are again plotted for tests conducted immediately after receiving the photovoltaic receiver from OCLI, and for later tests conducted after 60-90 days of actual outdoor weathering of the receiver in the collector. Some slight variations are evident between the early data and the more recent data. However, this variation is attributed to the use of different instrumentation in the two series of tests, as further explained below.

During Christmas week, 1978, E-Systems plant was closed and the prototype collector was left unattended. During the week, Dallas experienced its worst ice storm in 30 years and the electric power to the plant was disrupted for at least several hours due to downed power lines. Since the test system uses electrical heating for freeze protection, this power outage allowed severe freezing to occur within the test loop, damaging the platinum resistance sensors, the turbine flow meter, and plumbing. In January, 1979, the system was repaired but backup differential thermocouples had to be used in place of the non-functioning platinum sensors, and the flowmeter had to be recalibrated yielding a slightly different calibration constant. The data points shown in Figure 3.1.11 before and after the 60-90 day exposure period, also correspond to before and after the ice storm and consequent change in instrumentation. Thus, the slight variation in these two sets of data is probably attributable to experimental error rather than to physical changes in the collector's performance.

When total efficiency is plotted as shown in Figure 3.1.11, the intercept of the curve yields the collector optical efficiency, $\tau\alpha F'$, wherein

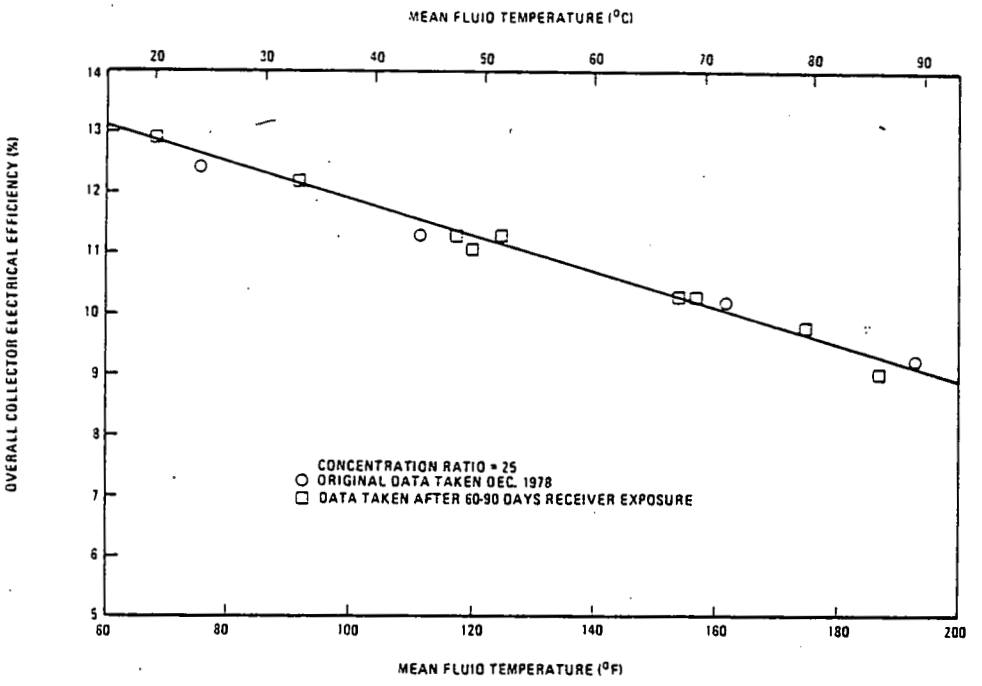

CONDITIONS: I_{dn} = 816–1003 W/M^2

M_{water} = 1.22–1.34 gpm (274–301 Kg/hr)

$T_{ambient}$ = 50–74 °F (10–23 °C)

FIGURE 3.1.10. TEST RESULTS FOR PROTOTYPE FRESNEL PHOTOVOLTAIC CONCENTRATOR

ETC032879-2

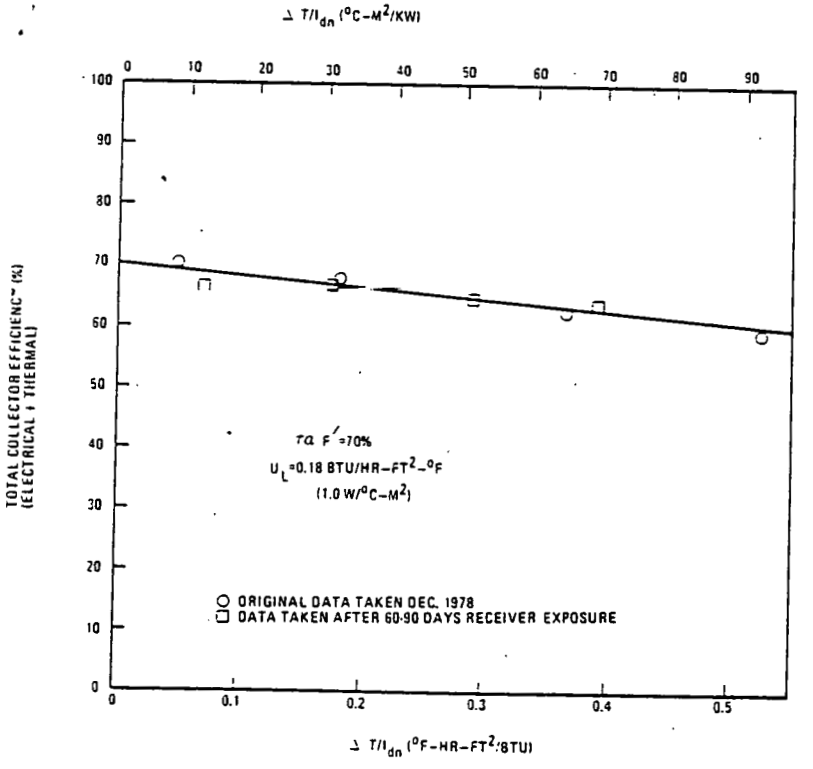

FIGURE 3.1.11. TOTAL EFFICIENCY OF PROTOTYPE FRESNEL PHOTOVOLTAIC CONCENTRATOR

τ is net lens transmittance, α is cell stack absorptance, and F' is receiver thermal effectiveness. For the prototype, the curve of Figure 3.1.11 yields about 70%. The predicted value (Reference 9) was:

$$\tau\alpha F' = (0.85)\ (0.85)\ (0.99) = 71.5\%$$

Thus the agreement between theory and test is excellent, although the slightly lower value measured is presumably due to the cell stack absorptance being lower than the estimated 85%.

The slope of the curve of Figure 3.1.11 yields the collector thermal loss coefficient, U_L. The measured value (0.18 Btu/hr-ft^2-$^\circ$F or 1.0 w/m^2°C) is slightly higher than predicted, but this effect is attributed to wind currents entering the parquet lens and increasing convective losses, an effect which was especially noticeable under high wind speeds combined with high operating temperatures. The production collector should have a lower thermal loss.

The current/voltage characteristic curve for the prototype collector was measured for several conditions, with typical results shown in Figure 3.1.12. This curve agrees well with theoretical expectations. It should be noted that the production unit will have about 15% higher voltage levels due to 53 cells rather than the 46 cells in the prototype. Note that the short circuit current is 11 amps, which indicates a net flux on the cells of 11 amps $(2033\ \frac{w/m^2}{amp})$ = 22,363 w/m^2, which indicates a lens net flux concentration of (22,363/1003) = 22.3 suns, which indicates a net lens transmittance of $(\frac{22.3}{25})$ = 89%.

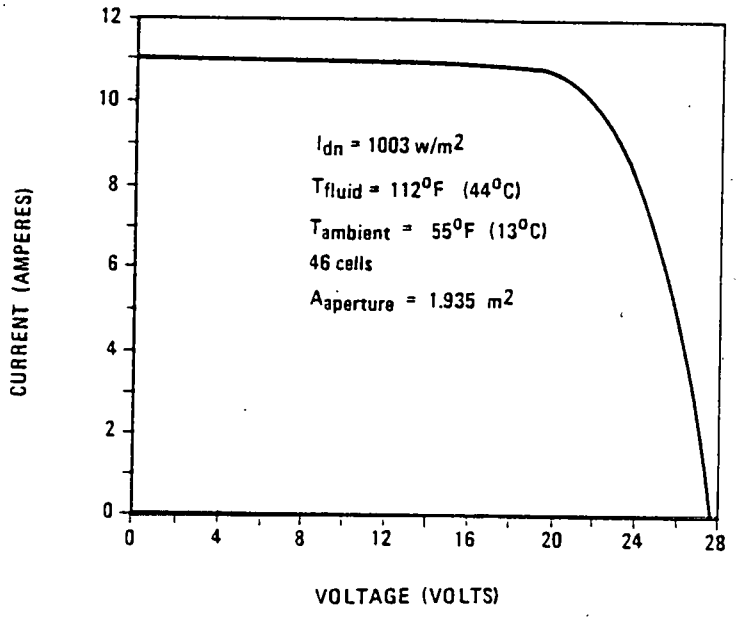

ETC011979-5

FIGURE 3.1.12 TYPICAL MEASURED CHARACTERISTIC CURVE FOR PROTOTYPE FRESNEL PHOTOVOLTAIC CONCENTRATOR

DESIGN CONDITIONS		TEST CONDITIONS
946 W/M^2	DIRECT NORMAL INSOLATION	1003 W/M^2
70°F (21°C)	AMBIENT TEMPERATURE	55°F (13°C)
114°F (46°C)	FLUID TEMPERATURE	111°F (44°C)
25	CONCENTRATION RATIO	25
PREDICTED PERFORMANCE		**MEASURED PERFORMANCE**
11.4%	ELECTRICAL EFFICIENCY	11.3%
58.6%	THERMAL EFFICIENCY	56.4%
70.0%	TOTAL EFFICIENCY	67.7%
85.0%	NET LENS TRANSMITTANCE FOR SILICON CELL RESPONSE SPECTRUM	88.7%

ETC011979-6

TABLE 3.1.2 COMPARISON OF PREDICTED VERSUS MEASURED PERFORMANCE FOR PROTOTYPE FRESNEL PHOTOVOLTAIC CONCENTRATOR

As presented above, the prototype test results agree well with theoretical predictions and verify that the new collector performs at excellent electrical and thermal efficiency levels. Table 3.1.2 presents a direct comparison of predicted design-point performance (presented at the Mid-Program Review, Reference 9) and measured performance from the curves of Figures 3.1.10 and 3.1.11 for the design point conditions. Note that the electrical, thermal, and total collector efficiencies measured for the prototype agree with theoretical predictions within a few percent. Such correlation indicates that the optical, thermal and electrical processes occurring within the collector are well understood and fully predictable. Finally, the new lens transmittance was measured to be higher (89%) than the predicted goal (85%), proving that the new concentrator can achieve excellent optical performance combined with extremely short focal length, thereby providing high efficiency at low cost.

3.1.3 Photovoltaic Assembly Environmental Cycling Tests

OCLI conducted the following thermal cycling test of E-Systems' sample photovoltaic receiver module:

Number of cycles: 50
Extremes : -40° and +90°C
Rate of Temperature Change: 100°C/hour
Length of Cycle: 4 hours
Result: The module was inspected by Quality and Product Engineering and no evidence of damage due to the exposure was noted.

3.1.4 Shading Protection & Illumination Transients

3.1.4.1 Shading Protection

There are two shading considerations to be taken into account:

1. Because of the roll-tilt tracking scheme of the system, up to three cells at either end of a module can be shaded at various times of the day and year. Figure 3.1.13. shows the % loss of power as a function of longitudinal tracking accuracy for three configurations of end cells. In the selected configuration of two end cells in parallel and bypassed by one diode, the loss due to shading can be kept to less than 3% for incidence angles less than 5°. As discussed in Section 2.2.3.1, the annual average incidence angle is less than 4°.

2. The possibility of accidental and transient shading will be handled by one bypass diode around the remaining 47 cells in the series string of one trough. Under these conditions the maximum reverse voltage that can appear across any one solar cell is approximately 25 volts, well below the breakdown voltage of the cell. When that point is reached the bypass device will turn on and reduce the reverse voltage across the shaded trough to less than 1 volt and the current to essentially zero. The diode used will be IN1199A type or equivalent, which are specified at 12AMP forward current and 50V PIV.

3.1.4.2 Illumination Transients

The major illumination transient will be lightning during seasonal thunder storms. Since it is highly unlikely that a lightning bolt would occur exactly aligned with the optical axis of the concentrating system, no transient problems with lightning are anticipated. Additionally under storm conditions the tracking and control system will have stowed the collectors in the morning starting position and disconnected the load from the system, so in the extremely unlikely condition of a lightning bolt on the eastern horizon, exactly on the optical axis of the collectors, only an open circuit voltage transient would be experienced.

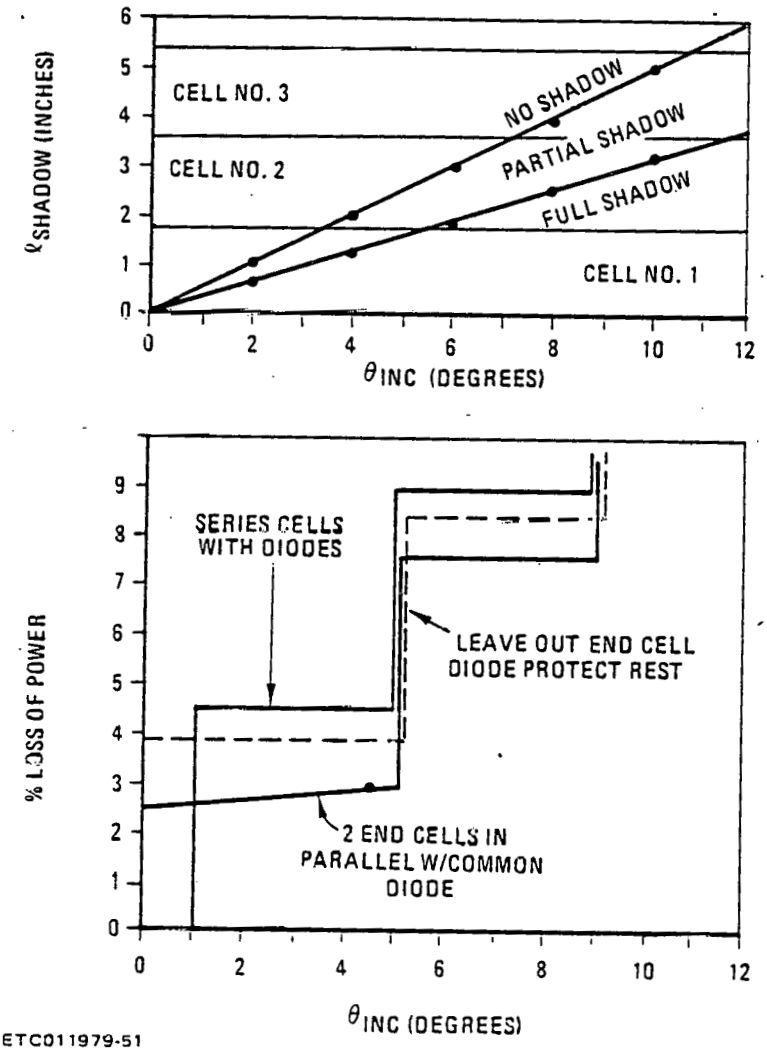

FIGURE 3.1.13 TRADEOFFS IN CELL SHADING PROTECTION

3.1.5 Array Material Costs

Array material costs have been accumulated in accordance with the DOE guidelines and are presented in Table 3.1.5.1. It is felt that the unit values used are reasonable and thus the cost picture developed therefrom is realistic.

As shown, the bottom line projected material cost for the DFW Photovoltaic Fresnel Lens Array is $160.85 per square meter. Examination of the makeup of this number clearly showns the bulk of the cost lies in the receiver, i.e. the photovoltaic cells represent 61% of the cost and the copper heatsink is another 8%. Only 31% of the total cost is in the array structural, optical and drive sections. However, as discussed in Sections 2.2 and 3.1, both analyses and tests indicate that the new lens can achieve higher concentration ratios, and thereby reduce cell and receiver costs. To maintain such higher concentration ratios, tighter tracking accuracies and stiffer structures will be required. Tradeoff studies remain to be done to fully optimize system performance/cost ratio. Thus the figures presented do not represent the ultimate costs of the Fresnel photovoltaic array.

TABLE 3.1.5.1

ARRAY MATERIALS COST PER DOE GUIDELINES

	Material	Lbs./Array	Matl. Cost	$/Array	$/M^2
Lens	Acrylic	244.7	.90/lb	220.23	9.88
Module Housing	Steel	773.7	.25/lb	193.43	8.67
Receiver	Copper	165.0	1.70/lb	280.50	12.58
Cells & Interconnects	8,764 cm^2	-	.25/cm^2	2,191.00	98.25
Array Structure	Steel	1001.0	.38/lb	380.38	17.06
Extrusions	Alum.	66.8	.85/lb	56.78	2.55
Tubing, Interconnects	Copper	34.5	1.70/lb	58.65	2.63
Gear Box	Steel	4.5	4.00/lb	18.00	0.81
Gears, Chains	Steel	5.0	4.00/lb	20.00	0.90
Motors	-	7.5	3.00/lb	22.50	1.01
Glass	Glass	34.9	1.20/lb	41.90	1.88
Misc. Items	90% Steel	206.4	.50/lb	103.20	4.63
TOTALS		2544.0		3,586.57	160.85

3.2 Power Conditioning, System Control & Switchgear

In the following subsections, a detailed description of the power conditioning unit, system control (consisting primarily of tracking control), and electrical switchgear will be presented. Additionally, the overall electrical system performance will be summarized and the instrumentation for monitoring this performance will be described.

3.2.1 Power Conditioning

E-Systems employs a unique solution for the conversion of photovoltaic (PV) power to commercial grade 480 VAC 3Ø 4 wire power. The pulse width modulated (PWM) inverter consisting of six banks of medium power switching transistors provides a highly efficient and cost effective design. In comparison to standard commercial inverters, the PWM inverter is ten percent more efficient at one-fifth the cost for production units.

The Power Conditioning Unit (PCU) performs the following functions:

- Supplies stable filtered 3Ø 60 HZ power to the test load.
- Automatically switches from utility line source to PV array when PV power production exceeds parasitic losses.
- Automatically switches from PV array source to utility line when PV power production falls below parasitic losses.
- Operates in a peak power point tracking mode to maximize PV power production.
- Provides fault protection and isolation of PV array and utility line.
- Supplies supplemental rectified DC power from utility line to maintain inverter input power at constant 27 KW level.
- Limits injection of harmonics.
- Maintains DC ripple constant below 2% of DC input current.

Power conditioning unit (PCU) specifications are listed in Table 3.2.1. Figure 3.2.1 illustrates the key components of the PCU as described

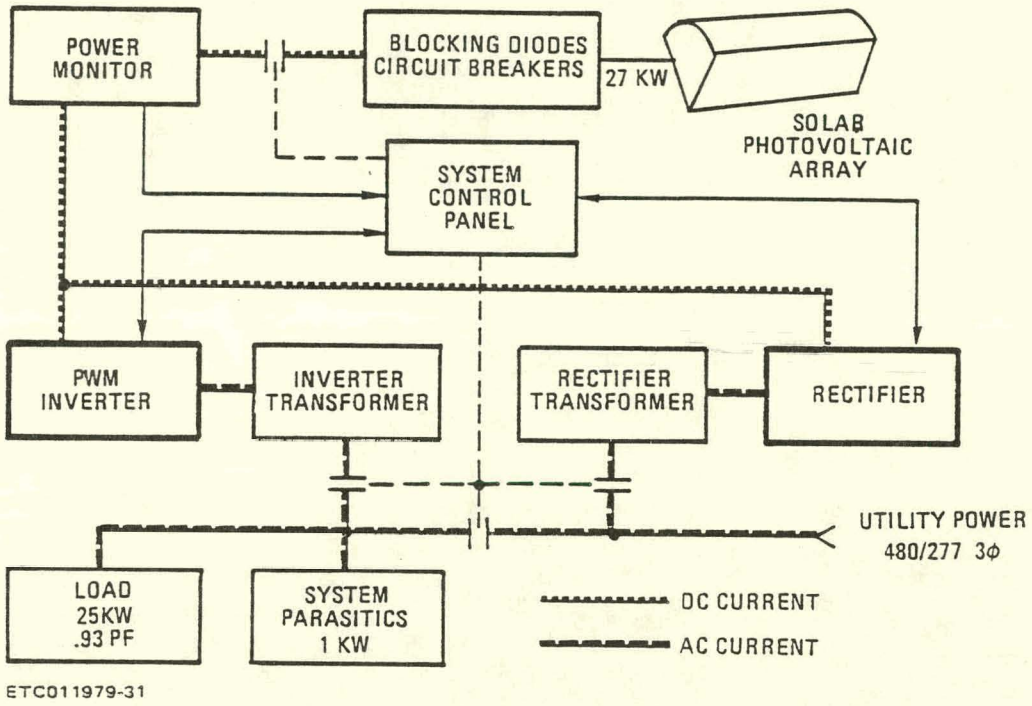

FIGURE 3.2.1. D/FW POWER SYSTEM

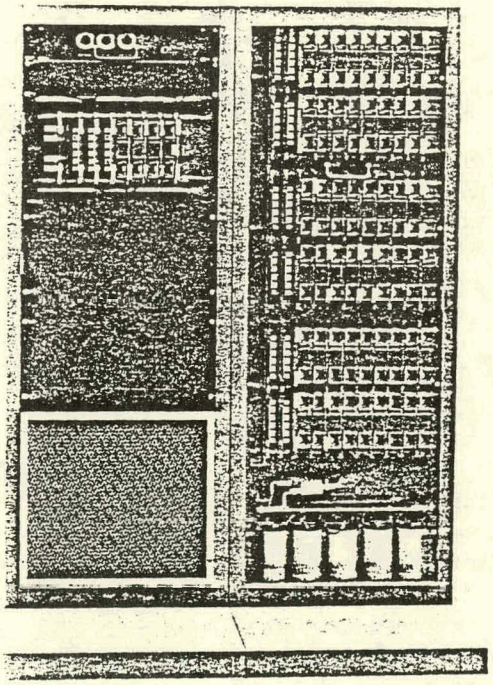

FIGURE 3.2.2 325 KVA PCU

below. Figure 3.2.2 is a picture of a similar PCU having a capacity of 325 KVA. PCU specifications are listed in Table 3.2.1.

TABLE 3.2.1

PCU SPECIFICATIONS

PCU Input Power	27 KW
PCU Input Current	104 Amps nominal
PCU Input Voltage	200-300 VDC, 260 VDC nominal
Overvoltage	350 VDC Max.
Overcurrent	200% rated current
PCU Output Voltage	480/277 VAC 3Ø 60 Hz 4 wire
PCU Output KW	26 KW (28 KVA at 0.93 Power Factor)
Harmonic Distortion	Less than 5% total, 1% any one harmonic
Ripple Current	Less than 2% of DC input current
Inverter Efficiency	97% at 27 KW
Rectifier Efficiency	Up to 97.5%
Ambient Temperature	-10 + 45°C
Relative Humidity	96% non condensing
Pressure	520-760 mm Hg
Electrical	Conforms to NEC
EMI	Conforms to Mil Std 461-A

Primary components included in the PCU are:

Inverter - Transforms PV array power to conventional AC power. Six banks of 58 medium power transistors sharing a common input from the eleven arrays are distributed to form three legs of the 3Ø 60 Hz circuit. Fault protection and control circuits are included.

Rectifier - Provides DC power to the inverter to maintain the 27 KW input level whenever the PV array output falls below 27 KW. Regulated power supply consists of a two stage rectifier, diode section in series with a SCR section which provides precise output voltage control.

Power Monitor- Control circuitry monitors PV array output and originates a power signal directly proportional to PV array power delivered to the inverter. Analog integrated circuits monitor and compute instantaneous power levels.

PCU System Control - Provides the peak power point tracking control signal by sampling instantaneous power levels and comparing the last sample with the previous value.

The voltage regulation control signal commands the rectifier to increase or decrease output voltage and results in the appropriate adjustment of the PV array output voltage to maximize PV array power output. Analog and digital integrated circuits generate control signals.

Switchgear - Contactors and delay relays are used for fault protection and switching.

Selection of the switched transistor PWM inverter was based on its performance and cost advantages as shown in Table 3.2.2.

TABLE 3.2.2

PCU COMPARISON CRITERIA

	Standard SCR Power Inverter	Transistor Inverter
Conversion Efficiency	84%	97%
Nominal Rating	30 KW (0.8 PF)	27 KW (0.8 PF)
Voltage	130 DC/120 AC	260 DC/277 AC
MTBF/Reliability	60,000 HR commercial unit	10,000 HR initial units produced
Availability	Production (Mod Required)	Designed
Equipment Size/ Heat Dissipation	Large	Small
Production Cost	$1275/KW	$200/KW

3.2.1.1 PCU Control

PCU control functions are performed within the PCU. Voltage regulation provides output voltage independence from PV using input voltage variations. Voltage feedback from each inverter output is applied to the corresponding modulator comparitor. Synchronization of inverter output with the power grid, inverter phase angle relationship and inverter frequency

stability is provided by monitoring the power grid with a three phase control transformer.

Control of the inverter's switching transistor is provided by the inverter controller logic chip that interfaces modulators and drive buffers. It is a state machine whose next clock internal state is a function of four present state registers and 16 additional inputs. Logic comparitors provide fault inputs to the inverter controller for overvoltage or undervoltage conditions or out of limits logic voltage.

Control of transistor failure conditions is provided by fusing each transistor. Load faults which pull the transistors out of near saturation will interrupt the control chip and cause the output stage to be momentarily turned off. Drive is reapplied within a few miliseconds so that a safe current limited mode of operation can allow the fault to clear. Continuation of the fault results in input and output contactors opening and PCU shutdown.

Specific control involving electromechanical contactors and delay relays will be discussed in section 3.2.3.

3.2.1.2 Peak Power Point Tracking

The PV array output is monitored and the peak power point is tracked by adjusting the rectifier output voltage. The rectifier voltage is a forcing function that sets the operating voltage level for the array. Figure 3.2.3 illustrates the power curve on which rectifier voltage forces the array to operate.

Discrete logic provides tracking control based on array power which is sampled at a one second interval. Each power level measurement is compared to the last value and a voltage control output is generated. As long as the last measured power continues to be higher, the control voltage

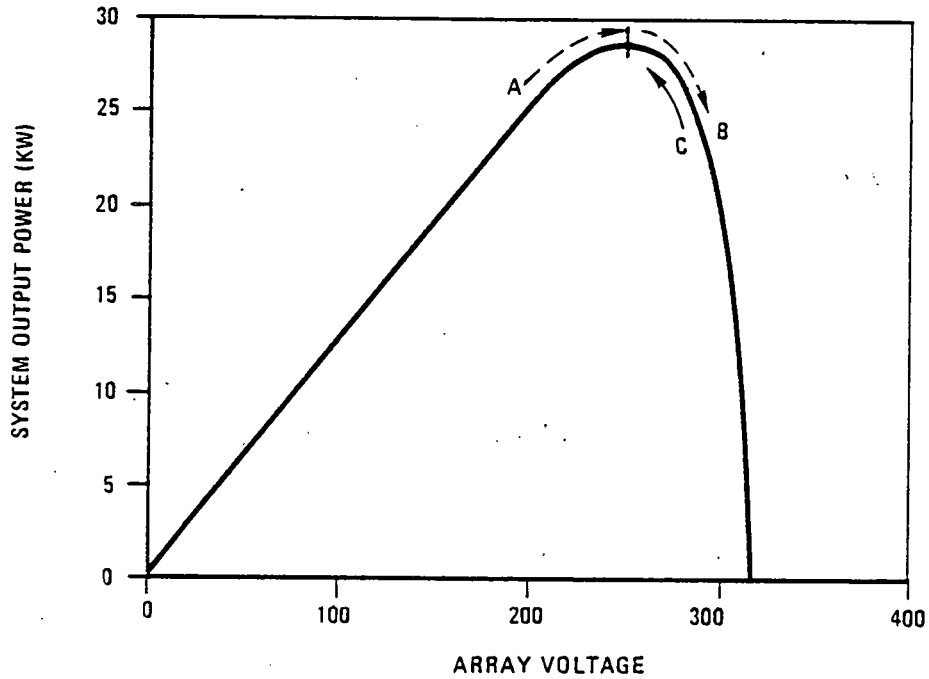

ETC011979-9

FIGURE 3.2.3 PEAK POWER CURVE

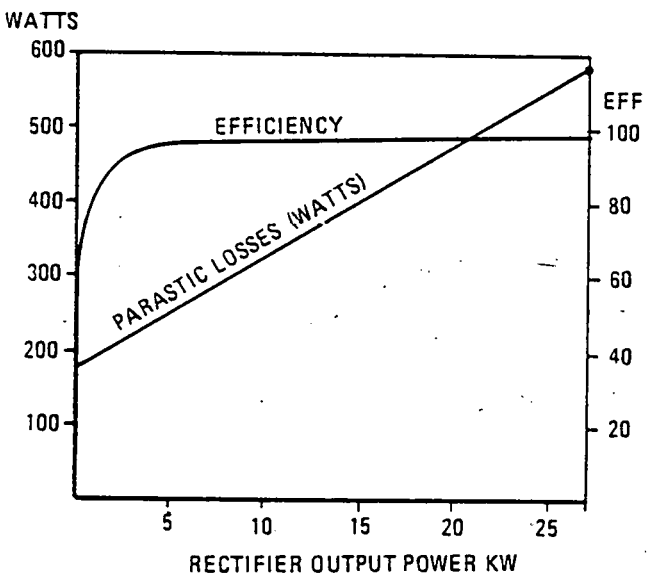

ETC011979-10

FIGURE 3.2.4. RECTIFIER EFFICIENCY

will maintain the same polarity (Arrow A) and continues to seek the peak power point with a voltage increase.

Once the measured power indicates a reduction from the last value, (Arrow B) the control voltage will reverse its direction of change. This indicates that the peak power point has been passed. A decreasing rectifier voltage will drive the array power production (Arrow C) back to its maximum. The hunting will continue with 0.4 volt increment per second. Normal operations consist of an oscillation about the peak power point that maintains rectifier voltage within ± 0.4 volts. The tracking circuitry has 256 steps which can be preset to a selected voltage increment for fine or coarse tracking. Using the 0.4 volt increment, the time required to reacquire the peak power point would average two minutes where the peak power point shifts to either extreme. A worst case time would be 4.3 minutes to track from 200 to 300 volts DC.

3.2.1.3 Efficiency

A high efficiency PCU was selected to minimize system parasitic losses. This approach is state-of-the-art and further improvements are not currently available. Table 3.2.3 contains the power losses and efficiency of the inverter.

TABLE 3.2.3

INVERTER EFFICIENCY*

Unit	Parasitic Losses (Watts) Full Load	Efficiency
Inverter	540	98%
Transformer	270	99%
Total	810	97%

*The inverter always operates at full load in the DFW Photovoltaic system. Thus, parasitic losses and inverter efficiency are constant.

The inverter efficiency of 97% is substantiated by test data derived from actual tests of a similar inverter.

A calorimeter test performed on one of the 325 KVA transistor switching modules resulted in measured heat losses of 151 watts which was equivalent to 98.2% efficient.

Figure 3.2.4 shows the rectifier efficiency as a function of rectifier power delivered. Rectifier parasitic losses are shown in watts. Rectifier efficiency increases rapidly as loading increases. Normal daily operations will require rectifier outputs from zero up to about 25 KW to supplement the PV array. While the rectifier efficency is low at low power levels, the actual power losses are small when compared to the total power delivered by the PV array.

3.2.2 System Control

PV array system control describes the start up, sun tracking, shut down and fault conditions that are incorporated into the control circuitry. Controls internal to the PCU are discussed in the PCU and Switchgear section. Process control of coolant flow is included here.

3.2.2.1 Tracking

The tracking system is designed to provide roll axis tracking accuracy of $\pm$ 0.05 degrees, tilt axis accuracy of $\pm$ 0.75 degrees and automated controls to allow automatic roll axis tracking and safe operation.

Roll axis control is self starting, active tracking and responsive to insolation intensity and fault conditions. Tilt axis tracking requires periodic manual adjustments simultaneously positioning all eleven arrays to compensate for the 63 degree variation which occurs over a six month period. Figure 3.2.5 illustrates the roll and tilt block diagrams.

3.2.2.1.1 Roll Axis

Roll axis tracking control is provided by the tracking and control

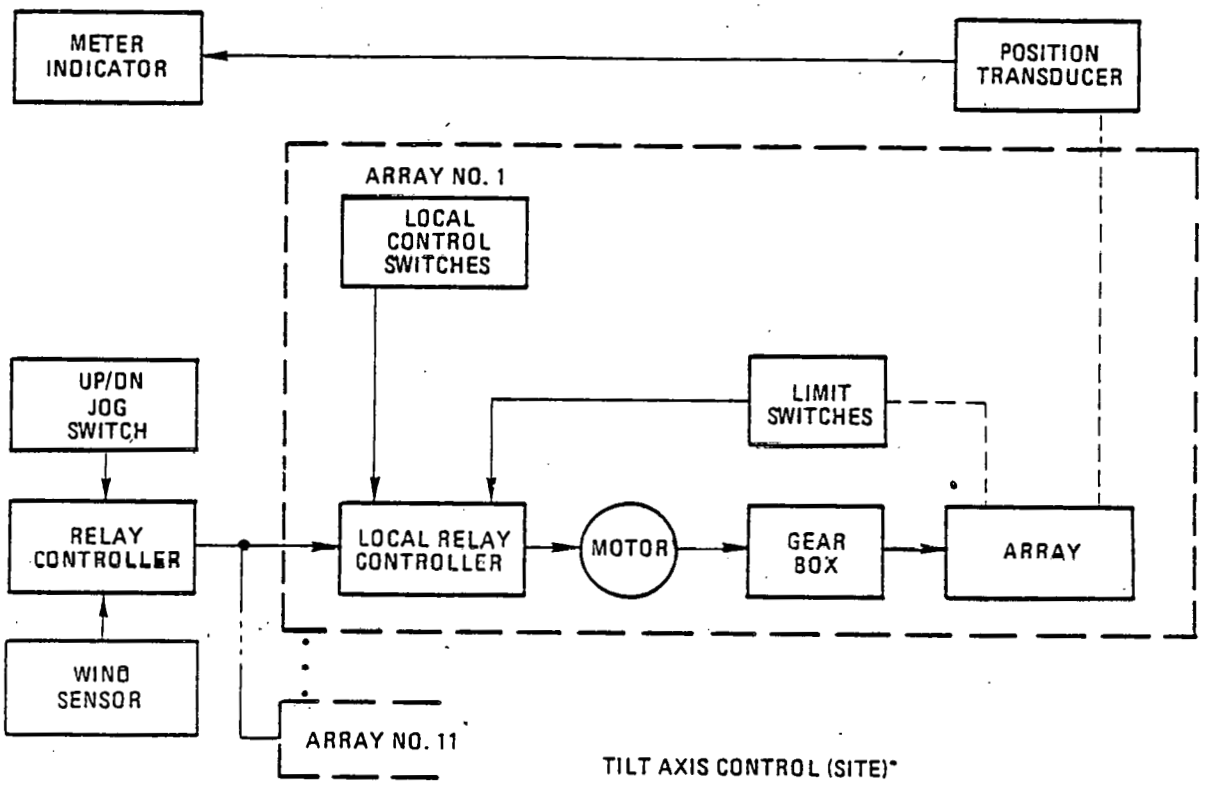

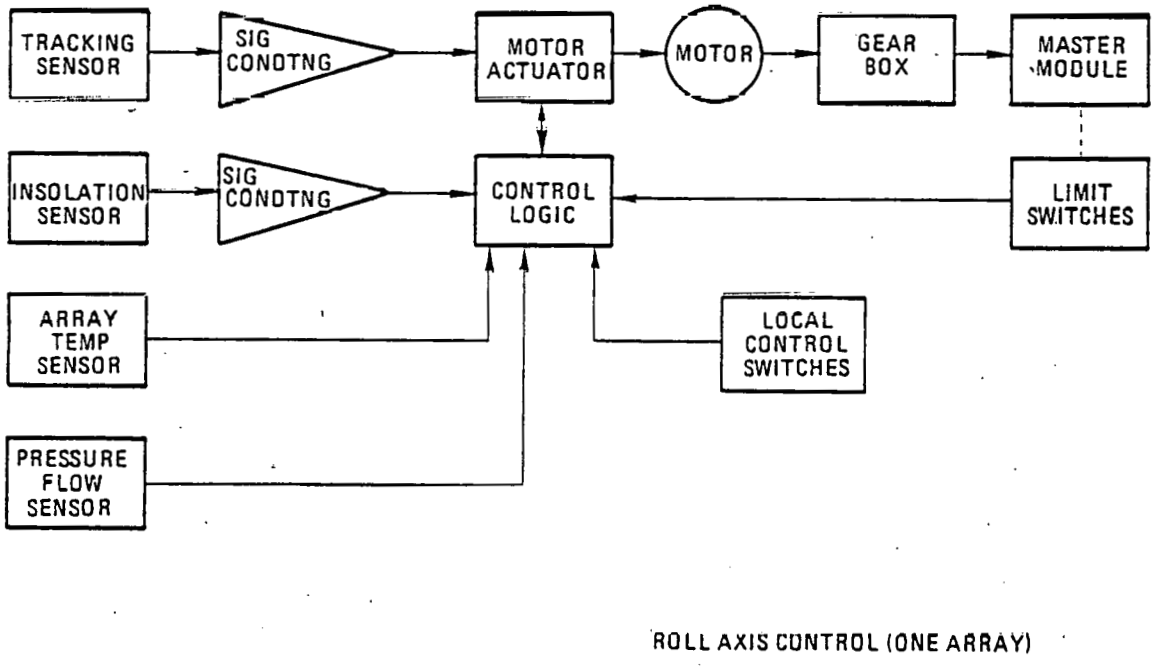

ETC011979-1

FIGURE 3.2.5. SYSTEM BLOCK DIAGRAM

unit which is mounted on the master module of each array.

The tracking and control unit provides:

- Automatic start of array track
- One direction track
- Bi-directional slew
- Roll axis tracking error signal
- Low insolation level detector and track inhibit
- Insufficient insolation and return to stow signal
- End of day return to stow signal
- High temperature limit return to stow
- Loss of pump motor return to stow
- Reset tracking logic at stow in preparation for the next day

Roll axis tracking is single direction track and two direction slew. The unit will initiate tracking and follow the sun until the end of day occurs and a stow command is generated. Intermittent cloud cover will cause the insolation level detector to generate a track inhibit command when the low insolation threshold is violated. The arrays will stop tracking until the cloud passes and the arrays re-start and slew to the sun's new position. Extended cloud coverage will cause collector temperature to drop and result in the coolant pump motor to turn off. If the light level decreases below the second threshold due to heavy storm related clouds, all arrays will return to stow. The roll axis motor is a five watt instrument motor with a six RPM output speed. The array can be slewed from East limit to West limit (150 degrees) in thirty minutes. Slew speed is five degrees per minute which is twenty times the average track speed. The high slew speed provides for rapid repositioning of the array from stow to a late start position up to 120 degrees west of stow.

Limit switches are placed to inhibit roll axis rotation at either end of the 150° track. A positive interruption of the current to the track motor as well as logic interrupts to the tracking and control unit are provided by the limit switches. Local control switches are mounted in the roll axis drive enclosure to allow an array to be taken off-line in the roll axis. Once off-line, the array can be manually controlled in roll independent of the other arrays. A prototype roll axis tracking control unit was tested during Phase I and provided ± 0.02° tracking accuracy, substantially better than required.

3.2.2.1.2 Tilt Axis

The tilt axis control system is manually activated by an operator about

every four days (every two days near equinox, every week near solstice) to reposition the eleven arrays. A position potentiometer located on the master array provides position feedback data to the analog display meter, on the operator's console control panel

The tilt axis is driven by a 1/15 horsepower 30 RPM gear motor, which provides full travel of 64.5 degrees in 30 minutes.
Each array's drive motor is controlled by two latching relays, one for up and one for the down direction. The relays are located in the panel box at the base of the array. The box also contains local control switches for isolating the array and manually positioning the array in tilt. Simultaneous control of the eleven arrays is exercised by a single set of latching relays at the control station. One relay provides up control and one provides down control. Either relay latches and holds until manually interrupted by the operator depressing the off button. The tilt axis drive hardware is duplicated for each of the eleven arrays. Only the master array has the tilt axis position transducer for positioning control.

The master array's position transducer provides an analog voltage proportional to the array's position. The transducer is a single turn potentiometer with 5 VDC applied across the full potentiometer. An output of 0-1 VDC represents 64.5 degrees of travel which will indicate full scale on the tilt angle panel meter. The panel meter has twelve months and days of the month annotated across the meter face so that 182 divisions represent the maximum range of the tilt axis. The non-linearity of the elevation track between solstices will be compensated for by layout of the meter face scale. Position accuracy is within 0.75 degrees.

Repositioning of the master array tilt is done by manually pulsing (energizing) the tilt axis motor in the up or down direction until the tilt axis position meter indicates the appropriate day of the year. All array tilt axis drive motors operate from the same control relay which provides

electrical slaving of all arrays. Position errors which accumulate over extended periods of time are removed when the arrays are returned to the prealigned stow position.

A wind sensor mounted with the weather station provides a contact closure with a wind speed exceeding 45 MPH (20 mps). This switch action will activate the tilt axis drive motor to move the arrays to the tilt axis stow.

3.2.2.2 Process Control

The coolant pump is included in the control system. The one horsepower 480 VAC 3Ø motor is actuated from the control panel. A motor contactor provides a loss of power signal to the track and control unit of each array. When activated, all arrays drive to stow. The master array has a temperature sensitive switch located on one module's receiver. A rise in receiver temperature above 100°F will activate the coolant pump motor, while a drop in receiver temperature below 90°F will shut off the pump motor.

3.2.3 Switchgear

Standard electromechanical power switchgear is used to transfer load between array and utility power grid. Isolation of the PV array from the utility power grid and protection from utility load and PCU faults are provided. Delay relays protect against restart faults. AC load switching is "make before break" to provide continuous operations.

All switchgear is included in the PCU with the following exceptions:

480 VAC 3Ø line circuit breakers
260 VDC array circuit breakers
solid state blocking diodes

3.2.4 Electrical System Parasitic Losses

In addition to the parasitic losses of the PCU, additional losses are inherent in the system. Table 3.2.4 contains the losses estimated for DFW.

3.2.5 Instrumentation

The PCU is instrumented to monitor power, integrated power, current and voltage as illustrated in Figure 3.2.6. Measurement transducers are

TABLE 3.2.4

PARASITIC LOSS

Source	Remarks	Loss (Watts)	% Peak Array Power
Wiring	Est 484 ft. # 10 copper wire	418	1.5
Blocking diodes	11 diodes 0.6 VDC at 9.4 AMP	62	0.2
Transformer		50	0.2
Relay	26 relays at 3 watts	78	0.3
Power supplies	2 units	95	0.5
Track motors	11 tilt and roll motors	3	0.01
Coolant pump motor	Vendor data	600	2.2
Total		1306	4.91

located in the monitor panel and provide control signals to the data logger and for presentation on the display panel. Transducers are accurate to 0.5%. All transducers are off the shelf commercial devices.

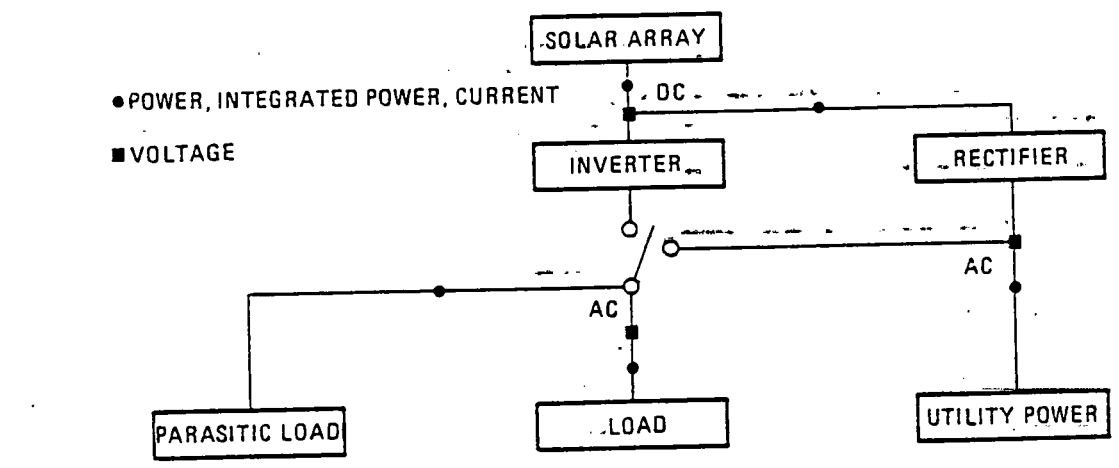

FIGURE 3.2.6. ELECTRICAL SYSTEM INSTRUMENTATION

3.3 Thermal System

The thermal system is a simple recirculation loop through which a 30% ethylene glycol/water solution circulates, absorbing thermal energy in the collector field, transferring the energy collected through a boiler feedwater heat exchanger, and then returning the fluid to the collector field. The thermal transfer portion of the circulation loop is shown schematically in Figure 3.3.1. A heat exchanger module which includes the pump, boiler feedwater heat exchanger, over-temperature heat exchanger, expansion tank, controls and instrumentation has been designed and will be located in the basement of the Central Utility Facility at the DFW airport. All components are existing, off-the-shelf, short lead-time procurement items that have been used in hydronic systems for many years. Major components, piping and insulation system and instrumentation are:

- Pump - a one-horsepower Bell and Gossett Series 1522-12 centrifugal pump provides the required pumping head at the design flow rate (6250 kg/hr). Overall motor-pump efficiency is 44% at operating point.
- Boiler Feedwater Heat Exchanger - a single pass, counterflow shell-and-tube Bell and Gossett heat exchanger, two in series, model STH-630-1. At design conditions, overall heat transfer coefficient (UA product) is 12000 w/°C; pressure drops are 7 psi for glycol solution and 1 psi for feedwater.
- Over-Temperature Heat Exchanger - a single unit as described for the boiler feedwater heat exchanger above.
- Expansion Tank - sized for fluid thermal expansion and system operating pressure range. 80 gal. ASME code pressure tank. 125 psi working pressure. Maximum temperature 450°F. Manufactured by Thrush Products, Inc.
- Piping - sizes selected to minimize pumping head requirements and to evenly distribute flow to 11 arrays. Nominal 2 in (5 cm) type M hard copper tubing from collector field to heat exchanger

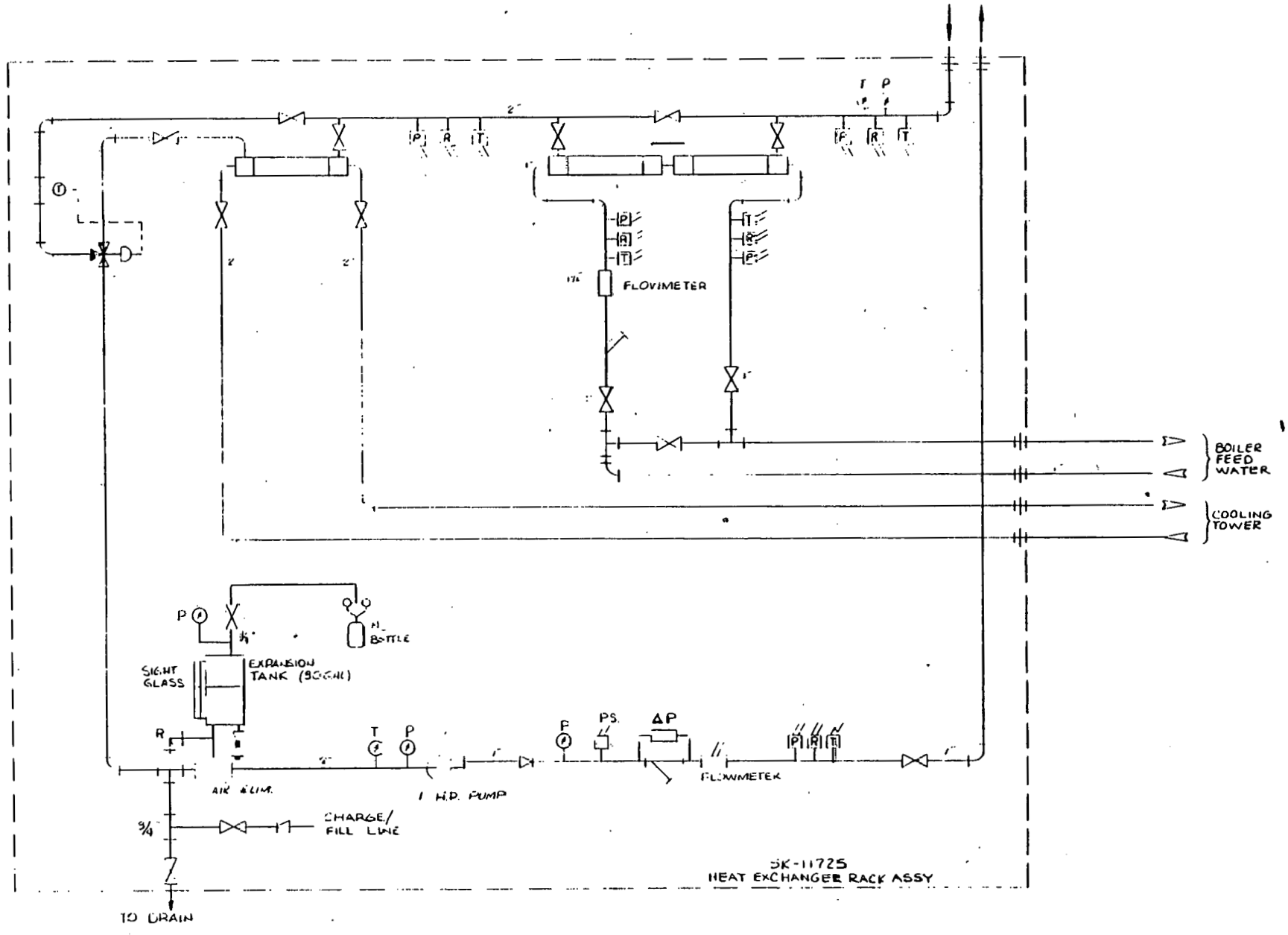

ETC011979-52

FIGURE 3.3.1 FLUID/THERMAL TRANSPORT SYSTEM

rack. Nominal 2 in (5 cm) carbon steel ASTM A-106 Grade B pipe throughout heat exchanger module assembly. Total pressure drop through manifold piping and arrays is 15 psi.

- Insulation - Johns-Manville Micro-Lok 650 fiber glass insulation with aluminum jacket for exterior environmental protection. Nominal 3 in. (8 cm) from collector field to heat exchanger module; nominal 2 in (5 cm) from heat exchanger module to collector field. On annual basis piping thermal losses are only 3 1/2% of net heat collected.

- Instrumentation - Thermocouples and resistance temperature sensors (RTD) located throughout collector field and thermal system to measure fluid temperature. For all energy balance measurements the RTD and thermocouples will be used in a differential mode to measure inlet to outlet temperature differences across major components. In differential mode RTD's provide 0.02°C accuracy while thermocouples provide 0.1°C accuracy. For absolute temperature measurements these accuracies are 0.5°C for RTD's and 1°C for the thermocouples. Specially calibrated turbine flowmeters will be used which have accuracies of 0.5% of flow. Semiconductor pressure transducer will be used with accuracies of 1% of pressure.

4.0 ENVIRONMENTAL ASSESSMENT AND IMPACT

The photovoltaic system proposed for DFW Airport will be placed on the central utility plant in the center of the terminal area of the airport. The immediate environment, therefore, is secure, of limited access, and populated with professionals and skilled labor who will be knowledgeable of the system and its purpose. The only chemical component used in the system is a water solution of ethylene glycol, or antifreeze which is a nonvolatile compound of very low toxicity which is used in a closed heat exchanger subsystem. No emissions to the atmosphere will occur during normal operation and accidental leakage and spillage of this solution can be cleaned up and disposed of with no loss to the environment.

DFW Airport has been designed to emphasize its functional aspects. The landscape is dotted with manifestations of this functionality. Radar Antennas, Control Towers, Power lines, and the electrified tracks of the automatic people mover, Air Trans, are all part of the local environment. The proposed photovoltaic system will fit into and become a compatible part of this.

The one area of environmental sensitivity could be the power inverter which will convert the D.C. power generated by the photovoltaic system to 60 cycle A.C. power suitable for use in the central utility plant. The solid state power devices used in this subsystem will be switching on and off during normal operation and will generate harmonics of the fundamental frequency which, if uncontrolled and powerful enough, could interfere with one or more of the radio frequency communication systems at the airport.

This environmental factor has been considered in the design of the inverter subsystem, which will conform to the military specification MIL-S-461-A. Measurements of RFI will be made on the system and if necessary additional precautions will be taken to reduce these emissions below the level of sensitivity. No problems in controlling this environmental factor are anticipated.

In general then, the proposed photovoltaic system at DFW Airport will have minimal or no impact on the local surrounding but will be readily integrated into, and become a compatible part of, that environment.

5.0 REFERENCES

1. Ross, J. A., "Design and Construction of Advanced Design 10 KW Power Conditioning Units for Photovoltaic Power Systems," La Jolla, California, December, 1978.

2. O'Neill, Mark J., "Solar Concentrator and Energy Collection System," U. S. Patent No. 4,069,812, 24 January 1978.

3. Optical Coating Laboratory, Inc., "Concentrator Solar Cells and Modules for Department of Energy Photovoltaic Concentrator Application Experiment," City of Industry, California, December 23, 1977.

4. Utesch, Al, Manager, Central Utility Facility at DFW Airport, Private Communication, July, 1978.

5. "Insolation Climatology Data Base," Report No. ATE-74 (7417-16)-2, Volume III, Aerospace Corporation, El Segundo, California, 1974.

6. "Hourly Solar Radiation Surface Meteorological Observations - User's Manual," Volume I, TD-9734- "Typical Meteorological Year," Asheville, North Carolina, August, 1978.

7. Hovel, Harold J., Semiconductors and Semimetals, Volume 11, Academic Press, 1975.

8. E-Systems Energy Technology Center, "A Proposal for a Fresnel/Photovoltaic Concentrator Application Experiment for the Dallas-Fort Worth Airport", No. ETC/78P-001, Dallas, Texas, January 1978.

9. E-Systems Energy Technology Center, "A Fresnel/Photovoltaic Concentrator Application Experiment for the Dallas-Fort Worth Airport - Mid-Program Review," Albuquerque, New Mexico, October, 1978.

DISTRIBUTION:
TID-4500-R66, UC-63a (235)

Division of Distributed
Solar Technology (10)
U.S. Department of Energy
600 E Street NW
Washington, D.C. 20545
Attn: R. SanMartin
P. Maycock
A. Krantz (6)
L. Magid
A. Clorfeine

U.S. Department of Energy (6)
Albuquerque Operations Office
Albuquerque, NM 87115
Attn: D. K. Nowlin, Director
Special Programs Division

SERI, Library (2)
1536 Cole Blvd., Bldg. #4
Golden, CO 80401

SERI (2)
1536 Cole Blvd.
Golden, CO 80401
Attn: L. Mrig
H. Lauffenburger

Jet Propulsion Laboratory (6)
4800 Oak Grove Drive
Pasadena, CA 91103
Attn: R. Forney
W. Callaghan
R. Ross
R. Ferber
P. Sutton
J. Hesse

NASA/LeRC (2)
21000 Brookpark Road
Cleveland, OH 44135
Attn: J. Deyo
A. Ratajczak

The Aerospace Corporation (2)
P. O. Box 92957
Los Angeles, CA 90009
Attn: S. Leonard
B. Siegel

MIT-Lincoln Lab (2)
Box 73
Lexington, MA 02173
Attn: M. Pope
S. Sacco

MIT-Energy Lab
Cambridge, MA 02139
Attn: R. Tabors

4700 J. H. Scott
4710 G. E. Brandvold
4719 D. G. Schueler
4719 E. L. Burgess (75)
4720 V. L. Dugan
8266 E. A. Aas
3141 T. L. Werner (5)
3151 W. L. Garner (3)

For: DOE/TIC (Unlimited Release)

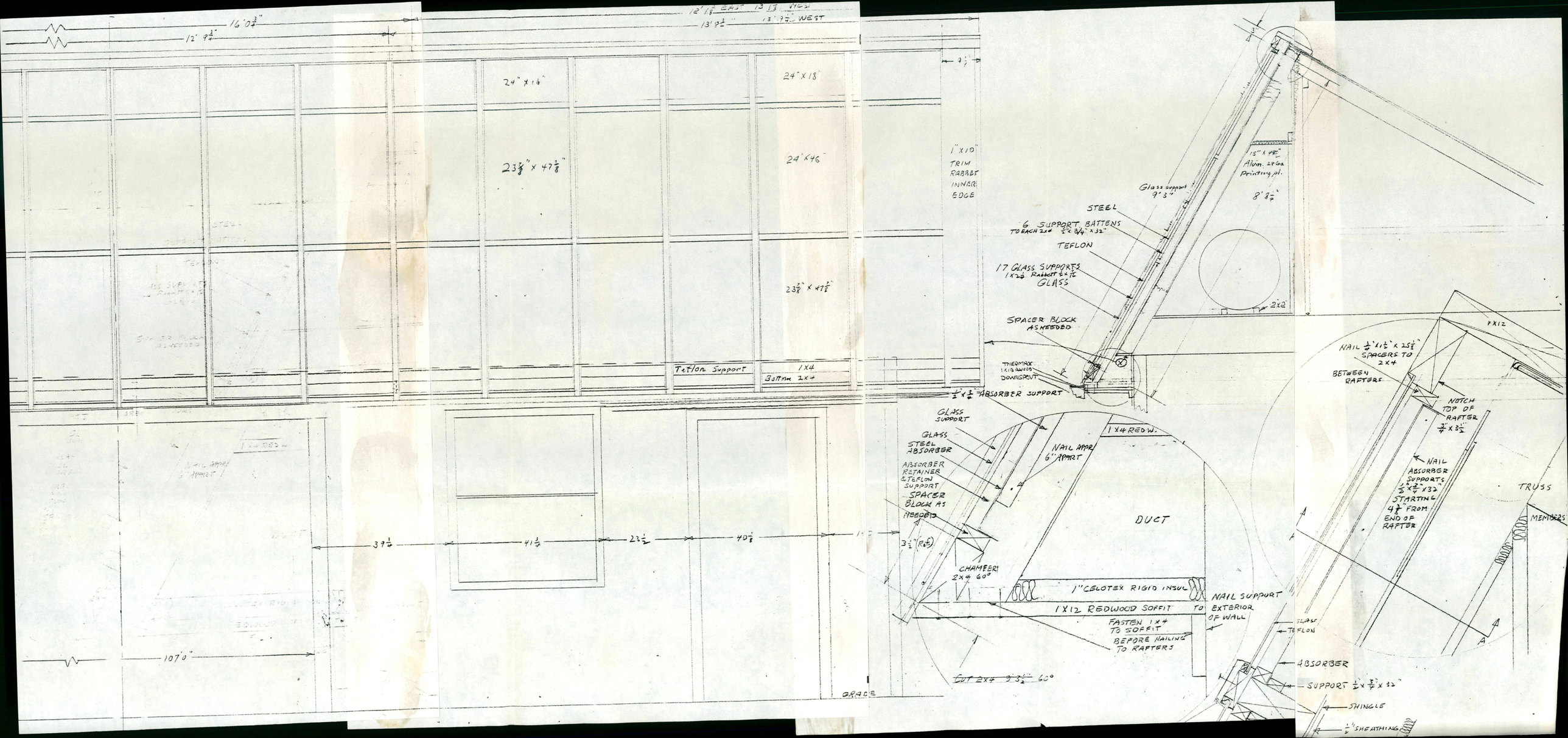
16'0 3/4"
12'9 3/4"
13'9 1/2"
24"X16"
24"X18"
23 3/8"X47 1/8"
24"X48"
1"X10" TRIM RABBET INNER EDGE
Teflon Support
1X4
3/8"thk 2X4
37 1/4
41 1/4
23 1/2
40 1/8
107'0"
GRADE
Glass support 9'3"
8'8 1/2"
15"X92" Alum. 24Ga Printing pl.
STEEL
6 SUPPORT BATTENS TO EACH 2X4 1/2X3/4"X32"
TEFLON
17 GLASS SUPPORTS 1X2 1/2 RABBET 1/4X7/8
GLASS
2X2
SPACER BLOCK AS NEEDED
THERMAX 1X13 REDWOOD DOWNSPOUT
1/4"X1 1/2" ABSORBER SUPPORT
GLASS SUPPORT
GLASS
STEEL ABSORBER
ABSORBER RETAINER & TEFLON SUPPORT
SPACER BLOCK AS NEEDED
3 1/2"(R&L)
1X4 REDW.
NAIL APPR 6" APART
DUCT
CHAMFER 2X4 60°
1"CELOTEX RIGID INSUL
1X12 REDWOOD SOFFIT
NAIL SUPPORT TO EXTERIOR OF WALL
FASTEN 1X4 TO SOFFIT BEFORE NAILING TO RAFTERS
Cut 2X4 9 3/4" 60°
1X12
NAIL 1/8"X1 1/2"X2 5/8" SPACERS TO 2X4 BETWEEN RAFTERS
NOTCH TOP OF RAFTER 3"X3 1/2"
NAIL ABSORBER SUPPORTS 1/2X3/4"X32" STARTING 4 3/4" FROM END OF RAFTER
TRUSS MEMBERS
A
A
GLASS
TEFLON
ABSORBER
SUPPORT 1/2X3/4"X32"
SHINGLE
1/2" SHEATHING

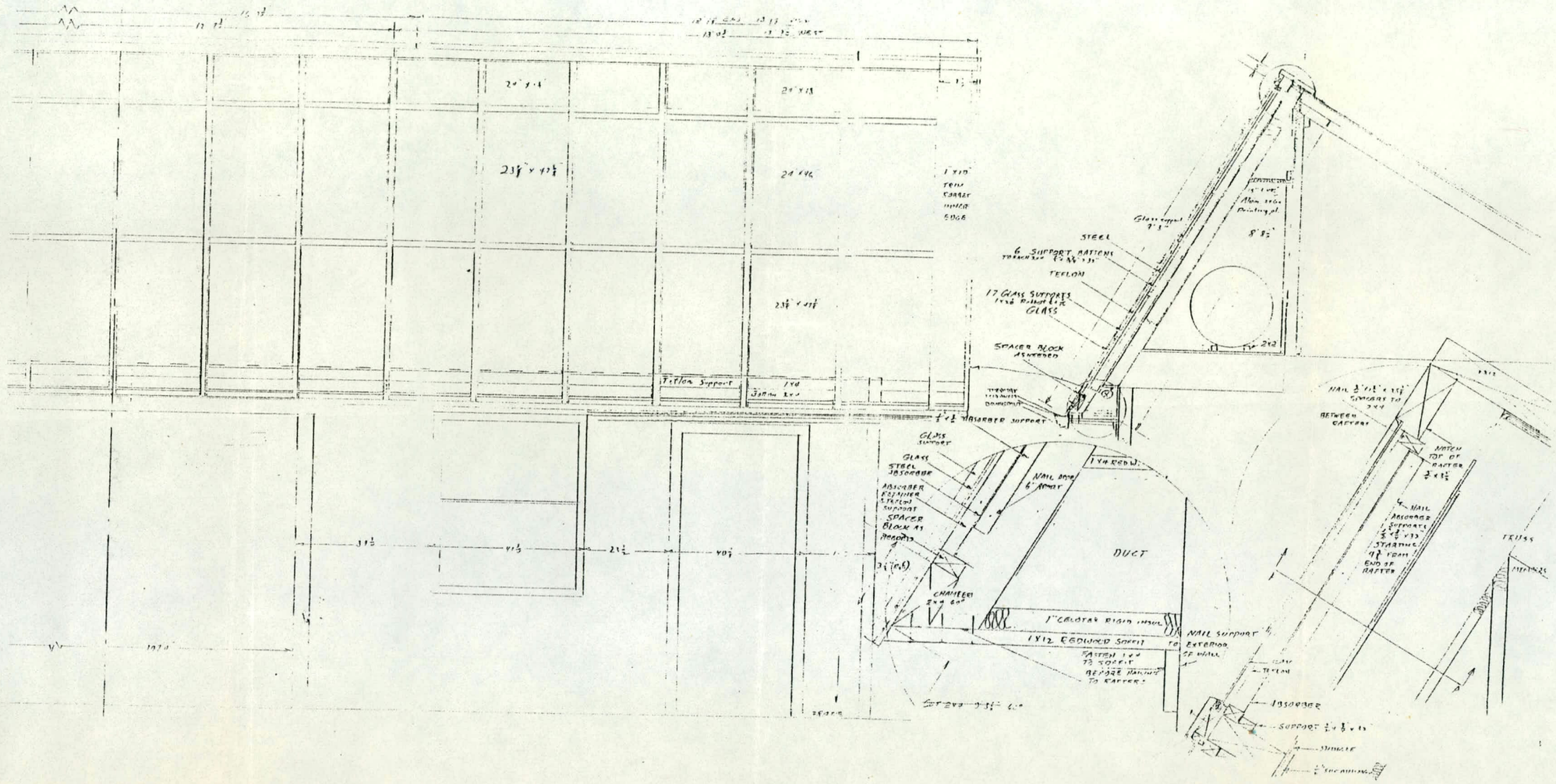
Teflon Support
DUCT
GLASS
SPACER BLOCK
TEFLON
NAIL SUPPORT
DUCT